Gravitational microlensing of extended objects

Iain James Coleman

Thesis submitted to
the University of Glasgow
for the degree of Ph.D.
in March 1998

Department of Physics & Astronomy,
Kelvin Building,
University of Glasgow,
Glasgow, G12 8QQ

Abstract

Gravitational microlensing is an important tool in the search for Galactic dark matter. This thesis investigates how microlensing can be used to infer astrophysically interesting information about the structure of extended objects, as well as the feasibility of using extended source effects to improve the estimates of the lens parameters.

I develop a simple, widely applicable model of an extended stellar envelope, and use it as the source object in microlensing simulations. This demonstrates the effect of the envelope structure and the lens parameters on the photometric and polarimetric light curves. It is shown that important information about the envelope is contained in the light curve. Furthermore, the levels of variable polarization produced are well within current observational capabilities, and the signal can be used to effectively constrain the mass, distance and transverse velocity of the lensing object. The use of polarization profiles as a microlensing diagnostic is demonstrated.

An overview of inverse problem theory is presented, with particular emphasis on the Backus-Gilbert technique which is used extensively in the thesis. This inversion method is then applied to the problem of determining stellar limb polarizations from binary systems. I study extensively the influence of the system orbital parameters and the data quality on the accuracy and stability of the inversion, and show that the relative sizes and orbital inclination of the stars is the most important factor. I also show that limb polarization profiles can be estimated with the same method.

Finally, I invert simulated microlensing light curves, to determine limb darkening and

chromatic profiles of lensed stars. We show that meaningful inversions are only possible in the case of a transit event. Furthermore, although data quality is important, the number of data points does not greatly affect the inversion provided there are more than about fifty points. The inner part of the disk is always poorly recovered, but the intensity profile in the outer part of the disk can be estimated to a high degree of accuracy.

The basic work in this thesis can form the foundation of much more detailed studies, for which some suggestions are outlined at the end.

Contents

Acknowledgements 1: Faceless Organisations

This PhD study was carried out in the Department of Physics and Astronomy of the University of Glasgow. It was funded by the Particle Physics and Astronomy Research Council. My thanks to both these organisations.

Fig. 1.1 was created with support to Space Telescope Science Institute, operated by the Association of Universities for Research in Astronomy, Inc., from NASA contract NAS5-26555 and is reproduced with permission from AURA/STScI. It is available royalty-free in digital form.

Acknowledgements 2: Real People

A thesis does not spring fully-formed from the head of the student: it grows slowly in a favourable environment, carefully tended and nurtured. Many people contributed to that environment, and they deserve a note of thanks.

First and foremost is John Simmons, my supervisor, whose gentle and perceptive influence can be detected throughout this thesis. John Brown, head of the A & A group (and my supervisor for a while), and Robin Green, my second supervisor, also played important roles.

Various parts of my PhD work were done in collaboration with others, and this thesis has benefitted greatly from their contributions. Jon Bjorkman participated in the work in Chapters 2 and 3, in particular providing results from his Monte Carlo code. Norman Gray worked closely with me on the inversion work in Chapters 4 and 5, and performed the heroic feat of integration outlined in Appendix B, which forms the foundation of Chapter 6.

Less tangible, but nonetheless important, are the various discussions I have had with colleagues. David Valls-Gabaud, Martin Hendry, Richard Barrett, Shashi Kanbur, Dave Clarke and Andy Wood have all allowed me to pester them with tedious questions, for which I am profoundly grateful.

Whether by helping out with day-to-day problems, giving useful snippets of advice or simply brightening up the world with their presence, many past and present members of the Physics and Astronomy department made my postgraduate education easier and

more enjoyable. Foremost amongst these is Aidan Keane, who endured sharing an office with me for nearly three years with characteristic cheerfulness, and in no particular order Andrew Conway, Chris Clarkson, Suzanne Martland, Guillian McArthur, David Keston, Susan Morrison, Victor Ameijenda, Scott McIntosh, Keith MacPherson, Sarah Matthews, Richard Smith, Rico Ignace, Alec MacKinnon, Giota Petkaki, Graham Woan, Paul Millar and Noelle Daly. I'm not sure I should really thank Peter Clive for introducing me to a whole new way to waste my time, but I will anyway, and of course a special mention is due to Daphne Davidson, the linchpin of the A & A group.

And finally, deepest thanks to my parents, John and Rosie Coleman, who have always cared for and supported me, even in doing something as crazy as astrophysics, and without whom this thesis would never have existed.

Chapter 1

Introduction

> It is to be *inferred* that there exist countless dark bodies close to the sun - such as we shall never see. This is, between ourselves, a parable; and a moral psychologist reads the whole starry script only as a parable and sign-language by means of which many things can be kept secret.
>
> Friedrich Nietzsche, *Beyond Good and Evil*

1.1 Dark matter in cosmology

The fact that most of the universe is apparently invisible can be rather unsettling. All our knowledge of the cosmos is derived from the light we can observe: for the bulk of matter to be dark implies a certain perverse sense of humour on Nature's part.

The first evidence for a substantial dark matter component in the Galaxy came from studies of galactic rotation curves. The distribution of visible matter - stars, gas and dust - in a spiral galaxy can be well represented by a two-component model, consisting of a flat thin disk and a massive central bulge. According to such a model, stars at a distance r far from the galactic centre should orbit at velocities proportional to $r^{-1/2}$ (from Kepler's 3rd Law). In fact, the rotation curves of our Galaxy and other spirals are flat at large r - the

velocity does not drop off with distance from the centre [1] [2]. This implies the existence of an unseen, roughly spherical halo component, comparable in mass to the entire visible part of the Galaxy.

Dynamical studies of galaxy clusters reveal even more dark matter. By measuring the velocity dispersion of the cluster galaxies one can estimate the mass contained within the cluster by means of the virial theorem [3]. Such calculations indicate a dark matter component which is an order of magnitude more massive than the visible galaxies [4].

An obvious question is: what does this dark matter consist of? There is an equally obvious answer in our own solar system. Far from any star a planet would be invisible, and it does not seem unreasonable to imagine a population of Jupiter-like objects or more massive brown dwarfs or stellar remnants making up the Galactic halo. These would be the so-called MAssive Compact Halo Objects, or MACHOs.

But this *cannot* be the whole story. The standard big bang model and observed light element abundances constrain the baryon density of the Universe to the range $0.007h^{-2} < \Omega_b < 0.022h^{-2}$ [5] (where Ω_b is the fraction of the critical density that is made up of baryons and $h = H_0/100\mathrm{kms}^{-1}\mathrm{Mpc}^{-1}$). Now this certainly implies a substantial quantity of baryonic dark matter, since the density of visible matter is only $\Omega_v = 0.003$ [6]. However, estimates of cluster dark matter give $\Omega \sim 0.2$ [7], which clearly implies that some type of exotic matter dominates on such lengthscales. Massive neutrinos are merely the most conservative suggestion.

Returning to our own Galaxy, the halo density is $\Omega_h \sim 0.02h^{-1}(R_h/70\mathrm{kpc})$ where R_h is the halo radius. Observationally, $R_h \gtrsim 70\mathrm{kpc}$ [8], so, if our Galaxy is typical, baryonic dark halos are just within big bang nucleosynthesis limits. Even if this constraint proves too tight (and a more typical halo radius might be $R_h \sim 200\mathrm{kpc}$ [9]) it is still reasonable to suppose that a substantial fraction of the dark matter in the halo is baryonic. Gas and molecular clouds are ruled out by X-ray observations and dynamical considerations [10] [11], so it seems likely a baryonic halo will consist of MACHOs.

Finding these compact, invisible objects is where the fun starts.

1.2 Gravitational lensing

The measurement of light deflection round the Sun [12] was the first true test of General Relativity (GR). Of course, one can obtain an expression for the deflection angle α of a light ray by a mass M by purely Newtonian means [13]: a particle with velocity v and distance of closest approach r will be gravitationally deflected through an angle given by

$$\tan\frac{\alpha}{2} = \frac{GM}{v^2 r} \tag{1.1}$$

Simply setting $v = c$ and considering small angles gives the "Newtonian" deflection angle

$$\alpha = \frac{2GM}{c^2 r} \tag{1.2}$$

The same value can be obtained from mass-energy equivalence in the context of Special Relativity; however, a full general relativistic treatment gives twice this angle,

$$\alpha = \frac{4GM}{c^2 r} \tag{1.3}$$

The experimental confirmation of the GR angle, and rejection of the Newtonian value, was a decisive test for General Relativity (and this event greatly influenced Popper's philosophy of science [14]). Einstein later showed [15] that light deflection can increase the apparent brightness of a source (after a suggestion by Mandl), but it was Zwicky [16] who first proposed that the lensing effect be used to determine the masses of galaxy clusters.

That, in a sense, is the prehistory of the field. Its history proper begins in 1964, when Refsdal [17] published a thorough treatment of the point mass lens. Lensing as a method for detecting dark matter was discussed by Press & Gunn [18], who proposed a search for double images of distant sources. However, the real breakthrough into the mainstream did not occur until 1979, when Walsh et al. discovered the first candidate for a lensed object - the doubly-imaged quasar Q0957+561A,B [19].

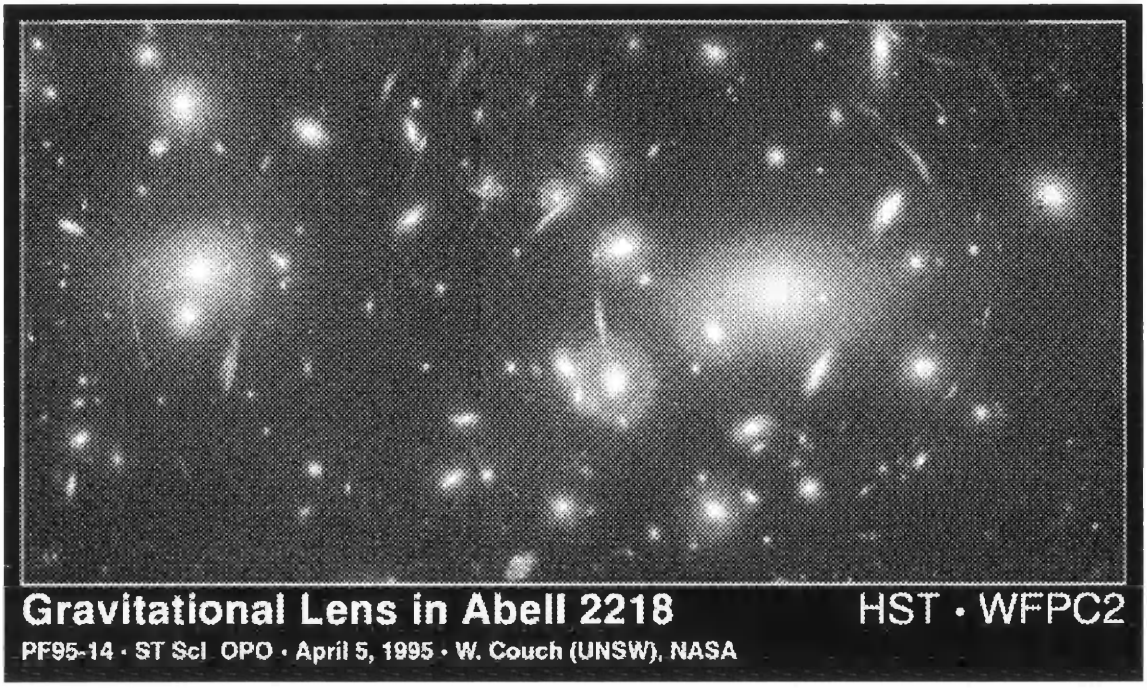

Figure 1.1: A Hubble Space Telescope image of lens arcs in the galaxy cluster Abell 2218

As will be shown below, a point mass will in general produce two images of the lensed object. The more closely aligned are the object, lens and observer, the more distorted the images until in the case of perfect alignment a single circular image is produced: the "Einstein ring". Q0957+561A and B lie 6.1 arcseconds apart on either side of a cluster galaxy at $z = 0.36$ (the quasar has redshift $z = 1.41$). Since 1979 a handful of other multiply-imaged quasars have been found [20], some with as many as four images, though the difficulties involved in confirming that two or more observed quasars are indeed the same object mean providing an authoritative number is impossible.

When the lensed images can be resolved, the distortion caused by lensing becomes apparent. This is most striking in the "radio rings", the Einstein rings formed by a compact radio source lying directly behind a galaxy. A less extreme, though more useful example can be seen in the lens arcs such as in Abell 370. These long, filamentary structures are the images of distant galaxies lensed by the deep potential well of cluster A370, and similar arcs have been identified in a number of other clusters. An HST image of cluster A2218

(Fig. 1.1) clearly shows the overall circular pattern of the lensed galaxies.

The importance of such arc structures lies in the fact that they allow a determination of the lensing potential, and thus the mass of the intervening cluster [21]. In the case of A370, a substantial dark matter component was identified.

Arc systems are merely the most blatant example of lensing by galaxy clusters. In the limit of weak lensing, the elliptical image of a distant galaxy is mapped into another ellipse [22]. However, although individual images do not appear distorted, the lensing is still apparent in the circular pattern imposed upon the field of galaxies. Given the unlensed orientations of the galaxies, one can invert to find the cluster potential. Unfortunately this information is not available, so a statistical study of large numbers of galaxies is required. It has been shown [23] that measurement of the direction of polarization of the lensed galaxies greatly improves the inversion, but this has not yet been put into practice.

1.3 Microlensing

Microlensing is more than just a smaller-scale version of lensing: it is a distinct theoretical and observational field in its own right. By definition, microlensing is a lensing configuration in which the multiple images are *unresolved*. Consequently, it can only be detected when the lens has a significant transverse velocity relative to the source, leading to a variation of the apparent source brightness with time. This is quite different from the distinction between strong and weak lensing. Microlensing is strong lensing: the "micro" refers to small angular separations between highly distorted images. In weak lensing the gradient of the amplification across the image is small. The fundamental distinction is clear: the lensing studies in section 1.2 involve static two-dimensional images, while microlensing concerns the analysis of one-dimensional time series.

Chang & Refsdal [24] discussed the basic concept in 1979, though the term "microlensing" was not coined until 1986 [25]. The earliest astrophysical results came from quasar observations. This is no coincidence. In a multiply-imaged quasar, if a brightness fluctuation in

one of the quasar images is not matched in the others the fluctuation cannot be due to intrinsic variability of the source. Microlensing is then a plausible explanation. Q2237+0305 is an ideal candidate, as it consists of four lensed images surrounding a nearby galaxy: a likely source of microlensing objects. Since 1988 [26] a handful of microlensing events have been seen in the images [27], allowing the stellar mass distribution in the lensing galaxy to be determined.

Presumably, therefore, some variability in single-image quasars could also be due to microlensing. On the basis of long time series quasar observations ($\sim$ 20 years), Hawkins [28] has claimed long-timescale variability ($\sim$ months) in most quasars and proposes that this is the result of routine microlensing by multiple objects, rather than intrinsic fluctuations in the quasars themselves. If correct, this implies a cosmological population of compact objects near the closure density - and therefore non-baryonic. Hawkins suggests that primordial black holes could make up this population, but his bold conjecture remains controversial.

In a highly influential 1986 paper [29], Paczyński proposed a large-scale variability survey of $\sim 10^6$ stars in the Large Magellanic Cloud (LMC), in order to detect compact objects in the Galactic halo by observing their microlensing effects. Several microlensing surveys are now in progress, and have met with considerable success. Their techniques and results will be discussed in section 1.5, but first a more quantitative treatment of microlensing is in order.

1.4 The Schwarzschild lens

A light ray which passes a mass M at a minimum distance r will be deflected through an angle

$$\alpha = \frac{4GM}{c^2 r} = \frac{2R_s}{r} \tag{1.4}$$

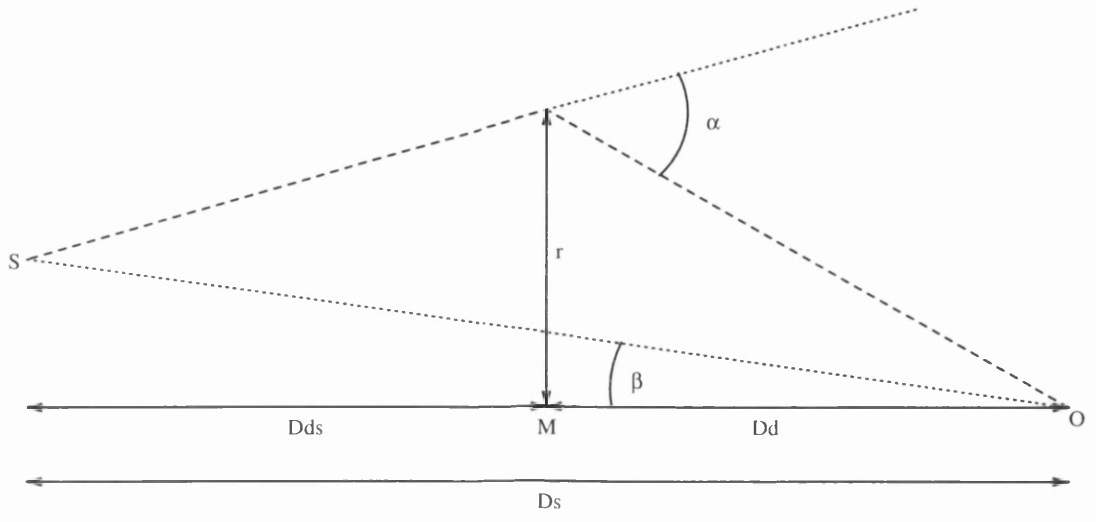

Figure 1.2: The geometry for a schwarzchild lens M and a source S at distances D_d and D_s respectively from the observer O

where R_s is the Schwarzschild radius of the lens.

From Fig. 1.2 it is clear that a ray which reaches the observer must satisfy the condition

$$\beta D_s = \frac{D_s}{D_d} r - \frac{2R_s}{r} D_{ds} \tag{1.5}$$

Denoting the angular distance between the lens and the observed ray by

$$\theta = \frac{r}{D_d} \tag{1.6}$$

we can rewrite Eqn. (1.5) as

$$\beta = \theta - 2R_s \frac{D_{ds}}{D_d D_s} \frac{1}{\theta}. \tag{1.7}$$

It is natural to introduce a characteristic angular scale, the *Einstein radius*, defined as

$$\theta_0 = \sqrt{2R_s \frac{D_{ds}}{D_d D_s}}. \tag{1.8}$$

This leads to a characteristic length scale in the source plane

$$\xi_0 = \theta_0 D_s = \sqrt{2R_s \frac{D_s D_{ds}}{D_d}}, \tag{1.9}$$

which we will refer to as the *projected Einstein radius.*

The lens equation Eqn. (1.7) can now simply be written

$$\theta^2 - \beta\theta - \theta_0^2 = 0 \tag{1.10}$$

with the solutions

$$\theta_{+,-} = \frac{1}{2}\left(\beta \pm \sqrt{4\theta_0^2 + \beta^2}\right). \tag{1.11}$$

We are now in a position to calculate the amplification of the source due to microlensing. Defining the normalised angles

$$\tilde{\theta} = \theta/\theta_0, \tag{1.12}$$

$$\tilde{\beta} = \beta/\theta_0 \tag{1.13}$$

the source has two images, at the positions

$$\tilde{\theta}_{+,-} = \frac{1}{2}\left(\tilde{\beta} \pm \sqrt{4 + \tilde{\beta}^2}\right). \tag{1.14}$$

As the intensity of a ray is constant along the ray path, the brightness ratio A of the source and image is simply equal to the ratio of surface areas, i.e.

$$A_{\pm} = \left|\frac{\tilde{\theta}_{\pm}}{\tilde{\beta}}\frac{\mathrm{d}\tilde{\theta}_{\pm}}{\mathrm{d}\tilde{\beta}}\right| \tag{1.15}$$

in the cylindrically symmetric case.

From Eqn. (1.14), the amplification factor for each image is therefore

$$A_{+} = \frac{1}{4}\left[\frac{\tilde{\beta}}{\sqrt{\tilde{\beta}^2 + 4}} + \frac{\sqrt{\tilde{\beta}^2 + 4}}{\tilde{\beta}} + 2\right] \tag{1.16}$$

and

$$A_{-} = \frac{1}{4}\left[\frac{\tilde{\beta}}{\sqrt{\tilde{\beta}^2 + 4}} + \frac{\sqrt{\tilde{\beta}^2 + 4}}{\tilde{\beta}} - 2\right]. \tag{1.17}$$

By definition, these two images cannot be resolved in the case of microlensing. Furthermore, the time delay between the images is of the order R_s/c [30], or 10μs for a $1M_{\odot}$

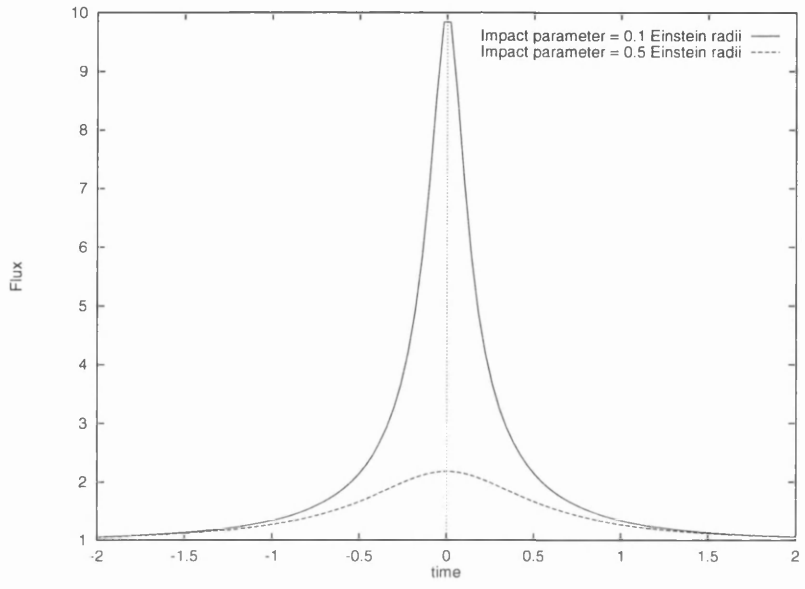

Figure 1.3: Two sample microlensing light curves.

lens. Therefore we can simply add the amplifications of the two images together to give the total amplification function

$$A(\tilde{\beta}) = \frac{1}{2}\left[\left(1+\frac{4}{\tilde{\beta}^2}\right)^{\frac{1}{2}} + \left(1+\frac{4}{\tilde{\beta}^2}\right)^{-\frac{1}{2}}\right]. \tag{1.18}$$

1.5 Microlensing surveys

We can now use these results to set some characteristic scales for microlensing. A point source at an angular distance of one Einstein radius from the lens will be amplified by a factor $A(\tilde{\beta}=1) = 3/\sqrt{5} \simeq 1.34$. In microlensing surveys this is set as the threshold brightness increase for consideration as a potential microlensing event. The timescale of a lensing event is simply the time taken for the lens to cross one Einstein radius, or

$$t = \frac{\theta_0 D_d}{v_\perp}, \tag{1.19}$$

where $v_\perp$ is the transverse velocity of the source.

Consider the lensing of a star in the LMC by a $1M_{\odot}$ MACHO in the Galactic halo. If the lens is half-way between Earth and the LMC, the images are separated by $\sim 10^{-3}$ arcsec, an unresolvable separation, and the lensing timescale is ~ 3 months if $V_{\perp} = 200\text{kms}^{-1}$. Observing such a microlensing event is therefore possible, but how likely are we to see it?

To answer this question it is useful to introduce the *microlensing optical depth*, τ. This is simply the instantaneous probability that a star is lensed such that $A > 1.34$, and can be written as

$$\tau = \int_0^{D_s} \frac{4\pi G}{c^2} \frac{D_d D_{ds}}{D_s} \rho(D_d)\, \mathrm{d}D_d \tag{1.20}$$

where $\rho(D_d)$ is the average density of lenses at a distance D_d. A commonly used halo model has the radial density profile

$$\rho(r) = \rho_0 \frac{R_0^2 + a^2}{r^2 + a^2} \tag{1.21}$$

where R_0 is the distance from the Sun to the Galactic centre, a is the halo core radius and ρ_0 is the local dark matter density. Inserting this profile and the LMC distance into Eqn. (1.20) yields a microlensing optical depth in the halo of $\tau_{halo} = 4.7 \times 10^{-7}$.

These numbers determine the parameters of microlensing surveys: the optical depth compels a survey to observe $\sim 10^{-6}$ stars, and the timescale makes several years of continuous observation necessary.

There are now several such surveys, but their methodologies are broadly similar. A suitable star field is monitored for variability, and a number of candidate microlensing events selected. This selection is far from trivial, as the cuts must discriminate microlensing from intrinsic variation in the source brightness. To be considered as a microlensing event, the fluctuation must satisfy the following criteria:

1. *Symmetry:* The microlensing light curve is symmetrical. This is unusual in stellar variability, and can be used as a rough indication of whether a particular event is

due to microlensing or intrinsic variability. The logical extension of this criterion is to demand that the data passes a threshold goodness of fit to the microlensing curve.

2. *Achromaticity:* The amplification function is frequency-independent, so one might expect the light curve to be the same in all wavelengths. In practice, the amplifications in two different wave bands are required to be the same.

3. *Uniqueness:* This is a slightly curious condition. After a candidate event has been identified, the object is subsequently monitored to see if the event recurs. Since the optical depth towards the bulge or LMC is $\sim 10^{-6}$, the chances of a single star being lensed more than once are tiny. Thus, any repeated variability is almost certainly intrinsic. There are two problems with this stipulation. Firstly, it is retrospective, so at any time a microlensing event may be retroactively disqualified. Secondly, a genuine microlensing event may be missed if it occurs to a star which also exhibits variability. Microlensing surveys generally avoid this possibility by simply removing known variable stars from consideration.

Each survey has its own "cuts", which further refine the selection process. These can be very involved, but the details can be crucial. A brief guide to the main surveys and their results follows: the references provide much more information on the analyses.

Note that the results quoted below are the claims made by the survey groups themselves. As we shall see later, there are complications, particularly extended source effects, which might bias these results in ways not accounted for in the published analyses. (Note, however, that the EROS group have consistently taken account of the effects of finite source size on the detection rate, and the MACHO group has recently folloed suit.)

1.5.1 The MACHO collaboration

The MACHO group has been monitoring the LMC, SMC and Galactic bulge since September 1992, during which time it has had dedicated use of the Great Melbourne Telescope

at Mount Stromlo.

The analysis of the first 2.1 years of LMC data has recently been published [31]. Eight microlensing events were detected, in a survey of 8.5 million stars, with timescales between 34 and 145 days. The main conclusions were:

1. The microlensing optical depth towards the LMC is $\tau_{halo} = 2.9^{+1.4}_{-0.9} \times 10^{-7}$ for events with timescales between 2 and 200 days.
2. The halo mass of MACHOs within 50 kpc is $2.0^{+1.2}_{-0.7} \times 10^{11} M_{\odot}$.
3. The most probable MACHO mass is $0.5^{+0.3}_{-0.2} M_{\odot}$.
4. Objects in the mass range $10^{-4} M_{\odot}$ to $0.03 M_{\odot}$ make up less than 20% of the dark halo.

A surprisingly large number of events has also been detected towards the bulge. A full analysis has not yet been published, but preliminary results based on the first season of bulge data (42 candidates) give $\tau_{bulge} = 3.92^{+3.17}_{-1.02} \times 10^{-6}$ [33]. This is significantly greater than the expected $\tau_{bulge} = 1 \times 10^{-6}$ [37], and may indicate a bar in our Galaxy. Such a bar would enhance the optical depth if its long axis were oriented roughly towards Earth.

1.5.2 OGLE

The Optical Gravitational Lensing Experiment has only monitored the bulge, and has been doing so since 1992 using the 1m Swope telescope at Las Campanas. A full analysis of the first two years of data is in broad agreement with the MACHO bulge results [34]. In a survey of over a million stars ($\sim 1.1 \times 10^6$ in 1992 and $\sim 1.4 \times 10^6$ in 1993), 9 microlensing events were detected, with timescales between 8.6 and 62 days. The resulting optical depth is $\tau_{bulge} = (3.3 \pm 1.2) \times 10^{-6}$ for events in this timescale range. As with the MACHO results, this large optical depth implies the existence of a Galactic bar.

1.5.3 EROS

The EROS group ("Expérience pour la Recherche d'Objets Sombres") has been comparatively unfortunate. The survey has involved two telescopes at La Silla: a CCD-equipped 40cm telescope looking for short timescale events (15 minutes $\lesssim t \lesssim$ a few days) and the 1m Schmidt, sensitive to events in the range 1 day $\lesssim t \lesssim$ a few months. One year of the CCD time was spent on the SMC; the rest of the survey was only concerned with the LMC.

No short timescale events were seen. Only two candidate events were identified in the Schmidt data. The first candidate has subsequently been identified as a Be star [35], and the second as an eclipsing binary [36]. Thus there is considerable doubt as to whether these are real microlensing events, rather than intrinsic variability of the source.

Given the lack of *any* very reliable events, the EROS conclusions must necessarily be limited. Even so, the absence of short duration events provides an upper limit of 20% to be set on the fraction of objects in the halo with masses between $10^{-7}M_{\odot}$ and $0.02M_{\odot}$. This is consistent with the MACHO results, but extends to a much lower mass limit.

1.5.4 DUO

The DUO project is the last of the "established" microlensing surveys. It is concerned with determining the spatial distribution of lenses toward the Galactic center, and employs the ESO 1m Schmidt telescope in a survey of between 6 and 13 million stars. So far 12 candidate events have been reported, including one binary event, which are apparently concentrated at low Galactic latitude [38].

1.5.5 Other projects

When microlensing surveys were first proposed, there was considerable scepticism about their feasibility. The successes outlined above have inspired further projects, expanding and refining the current techniques. MOA (Microlensing Observations in Astrophysics) is

a new New Zealand / Japan microlensing collaboration; PLANET (Probing Microlensing Anomalies NETwork) uses four semi-dedicated telescopes to follow up microlensing alerts with rapidly-sampled photometric measurements and AGAPE (Andromeda Galaxy and Amplified Pixels Experiment) looks for microlensing of unresolved stars in the Andromeda galaxy. Microlensing is a rapidly expanding field - so much so that this review will already be out of date.

There has also been a substantial scientific payoff for the field of variable stars. In the process of identifying and winnowing out a few microlensing events from the surveys, the various groups have created a massive catalogue of intrinsic stellar variability. Astronomers with interests in Cepheids, RR Lyraes and eclipsing binaries have not been slow to exploit this dataset.

1.6 Complications

The results outlined above are affected by many complicating factors: timescale limitations, blending, complex lens systems and extended source effects. Some of these are simply problems, while others are opportunities in disguise. We shall consider them in turn.

1.6.1 Timescale limitations

The timescale of a microlensing event can in principle take on any value between zero and infinity. In practice, microlensing surveys can only detect events within a finite range of timescales: the precise limits depend on the details of the individual survey, but a range of a few days to a few hundred days is typical. At the extreme ends of the range, the detection efficiency becomes very low.

Since the timescale is a function of the lens mass, this imposes a limit on the range of MACHO masses that can be detected. This limitation is well understood, however, and the quoted results generally include the appropriate caveats.

1.6.2 Blending

Microlensing surveys cover very crowded fields of stars, in order to maximise the probability of seeing an event. But there is a danger, especially in such a dense field, that an apparently single star may be in fact two stars whose separation is unresolvable. If one of these stars is lensed, the resulting light curve will be contaminated by the light from the other star, introducing chromaticity and an additional baseline flux [39], and systematicallyreducing the lensing timescale. Blending can be taken into account by adding extra parameters to the light curve fitting [31]: however, a highly blended event may not be recognised as microlensing at all.

1.6.3 Complex lenses

So far, we have only considered single, point mass lenses. Extending the discussion to a binary lens produces radically new results. It can be shown [40] that the amplification function of two coplanar point mass lenses includes caustic curves, along which the magnification is infinite. (In the single lens case, the caustics collapse to a point at the lens position.) Fig. 1.4 shows an example of the light curve produced by such a binary lens. It can be seen that, while the magnification is very high during caustic crossing, the light curve is very different from the standard single lens case.

This is a problem, because many such events will not fit the survey criteria for microlensing candidates (though a few binary events have been detected: OGLE#7, DUO#2 and MACHO LMC#9). It is also an opportunity, as it presents a new way to detect extrasolar planets. In the case where one mass is very large compared to the other, the resulting light curve resembles the "canonical" curve, but with spiky features caused by the small orbiting mass (or masses). This has been proposed as a signature of planetary systems [41].

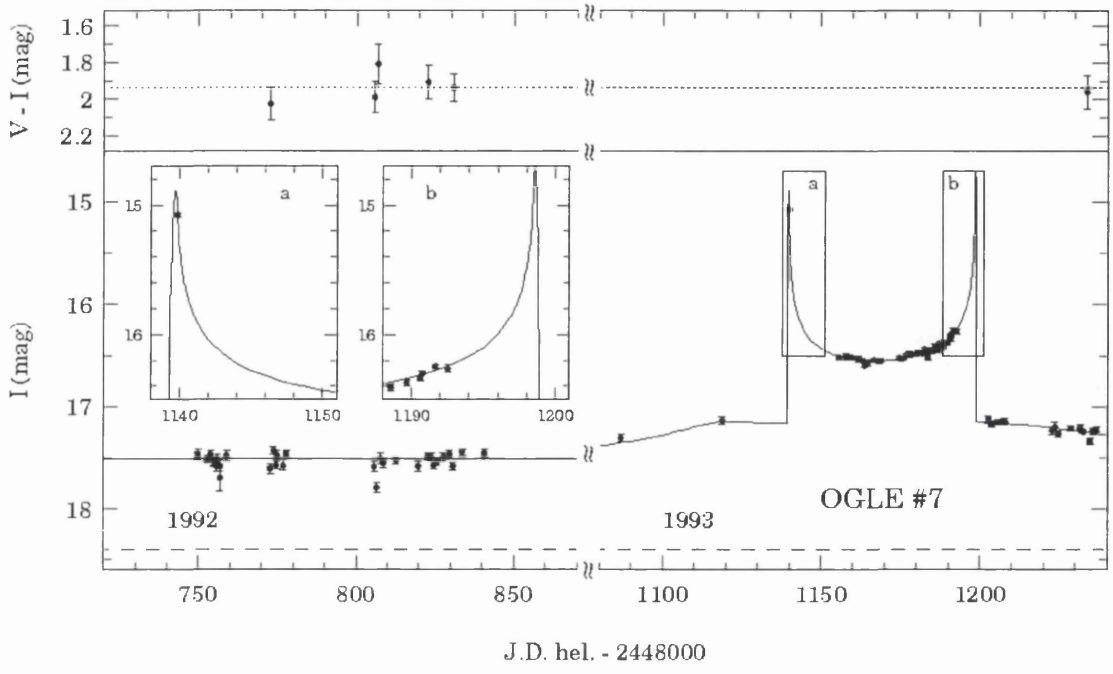

Figure 1.4: A binary microlensing event, OGLE#7, detected by the OGLE survey

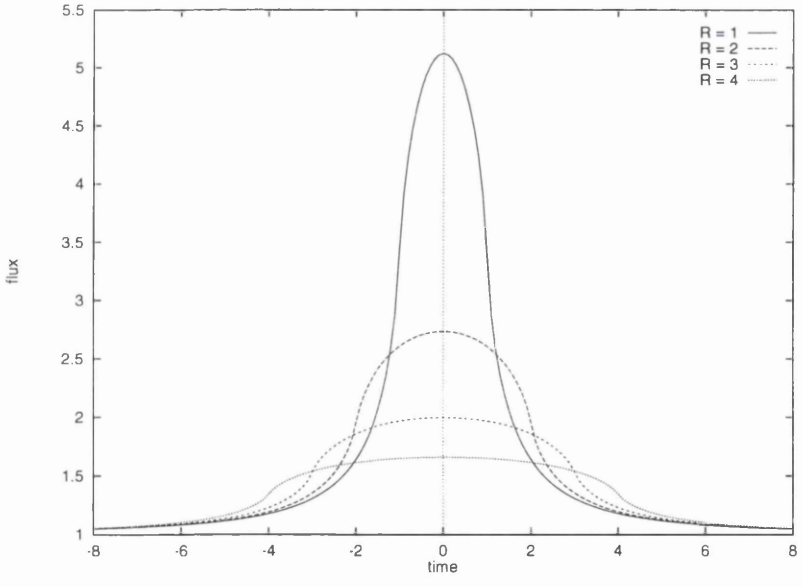

Figure 1.5: The effect of finite source size on the microlensing light curve. The source object is spherical, of radius R in units of the lens Einstein radius, and of uniform brightness

1.6.4 Extended sources

The point-source approximation breaks down if the source size is comparable to the Einstein radius. This has serious consequences for microlensing surveys: as we shall see in this section, there are a number of effects which can cause extended-source microlensing to go undetected in the data. Clearly, this will lead to a systematic underestimation of the lensing optical depth. On the other hand, we can exploit extended source effects to learn more about the lens - and about the source object itself.

When we abandon the point-source model, obtaining a theoretical light curve becomes somewhat more involved: the amplification must be integrated over the source so that the total flux at a given time, $F_\nu(t)$ is given by

$$F_\nu(t) = \int\int_{source} I_\nu(r,\theta) A(r,\theta,t)\, r\, \mathrm{d}r\, \mathrm{d}\theta \tag{1.22}$$

where (r,θ) are radial coordinates in the source plane, and $I_\nu(r,\theta)$ is the specific intensity.

This now opens up a remarkable set of possibilities. Any source structure (as expressed in $I(r,\theta)$ will be expressed in the light curve $F(t)$.

To start with the simplest case, consider a spherical source of radius R and uniform intensity I_0 [42], [43]. If R is of the same order of magnitude as the projected einstein radius of the lens, the microlensing light curve will depart from the point-source curve as shown in Fig. 1.5. The flux begins to rise sooner for greater R, as the nearest edge of the source begins to be lensed, but for small impact parameters the maximum flux is lower since the amplification is effectively smeared out over the source. For sufficiently large R the amplification will never meet the threshold for detection by the microlensing surveys. It has been shown [70] that events where $R \gtrsim 3\xi_0$will go undetected. This reduces the sensitivity of the surveys to low-mass lenses, and sets a lower bound of $\sim 10^{-7} M_\odot$ on detectable lenses. The EROS survey has made some attempt to take this into account [44]: the MACHO group has recently started doing the same.

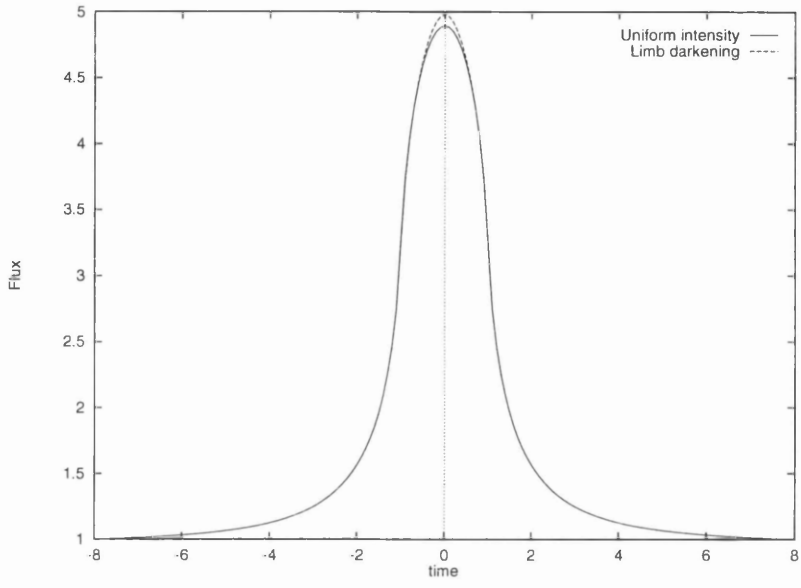

Figure 1.6: The effect of limb darkening on the microlensing light curve. The intensity at the limb of the darkened star is 0.9 times the intensity at the center of the disk (and 0.9 times the intensity at all points on the disk of the uniformly intense star).

While this is indeed a problem, detecting the effects of finite source size in the light curve can be immensely useful in constraining the lens parameters. The light curve gives the relationship between R and ξ_0: if R can be determined spectroscopically, we immediately have an absolute scale for the lens mass, distance and velocity. The significant improvement this makes to our information about the lens has been examined by Peng [45].

If we now let I vary across the disk, we can see that corresponding fine structure appears in the light curve due to differential amplification across the source. The lens effectively acts like a magnifying glass passing across the disk. Fig. 1.6 shows the effect of limb darkening: further calculations can be found in [70] and [47]. In general, we might also expect colour variations across the stellar disk to manifest themselves as differences in the observed amplification in different wavebands, as well as in the behaviour of particular spectral lines during the microlensing event. Valls-Gabaud has calculated these effects in detail [47].

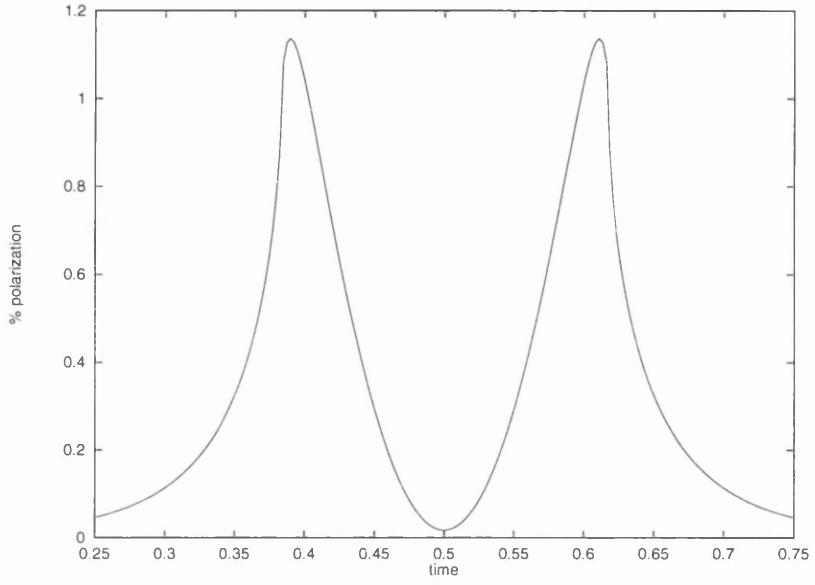

Figure 1.7: An example of a polarimetric signal induced by microlensing.

The astute reader will realise that this opens up a wonderful opportunity for stellar imaging. We can use the fine detail of the microlensing light curve to reconstruct $I_\nu(r, \theta)$; in other words, to put together a picture of the stellar disk. This possibility has been noted by a number of authors ([70], [48], [47], [49]), in the context both of stellar atmospheres and of quasar accretion disks. The practicalities of this process have hitherto received little attention, however: just how does one go about determining stellar atmosphere profiles from the light curve, and what kind of information can be obtained? Chapter 6 of this thesis answers these questions.

Polarization is another feature of the stellar limb that may be picked up by microlensing. Differential amplification of a star with some degree of limb polarization can give rise to dramatic variable polarization signatures (as in Fig. 1.7), even when the star normally exhibits no net polarization [70]. Just as with the unpolarized flux from an extended source, this can help pin down the parameters of the lensing object: furthermore, polarimetric measurements show the direction of transverse motion of the lens. In fact, the extent to which the polarization signal constrains the lens parameters is very striking [50]: while a polarimetric microlensing survey is not feasible, polarimetric follow-up observations of

microlensing alerts could prove very valuable. The major factor affecting the practicality of such measurements is the degree of limb polarization in the source star: if this is too low, the polarization signal will be too weak to be detected.

It is hard to say how good the prospects are for such studies, as measuring stellar limb polarization observationally is a difficult task. The basic problem is that one needs a way of resolving a part of the stellar disk, which is only possible under special circumstances - such as an eclipsing binary system. Determining the limb polarization of an eclipsing binary star is discussed in some detail in Chapter 5 of this thesis, where we shall see that it has similarities to the microlensing problem. However, it is clear that stars with extended scattering envelopes are the best candidates for producing strong polarization signatures when lensed. Not only are they physically large, so that $R \sim \xi_0$ for typical parameters, but they also emit strongly polarized light from their scattering regions.

Accordingly, we begin this thesis by developing a stellar envelope model from scratch, and in Chapter 3 we shall see the effects of microlensing on such an object.

Chapter 2

A generic model of extended stellar envelopes

> Can you bind the chains of the Pleiades, or loose the cords of Orion?
>
> Job 38: 31

2.1 Motivation

Measuring variable polarization induced by microlensing can be immensely useful. Simply having an additional light curve provides much tighter constraints on the lens parameters, and polarization is the only property of the observed flux which can establish the direction of lens motion. Furthermore, the effect of the finite source radius can be much more pronounced in the polarized flux.

The only problem is the relative difficulty of making polarimetric measurements. This is not just because of the need to measure the polarized flux in two directions, but also because the signal is typically much weaker than the unpolarized flux. This is why polarimetric microlensing surveys are not presently feasible: follow-ups to microlensing alerts are the favoured way of exploiting the phenomenon. Even so, for main sequence stars the

signal may be unmeasurably feeble, especially if the more pessimistic estimates of limb polarization are correct.

One way round this obstacle is to concentrate on those stars which are likely to give the strongest polarization signal when lensed. Stars with extended scattering envelopes are good candidates, as the intrinsic polarization in the envelope can be relatively high.

Simplistically speaking, the polarization arises from the optically thin layers of the atmosphere, as multiple scattering will usually tend to have a depolarizing effect. In stars on the main sequence, this region is very thin and so limb polarization is restricted to the edge of the stellar disk [74]. However, in giant stars a substantial optically thin component can extend to several stellar radii beyond the photosphere. The principal scatterers in this envelope may be electrons (in a hot object such as a Be star) or dust particles (in a red giant). In either case, a considerable line-of-sight polarization may be expected.

When such an object is lensed, this line-of-sight polarization will produce a net polarimetric signal as a result of differential amplification. Not only is the intrinsic polarization larger than in the case of a main sequence star, but also the main scattering region is further removed from the primary source of unpolarized intensity. For both these reasons, the induced polarization will be paricularly high. Furthermore, the red giant case can be expected to exhibit chromaticity, as scattering from dust is wavelength-dependent.

In this chapter we develop a fairly simple model stellar atmosphere from first principles, which can be applied to a wide range of stellar types. In the following chapter we go on to calculate the polarimetric light curves produced by a variety of microlensing effects. This will indicate the degree of polarization which an extended star may produce when lensed, and show how the envelope structure is reflected in the shape of the light curve. We assume a basic familiarity with the Stokes parameters I, Q, U and V: the uninitiated will find enlightenment in Appendix A.

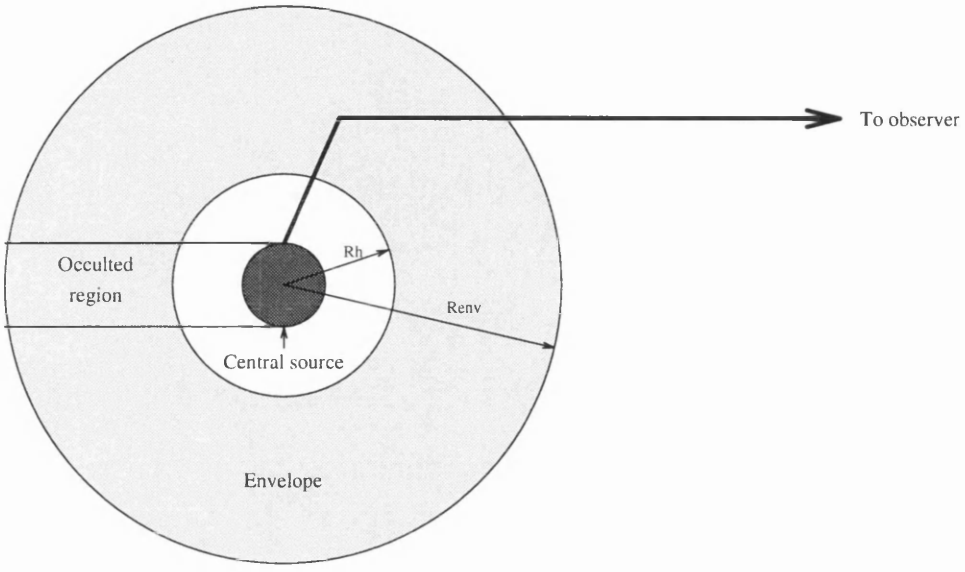

Figure 2.1: The model stellar atmosphere.

2.2 A model stellar envelope: one size fits all

In this chapter we shall take our extended source to be spherically symmetric, and shall assume that the stellar envelope is an optically thin Thomson scattering envelope, illuminated by a finite spherical photosphere of uniform intensity at its centre (Fig. 2.1). The central source has radius R_0, and the envelope is of radius R_{env}. There are no scatterers between R_0 and a boundary radius R_h: the scatterers follow a power law in number density between R_h and R_{env}. The region between R_0 and R_h is considered to be optically thin.

With $R_h = R_0$ this model can represent a hot star with an extended electron scattering envelope. Such stars are relatively rare, but their high intrinsic brightness makes them otherwise promising microlensing candidates. The major approximations in this model are spherical symmetry and low optical depth. The latter is valid for many high-temperature circumstellar envelopes, which commonly have optical depths ~ 0.1 to 0.3. Spherical symmetry is more contentious, in that the envelope may have a flattened, disk-like geometry rather than a near-spherical shape [54]: such a case will not be considered further in this

chapter, though we will return to it near the end of Chapter 3.

If we set $R_h \sim$ a few R_0 we obtain a basic model of a red giant star. In this case the scatterers are dust, and the region close to the stellar surface is too hot for dust particles to exist. In this case the scattering cross-section has an additional λ^{-4} wavelength dependence. In principle, the Heyney-Greenstein scattering function would be more appropriate for this envelope. However, this will not be used in these calculations in the interest of mathematical and computational simplicity.

Red giants are prime microlensing candidates: indeed, many of the events observed to date in the Galactic bulge have had red giants as sources. Typical optical depths for these envelopes ~ 0.2 to 0.6: the radius at which dust forms depends on the dust condensation temperature and the photospheric temperature of the star, but for realistic parameters will be in the range 3 to 7 stellar radii [55].

Consider a particle at position (x, y, z) with position vector $\mathbf{r}$ in a coordinate system with the origin at the centre of the star and the z-axis in the direction of the observer. This is the source frame $(\mathbf{e}_x, \mathbf{e}_y, \mathbf{e}_z)$. We can define another reference frame $(\mathbf{e}'_x, \mathbf{e}'_y, \mathbf{e}'_z)$ centred on the particle, with the y'-axis parallel to the y-axis, and the z'-axis aligned along $\mathbf{r}$. Both these frames can also be described by polar coordinates (r, θ, ϕ) and (r', θ', ϕ'), which are related to the Cartesian coordinates in the usual way.

From Fig. 2.2 it can be seen that the source frame and the particle frame are related by

$$\mathbf{e}_z = -\sin\theta\mathbf{e}'_x + \cos\theta\mathbf{e}'_z \tag{2.1}$$

$$\mathbf{e}_x = \cos\theta\mathbf{e}'_x + \sin\theta\mathbf{e}'_z \tag{2.2}$$

$$\mathbf{e}'_z = \cos\theta\mathbf{e}_z + \sin\theta\mathbf{e}_x \tag{2.3}$$

$$\mathbf{e}'_x = -\sin\theta\mathbf{e}_z + \cos\theta\mathbf{e}_x \tag{2.4}$$

since $\mathbf{e}'_z = \hat{\mathbf{r}}$ and $\mathbf{e}'_y = \mathbf{e}_y$.

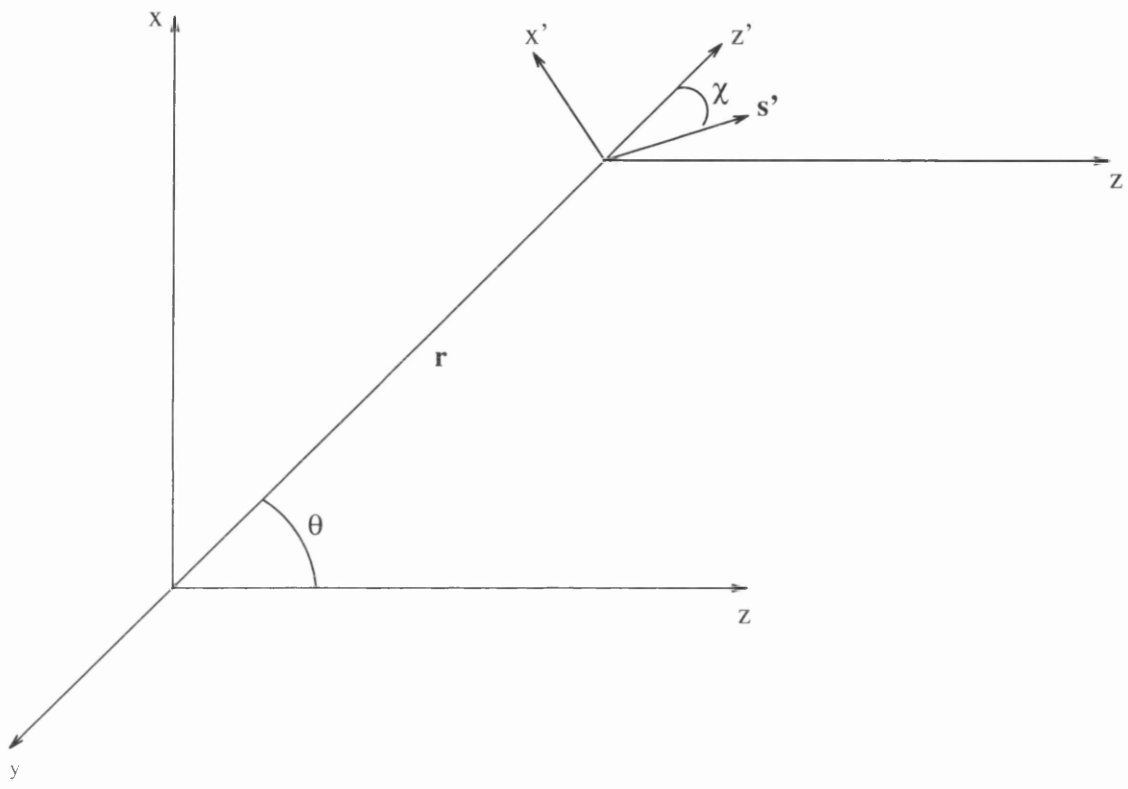

Figure 2.2: The scattering geometry. This figure shows the special case where **r** is in the $x - z$ plane. The observer is at $z = \infty$.

Now consider radiation incident upon the particle from direction $\mathbf{s}'$, and scattered into the direction $\mathbf{e}_z$, that is, towards the observer. Together, $\mathbf{s}'$ and $\mathbf{e}_z$ define the scattering plane. Writing $\mathbf{s}'$ in the particle frame basis,

$$\mathbf{s}' = \sin\theta'\cos\phi'\mathbf{e}'_x + \sin\theta'\sin\phi'\mathbf{e}'_y + \cos\theta'\mathbf{e}'_z \tag{2.5}$$

so the scattering angle χ is given by

$$\cos\chi = \mathbf{s}'\cdot\mathbf{e}_z = -\sin\theta'\cos\phi'\sin\theta + \cos\theta'\cos\theta \tag{2.6}$$

Let $\tilde{\phi}$ be the angle of the scattering plane to the $x-z$ plane. Then

$$\cos\tilde{\phi} = \frac{(\mathbf{e}_z\times\mathbf{s}')\cdot\mathbf{e}_y}{|\mathbf{e}_z\times\mathbf{s}'|} = \frac{(\mathbf{e}_z\times\mathbf{s}')\cdot\mathbf{e}_y}{\sin\chi} \tag{2.7}$$

Now

$$\mathbf{e}_z\times\mathbf{s}' = \sin\theta'\cos\phi'\mathbf{e}_z\times\mathbf{e}'_x + \sin\theta'\sin\phi'\mathbf{e}_z\times\mathbf{e}'_y + \cos\theta'\mathbf{e}_z\times\mathbf{e}'_z \tag{2.8}$$

$$= \sin\theta'\cos\phi'\cos\theta\mathbf{e}'_y + \cos\theta'\sin\theta\mathbf{e}'_y \tag{2.9}$$

giving

$$\cos\tilde{\phi} = \frac{\sin\theta'\cos\phi'\cos\theta + \cos\theta'\sin\theta}{\sin\chi} \tag{2.10}$$

Similarly

$$\sin\tilde{\phi} = -\frac{\sin\theta'\sin\phi'}{\sin\chi} \tag{2.11}$$

To obtain the scattered Stokes parameters at a point on the stellar disk we must integrate the contributions from all volume elements along the line of sight. In this optically thin model, only single scattering is considered.

$$I_{sc} = \int_{-\infty}^{\infty} dz \int_{4\pi} f_1(\mathbf{e}_z, \mathbf{s}') I(\mathbf{r}, \mathbf{s}') n(\mathbf{r}) \sigma \, d\Omega_{s'} \tag{2.12}$$

$$U_{sc} = \int_{-\infty}^{\infty} dz \int_{4\pi} f_2(\mathbf{e}_z, \mathbf{s}') I(\mathbf{r}, \mathbf{s}') n(\mathbf{r}) \sigma \cos 2\tilde{\phi} \, d\Omega_{s'} \tag{2.13}$$

$$Q_{sc} = \int_{-\infty}^{\infty} dz \int_{4\pi} f_2(\mathbf{e}_z, \mathbf{s}') I(\mathbf{r}, \mathbf{s}') n(\mathbf{r}) \sigma \sin 2\tilde{\phi} \, d\Omega_{s'} \tag{2.14}$$

where

$$f_1(\mathbf{e}_z, \mathbf{s}') = \frac{3}{16\pi}(1 + \cos^2 \chi) \tag{2.15}$$

$$f_2(\mathbf{e}_z, \mathbf{s}') = \frac{3}{16\pi}(\sin^2 \chi) \tag{2.16}$$

and $n(\mathbf{r})$ and σ are the number density and cross-section respectively of the scattering particles.

In the spherically symmetric case we have

$$I(\mathbf{r}, \mathbf{s}') = I(r, \theta') \tag{2.17}$$

$$n(\mathbf{r}) = n(r) \tag{2.18}$$

Introducing these simplifications and transforming coordinates from z to r yields

$$I_{sc}(a) = 2 \int_a^{\infty} \frac{r \, dr}{\sqrt{r^2 - a^2}} \int_0^{2\pi} \int_0^{\pi} f_1 I(r, \theta') n(r) \sigma \sin \theta' \, d\theta' \, d\phi' \tag{2.19}$$

$$U_{sc}(a) = 2\int_a^\infty \frac{r\,dr}{\sqrt{r^2-a^2}}\int_0^{2\pi}\int_0^\pi f_2 I(r,\theta')n(r)\sigma\cos 2\tilde{\phi}\sin\theta'\,d\theta'\,d\phi' \qquad (2.20)$$

$$Q_{sc}(a) = 2\int_a^\infty \frac{r\,dr}{\sqrt{r^2-a^2}}\int_0^{2\pi}\int_0^\pi f_2 I(r,\theta')n(r)\sigma\sin 2\tilde{\phi}\sin\theta'\,d\theta'\,d\phi' \qquad (2.21)$$

where a is the radial coordinate across the stellar disk such that $r^2 = a^2 + z^2$.

Consider U_{sc} and Q_{sc}.

$$\begin{aligned}
U_{sc}(a) &= 2\int_a^\infty \frac{r\,dr}{\sqrt{r^2-a^2}}\int_0^{2\pi}\int_0^\pi \frac{3}{16\pi}(\sin^2\chi)I(r,\theta')n(r)\sigma(\cos^2\tilde{\phi}-\sin^2\tilde{\phi})\sin\theta'\,d\theta'\,d\phi' \\
&= \frac{3\sigma}{8\pi}\int_a^\infty \frac{rn(r)\,dr}{\sqrt{r^2-a^2}}\int_0^\pi I(r,\theta')[\pi\sin^2\theta'\cos^2\theta + 2\pi\cos^2\theta'\sin^2\theta - \pi\sin^2\theta']\sin\theta'\,d\theta' \\
&= \frac{3\sigma}{8}\int_a^\infty \frac{rn(r)\,dr}{\sqrt{r^2-a^2}}\int_0^\pi I(r,\theta')[-\sin^2\theta'\sin^2\theta + 2\cos^2\theta'\sin^2\theta]\sin\theta'\,d\theta' \\
&= \frac{3\sigma}{8}\int_a^\infty \frac{rn(r)\,dr}{\sqrt{r^2-a^2}}\int_0^\pi I(r,\theta')\sin^2\theta[2-3\sin^2\theta']\sin\theta'\,d\theta' \qquad (2.22)
\end{aligned}$$

Clearly $Q_{sc} \equiv 0$.

Now $I(r,\theta') = I_0$ for $\theta' \le \alpha$ (where $\sin\alpha = R_0/r$). Thus

$$\begin{aligned}
\int_0^\pi I(r,\theta')[2-3\sin^2\theta']\sin\theta'\,d\theta &= I_0\int_0^\alpha 2\sin\theta' - 3\sin^3\theta'\,d\theta' \\
&= I_0[\cos\alpha - \cos^3\alpha] \qquad (2.23)
\end{aligned}$$

which gives

$$U_{sc}(a) = I_0\frac{3\sigma}{8}\int_a^\infty \frac{n(r)r}{\sqrt{r^2-a^2}}\frac{a^2}{r^2}[\cos\alpha - \cos^3\alpha]\,dr \qquad (2.24)$$

where $\cos\alpha = \sqrt{r^2 - R_0^2}/r$.

The calculation for I_{sc} is a little messier.

$$
\begin{aligned}
I_{sc}(a) &= 2\int_a^\infty \frac{r\,dr}{\sqrt{r^2-a^2}}\int_0^{2\pi}\int_0^\pi \frac{3}{16\pi}(1+\cos^2\chi)I(r,\theta')n(r)\sigma\sin\theta'\,d\theta'\,d\phi' \\
&= \frac{3\sigma}{8\pi}\int_a^\infty \frac{rn(r)\,dr}{\sqrt{r^2-a^2}}\int_0^\pi I(r,\theta')[2\pi+\pi\sin^2\theta'\sin^2\theta+2\pi\cos^2\theta'\cos^2\theta]\sin\theta'\,d\theta' \\
&= \frac{3\sigma}{8}\int_a^\infty \frac{rn(r)\,dr}{\sqrt{r^2-a^2}}\int_0^\pi I(r,\theta')[2\sin\theta'+\sin^3\theta'\sin^2\theta+2\sin\theta'\cos^2\theta'\cos^2\theta]\,d\theta' \\
&= I_0\frac{3\sigma}{8}\int_a^\infty \frac{rn(r)\,dr}{\sqrt{r^2-a^2}}\int_0^\alpha[(2+\sin^2\theta)\sin\theta'+(2\cos^2\theta-\sin^2\theta)\cos^2\theta'\sin\theta']\,d\theta' \\
&= I_0\frac{3\sigma}{8}\int_a^\infty \frac{n(r)r}{\sqrt{r^2-a^2}}[(2+\frac{a^2}{r^2})(1-\cos\alpha)+\frac{(2r^2-3a^2)}{3r^2}(1-\cos^3\alpha)]\,dr \qquad (2.25)
\end{aligned}
$$

2.3 Intensity and polarization profiles

We now have all the components of a model stellar envelope, and have gone as far as we can analytically. The integrals in Eqn. (2.24) and Eqn. (2.25) must be solved numerically, with the density profile $n(r)$ specified. In these models,

$$
n(r) = \begin{cases} 0 & : \quad r < R_h \\ n_0(\frac{r}{R_0})^{-\beta} & : \quad R_h \le r \le R_{env} \\ 0 & : \quad r > R_{env} \end{cases} \qquad (2.26)
$$

The parameter n_0 is set by specifying the optical depth τ of the envelope at the centre of the stellar disk. This is defined by

$$
\tau = \sigma\int_{R_h}^\infty n(r)\,dr = n_0\sigma\int_{R_h}^\infty (r/R_0)^{-\beta}\,dr,
$$

yielding

$$
R_0 n_0\sigma = \tau(\beta-1)(R_h/R_0)^{(\beta-1)}.
$$

Note that the scattered intensities are therefore linearly dependent on the optical depth, in this optically thin approximation. In the figures in this chapter and the next, we take

$\tau = 0.1$. This is at the low end of the range of optical depths for circumstellar envelopes: to obtain the results for higher optical depths, the intensity axes can simply be scaled by the appropriate factor. Of course, as τ approaches 1, the model breaks down and one would have to solve the full equation of radiative transfer or carry out a Monte-Carlo simulation.

A fourth order Runge-Kutta integration of Eqns. 2.24 and 2.25 (with adaptive step size) yields intensity and polarization profiles as shown in Figs. 2.3 to 2.11.

Fig. 2.3 shows the scattered intensity profile for $R_h = R_0$, i.e. a star with a hot electron scattering atmosphere. I_{sc} peaks close to the photosphere of the central source, at $r \sim 1.5R_0$, and is only ever $\sim$ a few % of the direct intensity I_0. The shape of the profile is dictated by two competing factors. As the radial coordinate r increases, the length of the effective scattering region along the line of sight increases while the number density and incident luminosity decrease. The profile has a maximum where these two trends balance. The location of this maximum also depends on the scattering function, which in this case has a peak for forward scattering. Consequently, the peak in scattered intensity occurs close to the source where the scattering angle is small.

R_h increases in Figs. 2.4 to 2.6, representing dusty red giant envelopes with internal ionised regions of varying extents. The profiles here are smaller and broader, with the peak pushed further out as R_h increases. We can now clearly see the step at $r = R_0$ due to occultation by the central source - this step exists in Fig. 2.3, but is practically imperceptible.

The profiles for U_{sc}, the polarized intensity, are shown in Figs. 2.7 to 2.10. Qualitatively, the profiles are similar to the I_{sc} curves, as the same factors govern both. The main difference is that the contribution from the forward scattering to the polarized flux is very weak in this case, so the effect of occultation is much less pronounced. However, the peaks in each case are at the same locations as in the corresponding I_{sc} profiles. Clearly the difference between the polarized and unpolarized scattering functions has only a small effect on the position of the peak.

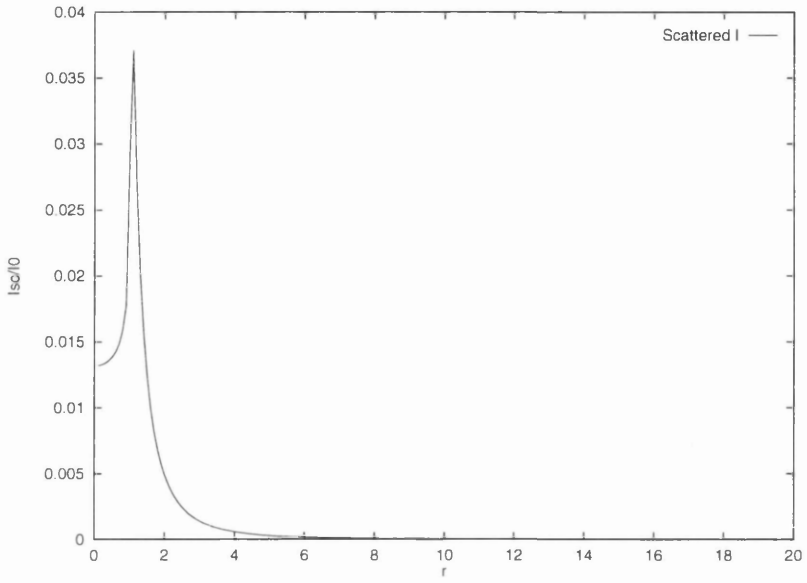

Figure 2.3: I_{sc} as a function of radial coordinate (in units of R_0) across the stellar disk. Here $R_h = R_0$. (Optical depth $\tau = 0.1$.)

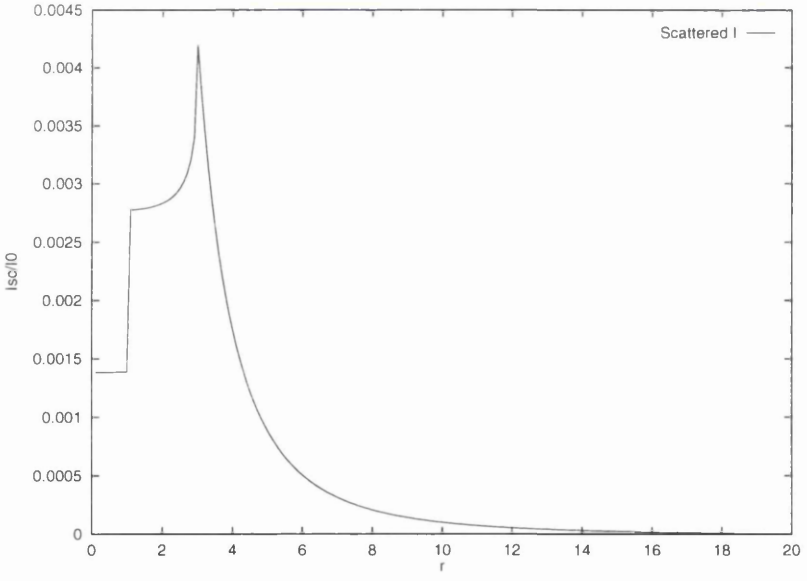

Figure 2.4: I_{sc} as a function of radial coordinate (in units of R_0) across the stellar disk. Here $R_h = 3R_0$. (Optical depth $\tau = 0.1$.)

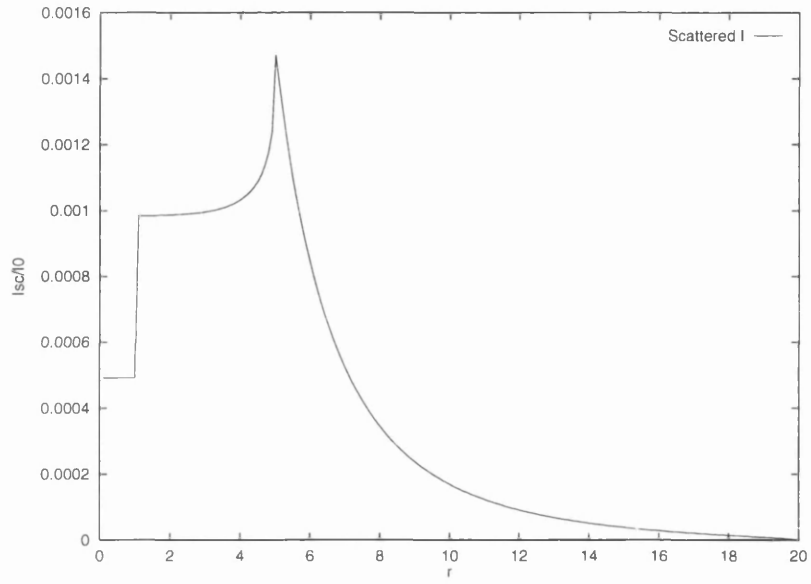

Figure 2.5: I_{sc} as a function of radial coordinate (in units of R_0) across the stellar disk. Here $R_h = 5R_0$. (Optical depth $\tau = 0.1$.)

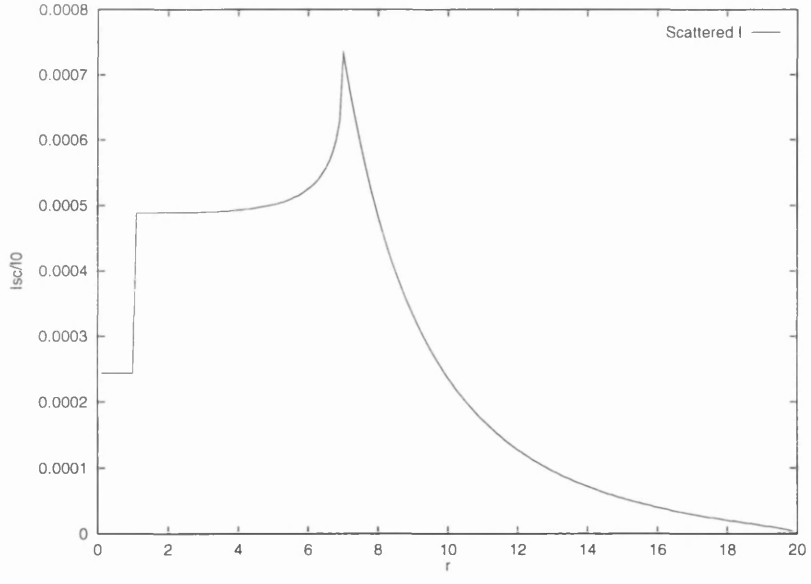

Figure 2.6: I_{sc} as a function of radial coordinate (in units of R_0) across the stellar disk. Here $R_h = 7R_0$. (Optical depth $\tau = 0.1$.)

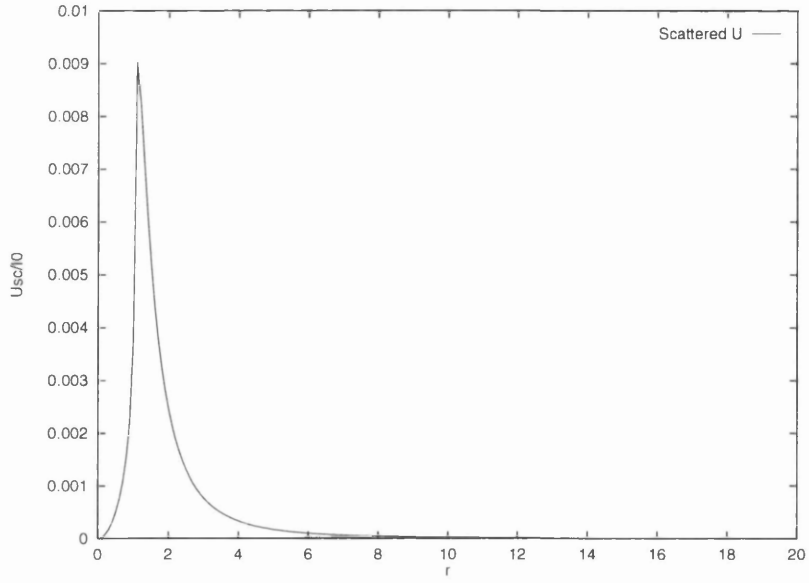

Figure 2.7: U_{sc} as a function of radial coordinate (in units of R_0) across the stellar disk. Here $R_h = R_0$. (Optical depth $\tau = 0.1$.)

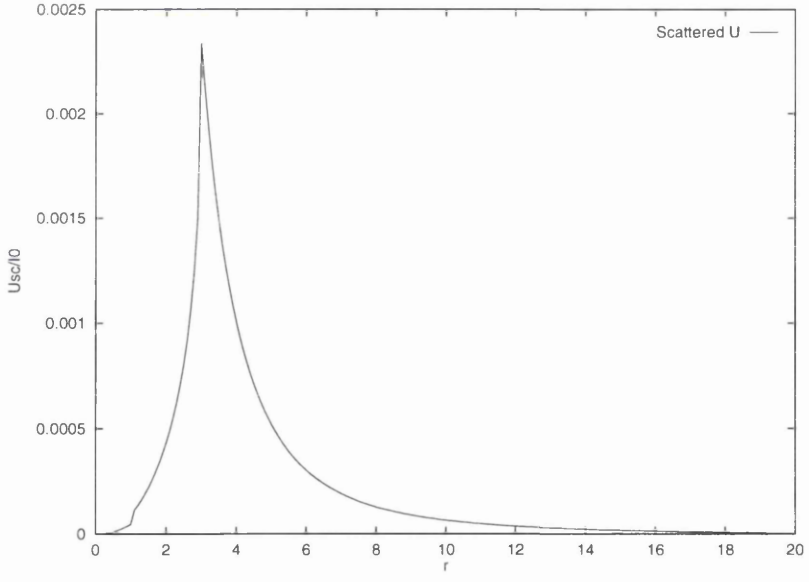

Figure 2.8: U_{sc} as a function of radial coordinate (in units of R_0) across the stellar disk. Here $R_h = 3R_0$. (Optical depth $\tau = 0.1$.)

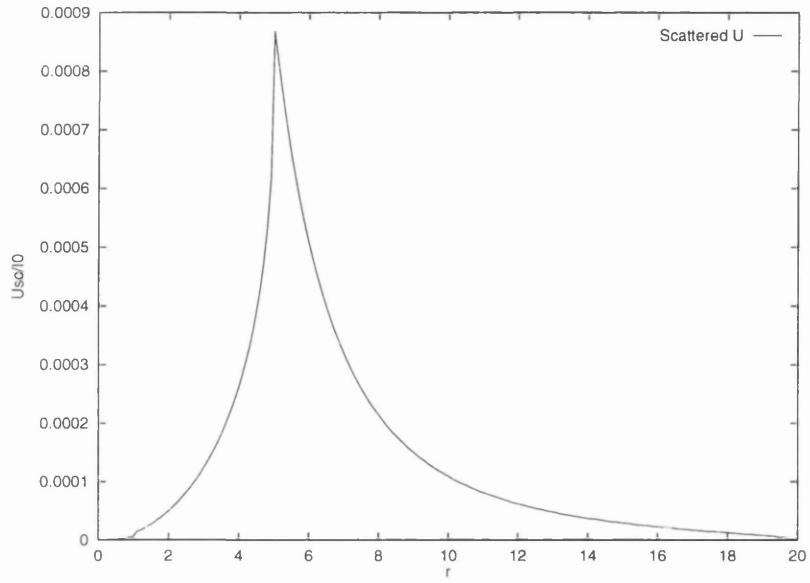

Figure 2.9: U_{sc} as a function of radial coordinate (in units of R_0) across the stellar disk. Here $R_h = 5R_0$. (Optical depth $\tau = 0.1$.)

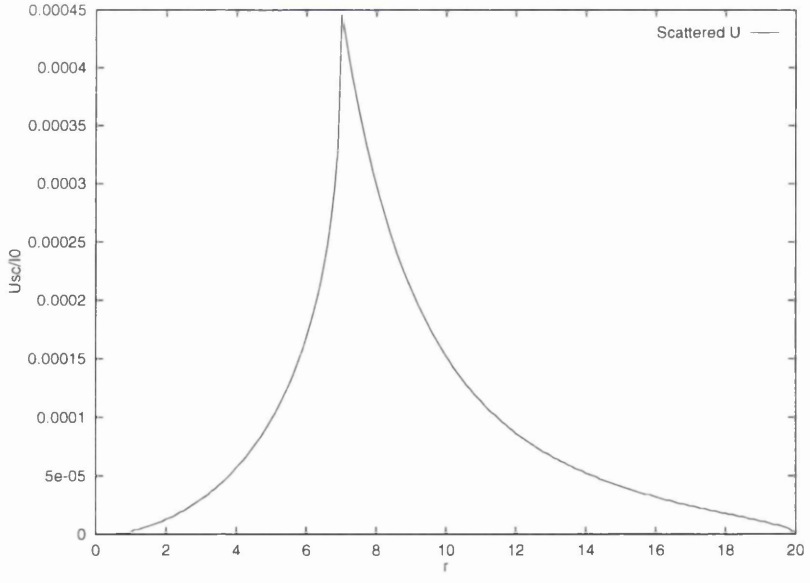

Figure 2.10: U_{sc} as a function of radial coordinate (in units of R_0) across the stellar disk. Here $R_h = 7R_0$. (Optical depth $\tau = 0.1$.)

U_{sc} is smaller than I_{sc}, by a factor ~ 2. However, it is much easier to detect this component of the scattered light as it is the only element of the stellar flux to be polarized. Fig. 2.11 shows the degree of polarization across the disk for the model considered in this section: at the edge of the envelope the light approaches 100% polarization as the scattering angle becomes closer to 90^o. In contrast, the unpolarized scattered light I_{sc} will be completely swamped by the much greater direct flux.

The upshot of all this is that polarimetry effectively picks the small flux from the envelope out of the much larger direct flux. Thus, polarization is a powerful probe of the envelope structure. This will become apparent in the next chapter, where we examine in detail the polarimetric signal produced when such a star is microlensed. For now, we can argue roughly as follows: if we integrate the microlensing amplification function (Eqn. (1.18)) over a disk of one Einstein radius , centred on the lens, we obtain a total amplification factor of $\sqrt{5}\pi$ (~ 7). If the Einstein radius $\sim 4R_0$, say, and it magnifies the main scattering region of the envelope where $I_{sc} \sim 0.002I_0$ (see e.g. Fig. 2.4), the amplification will be $\sim 20\%$: the degree of polarization in this region is ~ 0.5 (Fig. 2.11), giving a polarization signal $\sim 10\%$. Of course, this crude estimate does not take into account the magnification of the direct flux, which will dilute the polarization, but we can still reasonably expect a signal of $1 - 2\%$ polarization, which is easily measurable on a reasonably bright object. Furthermore, the optical depth of 0.1 is conservative, and a figure around three times this would be perfectly reasonable.

Finally, dust scattering in a red giant envelope is wavelength-dependent. We can see this in Figs 2.12 to 2.17, which show the scattered unpolarized and polarized intensities across the disk in the standard B and V wavebands. The central source is a black body with an effective temperature of 3500 K, and the units of intensity are such that $I_0 = 1$ in the B band. The scattering cross-section is proportional to λ^{-4}.

The unpolarized scattered light shows very definite chromaticity, with I_{sc} being relatively much more important at short wavelengths. As we shall see in the next chapter, this chromaticity can be amplified in a microlensing event, giving a characteristic chromatic

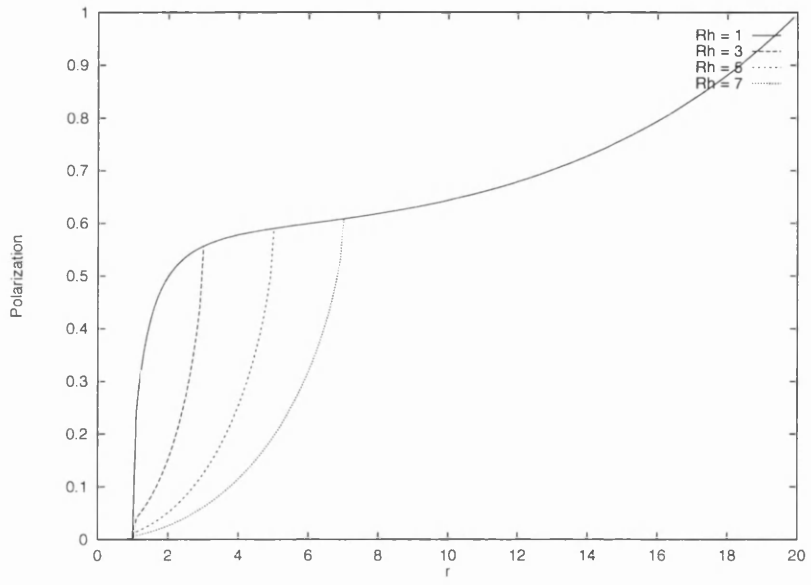

Figure 2.11: Degree of polarization as a function of radial coordinate (in units of R_0) across the stellar disk for $R_h = R_0$, $3R_0$, $5R_0$ and $7R_0$.

signal.

In contrast, the difference in polarized intensity in the two wavebands is very small. Nevertheless, this can also be detected by microlensing under favourable circumstances. One would also expect significant amplification of spectral lines associated with the envelope, analogous to the predictions in [47] - this, however, is beyond the scope of the present work.

None of these effects are restricted to giant stars: predicted polarimetric and chromatic effects have been published for the case where a main sequence star is lensed ([70]). The important difference here is that the scattering region where all the interesting effects occur is some distance ($\sim$ a few stellar radii) from the much brighter central source, rather than being confined to a narrow region about the limb. This means the lens can pick out this region without the signal being washed out by the amplified direct flux, and thus the observational prospects are greatly enhanced.

To summarise, we now have a model stellar envelope which allows us to calculate the Stokes parameters at any point on the disk. This model seems likely to produce significant ex-

tended source effects in microlensing simulations. In the next chapter, we shall investigate this possibility more fully, presenting a suite of predicted light curves and quantifying the observational prospects.

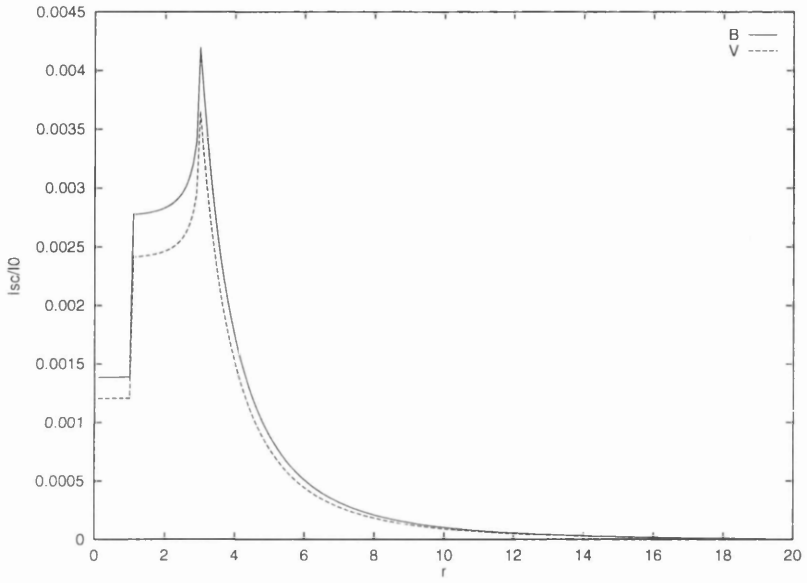

Figure 2.12: $I_{sc}(r)$ across the stellar disk in the B and V wavebands for a dust scattering envelope where $R_h = 3R_0$

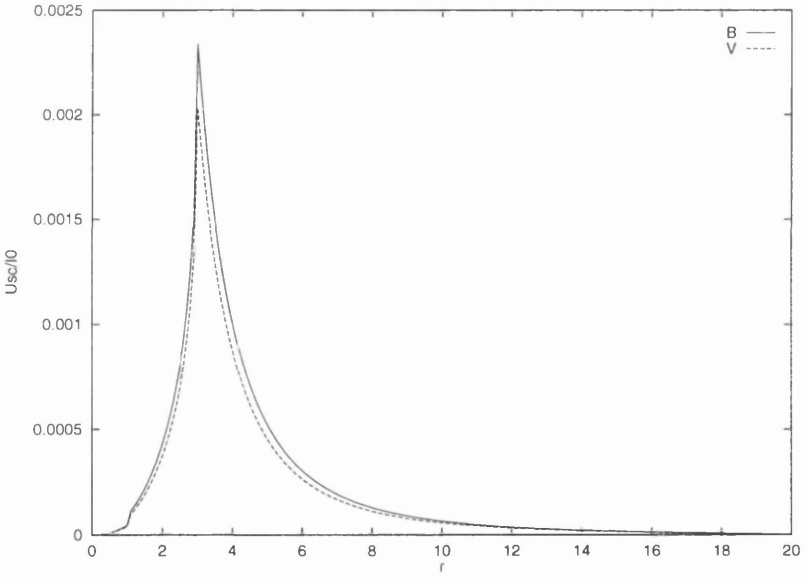

Figure 2.13: $U_{sc}(r)$ across the stellar disk in the B and V wavebands for a dust scattering envelope where $R_h = 3R_0$

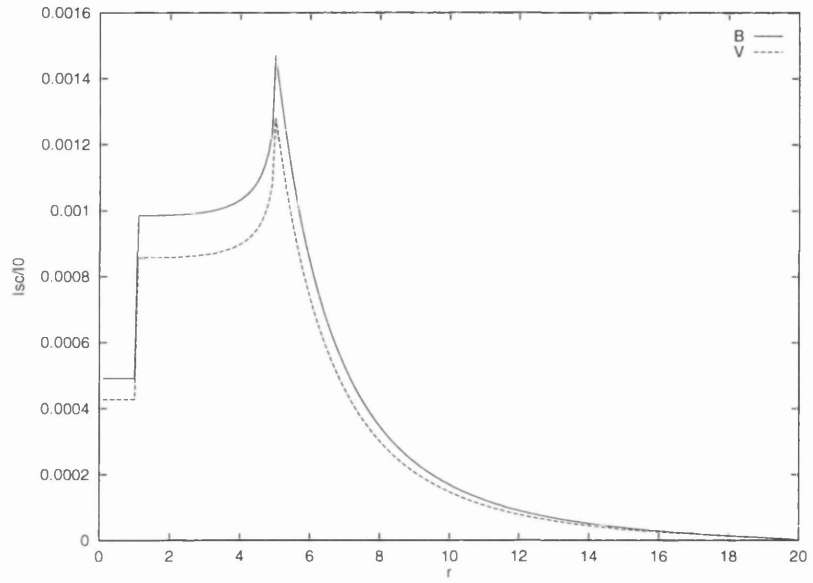

Figure 2.14: $I_{sc}(r)$ across the stellar disk in the B and V wavebands for a dust scattering envelope where $R_h = 5R_0$

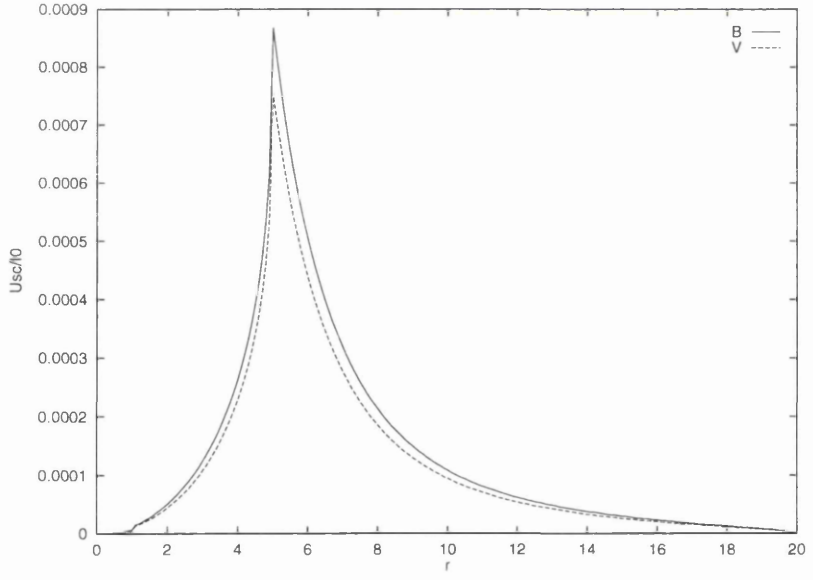

Figure 2.15: $U_{sc}(r)$ across the stellar disk in the B and V wavebands for a dust scattering envelope where $R_h = 5R_0$

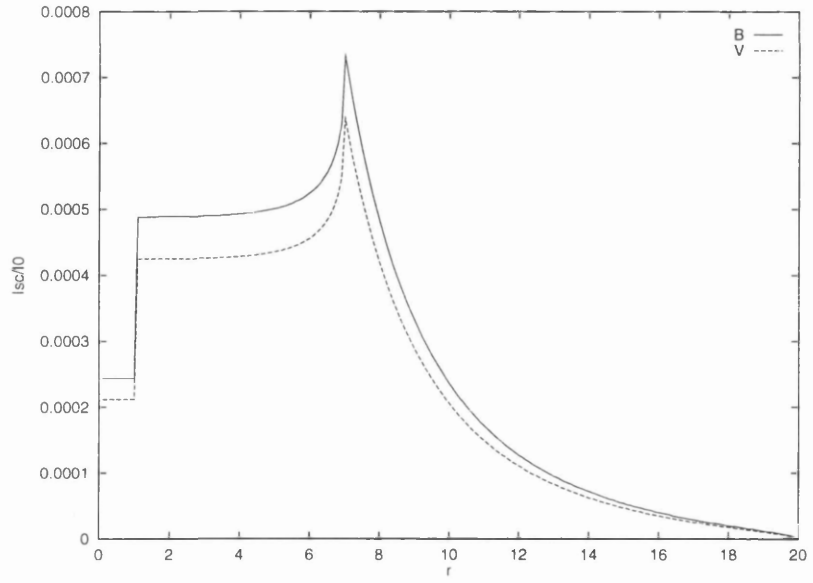

Figure 2.16: $I_{sc}(r)$ across the stellar disk in the B and V wavebands for a dust scattering envelope where $R_h = 7R_0$

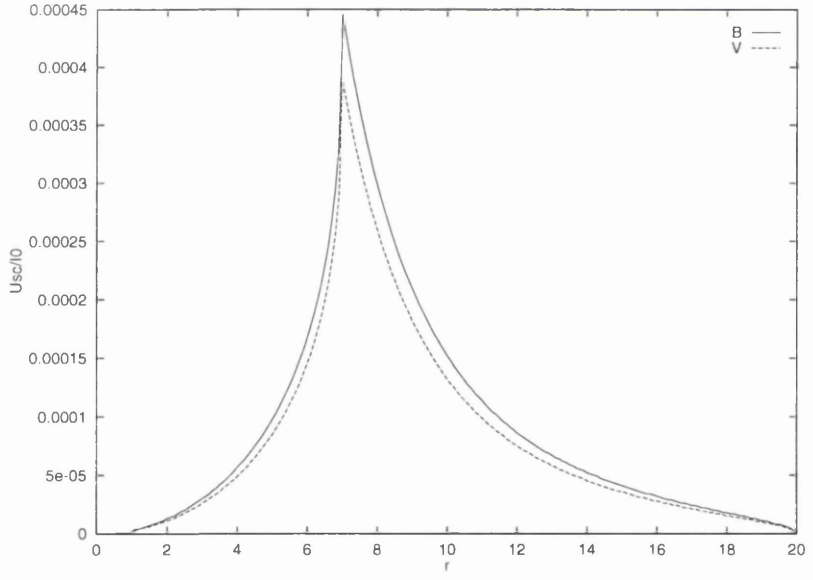

Figure 2.17: $U_{sc}(r)$ across the stellar disk in the B and V wavebands for a dust scattering envelope where $R_h = 7R_0$

Chapter 3

Microlensing light curves for extended envelopes

> Hofstadter's Law: It always takes longer than you expect, even when you take into account Hofstadter's Law.

In the previous chapter, we developed a simple model stellar envelope which can apply to a broad range of extended stars. We can now use this model as the source in microlensing simulations.

The basic approach is simple. For a given set of lens parameters, the observed flux during the lensing event is given by

$$F_I(t) = \frac{1}{4\pi R^2} \iint_{\text{disc}} I(r,\chi)\, A(r,\chi,t) r \,\mathrm{d}r \mathrm{d}\chi \tag{3.1}$$

where (r,χ) are polar coordinates on the stellar disk, R is the distance from the observer to the star, and $A(r,\chi,t)$ is the microlensing amplification function (see Eqn. (1.18)). The Stokes parameter I is the total intensity of radiation emitted at a point (r,χ) on the disk, as calculated in the previous chapter. The distance between the origin (at the centre of

the disk) and the projected position of the lens is a function of time t: evaluating this integral at a series of time steps gives us a microlensing light curve.

We can construct similar integrals for the polarized fluxes corresponding to the Q and U Stokes parameters, viz.

$$F_Q(t) = \frac{1}{4\pi R^2} \iint_{\text{disc}} Q(r,\chi)\, A(r,\chi,t) \cos 2\chi r \, dr d\chi \tag{3.2}$$

$$F_U(t) = \frac{1}{4\pi R^2} \iint_{\text{disc}} Q(r,\chi)\, A(r,\chi,t) \sin 2\chi r dr d\chi \tag{3.3}$$

Evaluating these in the same way as the total flux F_I, using the profiles from Chapter 2, allows us to calculate the degree P and direction ψ of polarization as a function of time, according to

$$P = \frac{\sqrt{F_Q^2 + F_U^2}}{F_I} \tag{3.4}$$

$$\psi = \frac{1}{2} \arctan \frac{F_U}{F_Q} \tag{3.5}$$

(see Appendix A for more details).

Throughout this chapter, the lensing object is always a point mass, Schwarzschild lens. Our focus will be on investigating whether extended stellar envelopes can produce appreciable polarimetric signals when lensed, how the light curves are affected by the structure of the envelope, and how best to exploit this information. Thus, the analysis breaks down into two main parts: variation of the lens parameters, and the lensing of a range of atmospheres.

In all the light curves, time is measured in units of the time the lens takes to cross one stellar radius $= R_*/v_\perp = D_d/D_s\xi_0\, t_{lens}$, where ξ_o is the projected Einstein radius measured in stellar radii, D_s and D_d are the source and lens distances, and t_{lens} is the lensing timescale as defined in Eqn. (1.19). The time when the lens is closest to the centre of the disk is defined as $t = 0$.

3.1 Lens parameters

The Schwarzschild lens is characterised by four parameters: mass, transverse velocity, distance from the source star and impact parameter (distance of closest approach to the source). We can reduce this to two, as the amplification function depends only on the projected Einstein radius in the source plane and the distance between the lens and the centre of the stellar disk.

In this section, results will be presented for $R_h = R_*$ and $R_h = 5R_*$, corresponding to an early type star and a red giant respectively. In all cases the density power law index $\beta = 2$.

3.1.1 Projected Einstein radius

As far as the unpolarized signal is concerned, increasing the Einstein radius of the lens simply boosts the amplification (Figs. 3.1 and 3.3). The polarized flux behaves somewhat differently. This signal depends on *differential* amplification across the disk: as the Einstein radius increases, the increased signal from the highly polarized envelope is offset to some extent by the fact that the high amplification now extends further across the source, amplifying the direct flux from the central photosphere. In Fig. 3.2, there is little difference between the $\xi_0 = 4R_*$ and $\xi_0 = 8R_*$ cases, as this law of diminishing returns comes into play. The red giant case (Fig. 3.4) is less affected by this problem, as the main scattering region is much further separated from the source star.

The double peaks seen in the polarization curves are similar to those presented in [70] for a lens transit across a stellar disk. The basic idea here is similar, except that "transit" here means the lens traverses the inner part of the disk where there is little scattering.

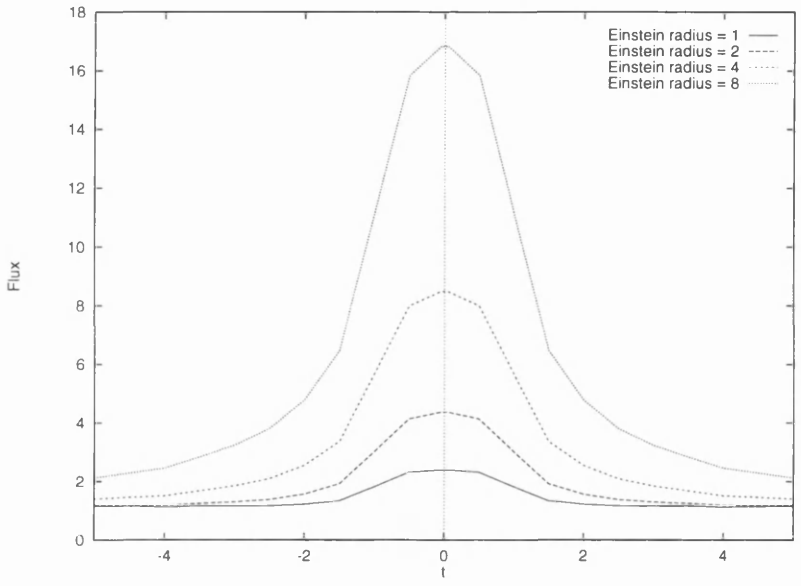

Figure 3.1: Unpolarized light curves for microlensing of a hot giant star. The unlensed flux = 1. Four cases are shown: Einstein radius = R_*, $2R_*$, $4R_*$ and $8R_*$. Optical depth $\tau = 0.1$, Impact parameter = 0.

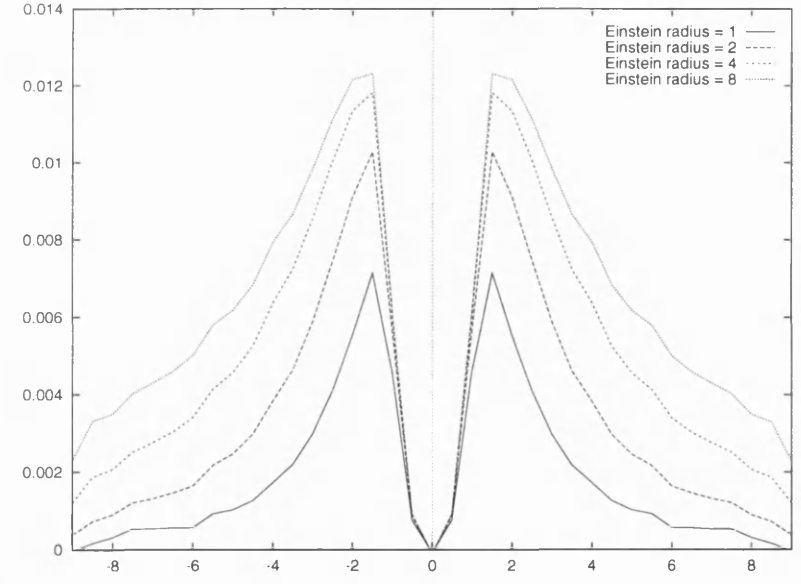

Figure 3.2: Polarized light curves for microlensing of a hot giant star. Four cases are shown: Einstein radius = R_*, $2R_*$, $4R_*$ and $8R_*$. Optical depth $\tau = 0.1$, Impact parameter = 0.

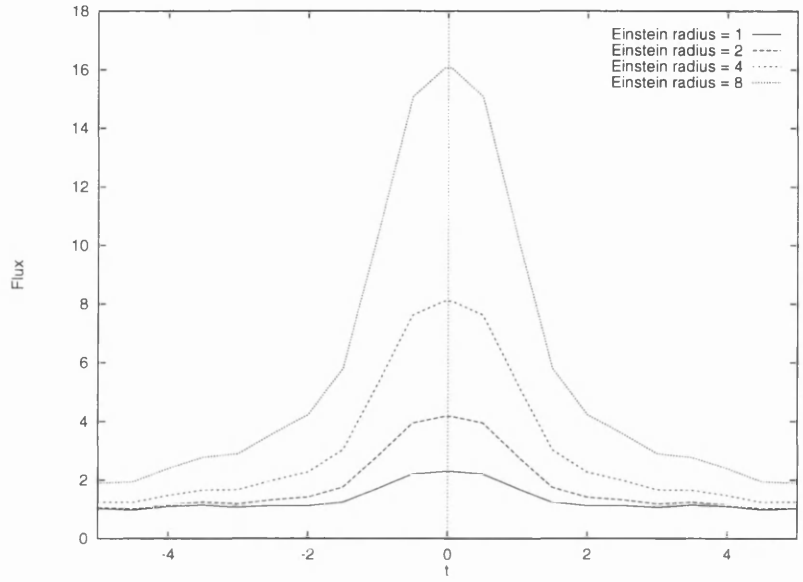

Figure 3.3: Unpolarized light curves for microlensing of a red giant star ($R_h = 5R_*$). The unlensed flux = 1. Four cases are shown: Einstein radius = R_*, $2R_*$, $4R_*$ and $8R_*$. Optical depth $\tau = 0.1$, Impact parameter = 0.

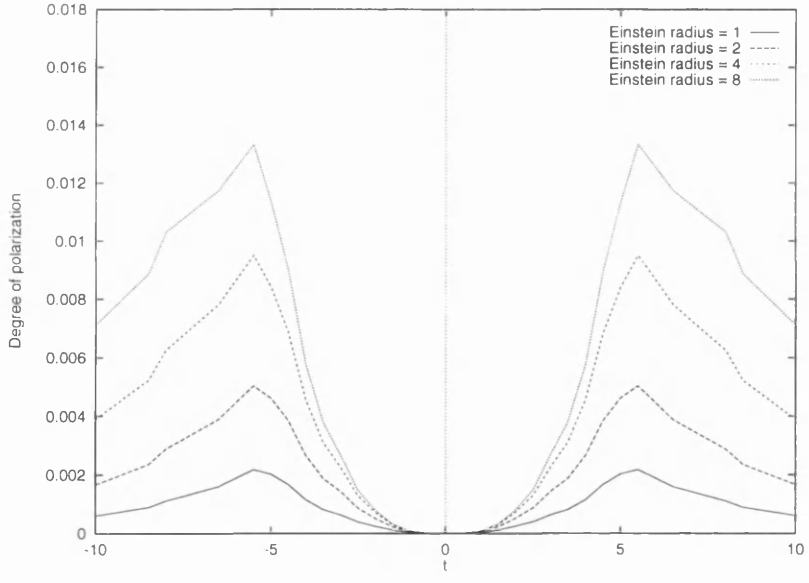

Figure 3.4: Polarized light curves for microlensing of a red giant star ($R_h = 5R_*$). Four cases are shown: Einstein radius = R_*, $2R_*$, $4R_*$ and $8R_*$. Optical depth $\tau = 0.1$, Impact parameter = 0.

3.1.2 Impact parameter

As the impact parameter increases, the unpolarized signal decreases markedly: when the impact parameter has reached $5R_*$, the amplification is small. None of this is very surprising.

The polarized light curves are more interesting. In the case of the hot, electron scattering envelope the signal still drops with increasing impact parameter, and the dip at $t = 0$ becomes less pronounced. This is because the bulk of the scattered light comes from regions close to the central photosphere. In contrast, the level of polarization from a lensed red giant is hardly affected by increasing the impact parameter. Here the scattering shell is far from the star, and provided the lens crosses this region at some point during the event the peak polarization will reach the same value. The main difference between the curves is that the section around $t = 0$ is much flatter when the lens is no longer transiting the inner part of the envelope. Consequently, we can expect a high degree of polarization when a red giant is lensed even when a large impact parameter leads to a low unpolarized amplification.

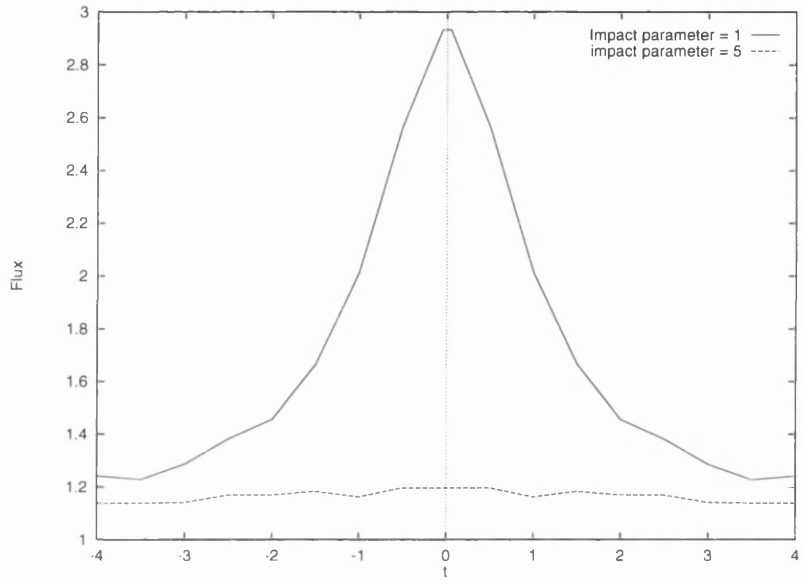

Figure 3.5: Unpolarized light curves for microlensing of a hot giant star. The unlensed flux = 1. Two cases are shown: Impact parameter = R_* and $5R_*$. Optical depth $\tau = 0.1$, Einstein radius = $2R_*$.

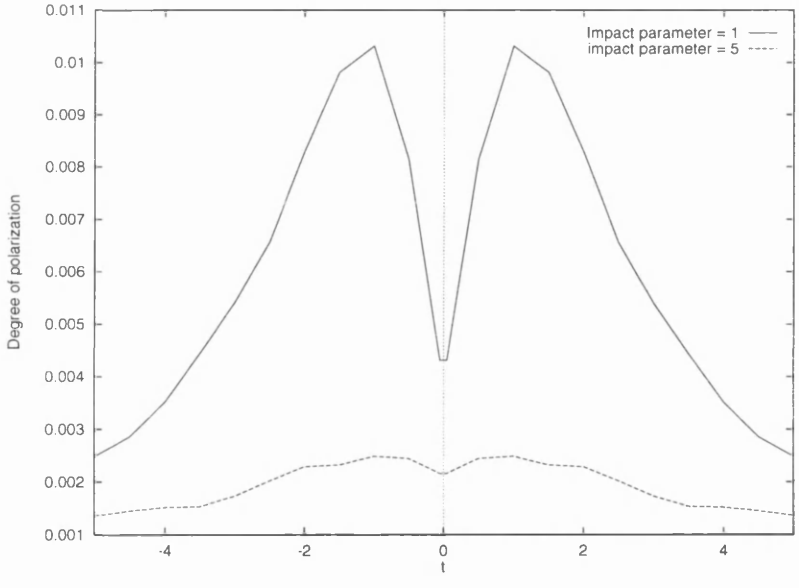

Figure 3.6: Polarized light curves for microlensing of a hot giant star. Two cases are shown: Impact parameter = R_* and $5R_*$. Optical depth $\tau = 0.1$, Einstein radius = $2R_*$.

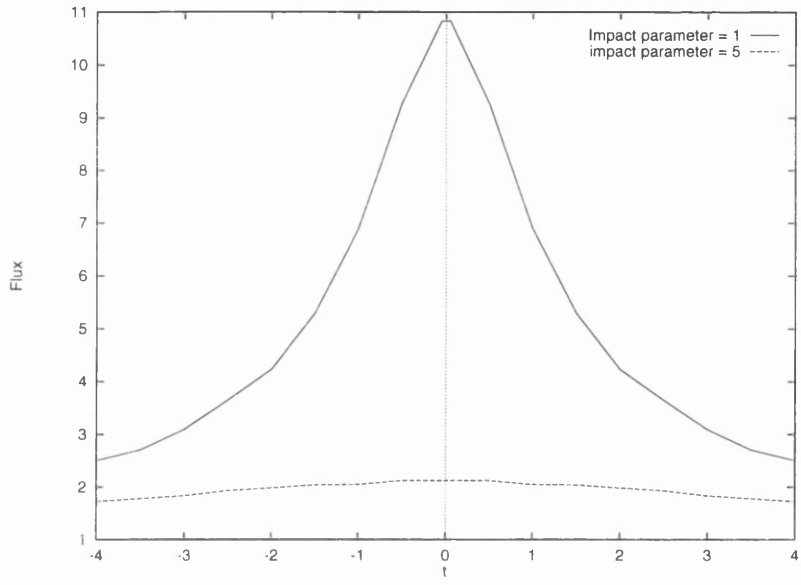

Figure 3.7: Unpolarized light curves for microlensing of a hot giant star. The unlensed flux = 1. Two cases are shown: Impact parameter = R_* and $5R_*$. Optical depth $\tau = 0.1$, Einstein radius = $8R_*$.

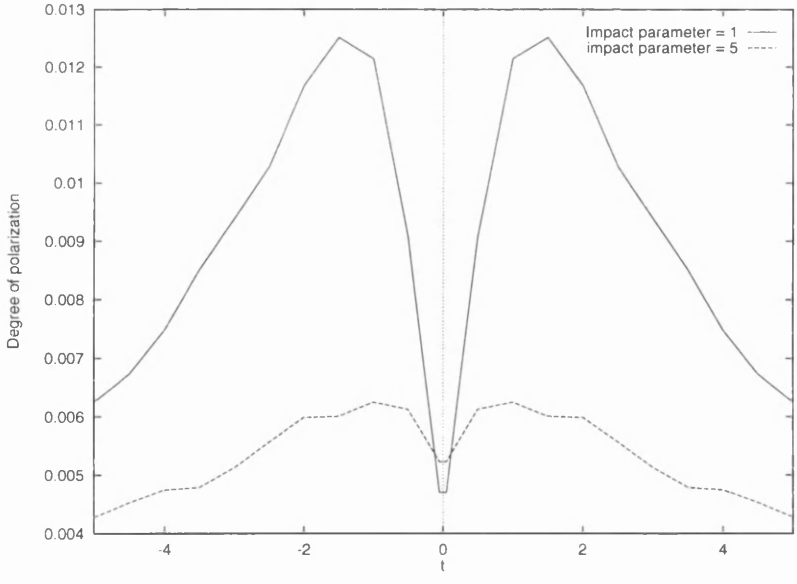

Figure 3.8: Polarized light curves for microlensing of a hot giant star. Two cases are shown: Impact parameter = R_* and $5R_*$. Optical depth $\tau = 0.1$, Einstein radius = $8R_*$.

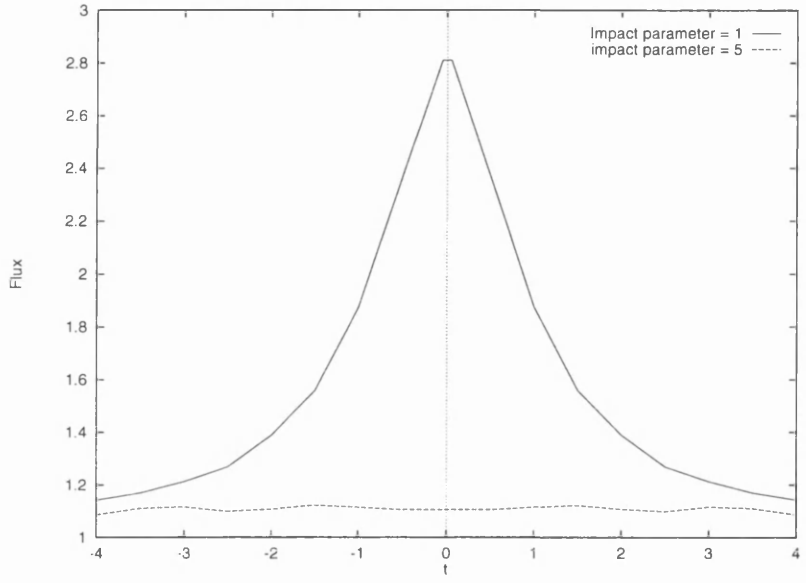

Figure 3.9: Unpolarized light curves for microlensing of a red giant star ($R_h = 5R_*$). The unlensed flux = 1. Two cases are shown: Impact parameter = R_* and $5R_*$. Optical depth $\tau = 0.1$, Einstein radius = $2R_*$.

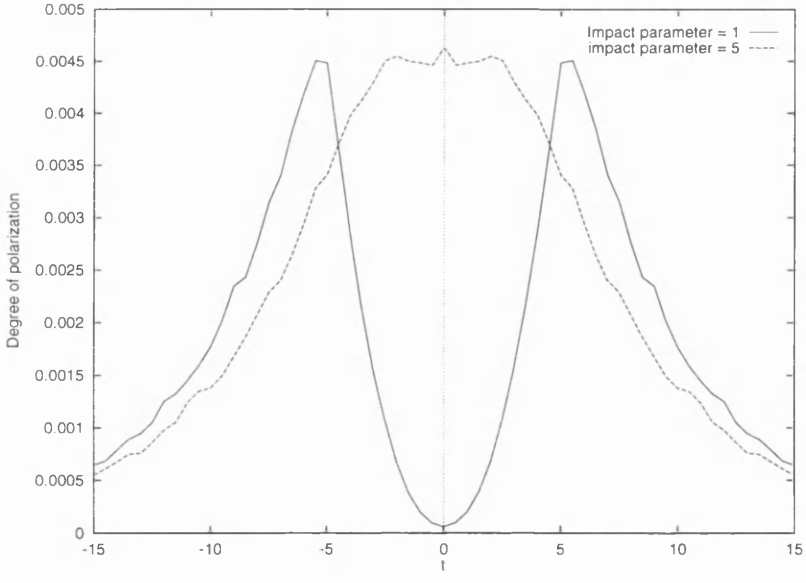

Figure 3.10: Polarized light curves for microlensing of a red giant star ($R_h = 5R_*$). Two cases are shown: Impact parameter = R_* and $5R_*$. Optical depth $\tau = 0.1$, Einstein radius = $2R_*$.

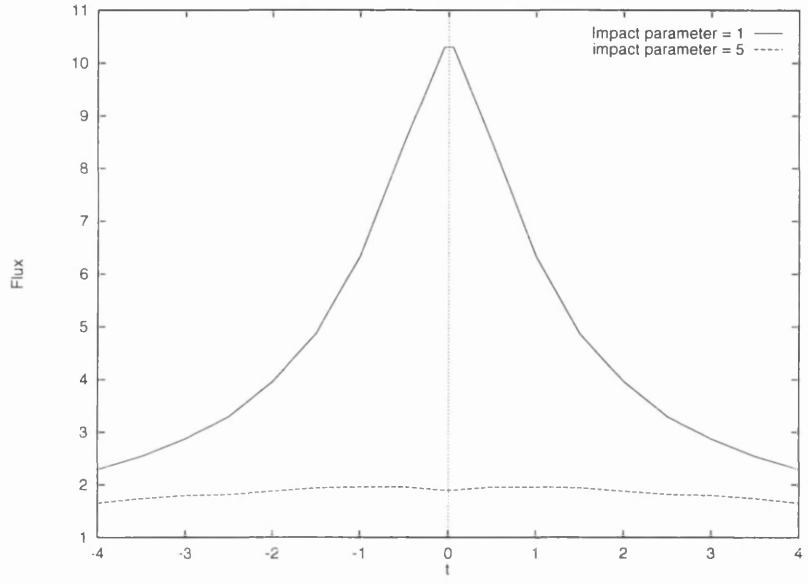

Figure 3.11: Unpolarized light curves for microlensing of a red giant star ($R_h = 5R_*$). The unlensed flux = 1. Two cases are shown: Impact parameter = R_* and $5R_*$. Optical depth $\tau = 0.1$, Einstein radius = $8R_*$.

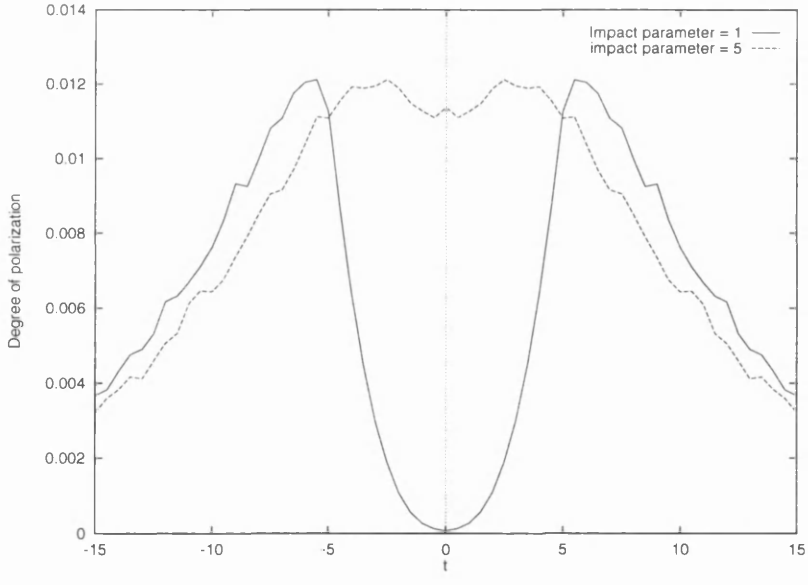

Figure 3.12: Polarized light curves for microlensing of a red giant star ($R_h = 5R_*$). Two cases are shown: Impact parameter = R_* and $5R_*$. Optical depth $\tau = 0.1$, Einstein radius = $8R_*$.

3.2 Envelope structure

Our simple model envelope can be specified with three parameters: the density power law index, the optical depth, and the extent of the region between the photosphere and the scattering envelope. Since the envelope is optically thin, the light curves simply scale with the optical depth, making this parameter profoundly uninteresting.

This section divides naturally between extended early type stars ($R_h = R_*$) and red giant stars ($R_h > R_*$).

3.2.1 Extended hot stars

Fig. 3.13 illustrates the effect of variations in the atmospheric density power law on the light curve. Increasing β steepens the polarimetric light curve, as the density of scatterers falls off more sharply with radial distance from the centre. The peak polarization also decreases slightly with β, presumably because the increased density close to the source of direct flux does not quite compensate for the decreased density in the outer reaches of the envelope, as the dilution by the direct flux is comparitively stronger.

In Be stars β is thought to vary between 2 and about 3.5 [54], so Fig. 3.13 covers the range of realistic cases.

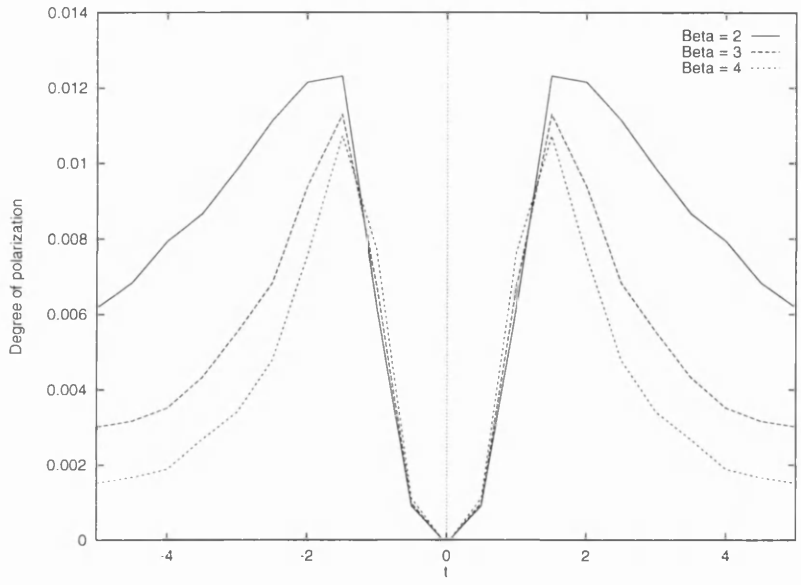

Figure 3.13: The effect of the density power law on the polarized light curves for microlensing of a hot giant star. Three cases are shown: density power law index $\beta = 2$, 3 and 4. Impact parameter = 0. Optical depth $\tau = 0.1$, Einstein radius = $8R_*$.

3.2.2 Red giant stars

In this case, varying the power law index has a steepening effect similar to that for the hot envelope (Fig. 3.14), though it is somewhat less pronounced. However, the fact that the dust forms far from the photosphere means the effect on the peak is the opposite to our previous case: concentrating the scatterers into a smaller region increases the polarization when that region is lensed.

If we change the dust formation radius (Fig. 3.15, we see that the position of the polarization peak very closely follows that change: so much so, in fact, that one can virtually read R_h directly from the light curve (assuming we know the impact parameter). Of course, if the impact parameter were sufficiently increased this would become less easy, but we can see here how a microlensing transit can practically image the stellar envelope. Chapter 6 shall deal with this issue in much more depth.

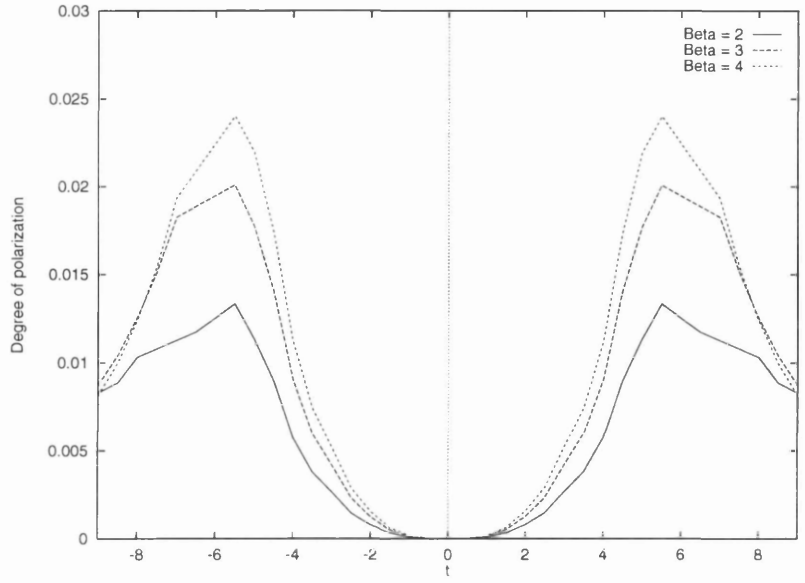

Figure 3.14: The effect of the density power law on the polarized light curves for microlensing of a red giant star ($R_h = 5R_*$). Three cases are shown: density power law index β = 2, 3 and 4. Impact parameter = 0. Optical depth $\tau = 0.1$, Einstein radius = $8R_*$.

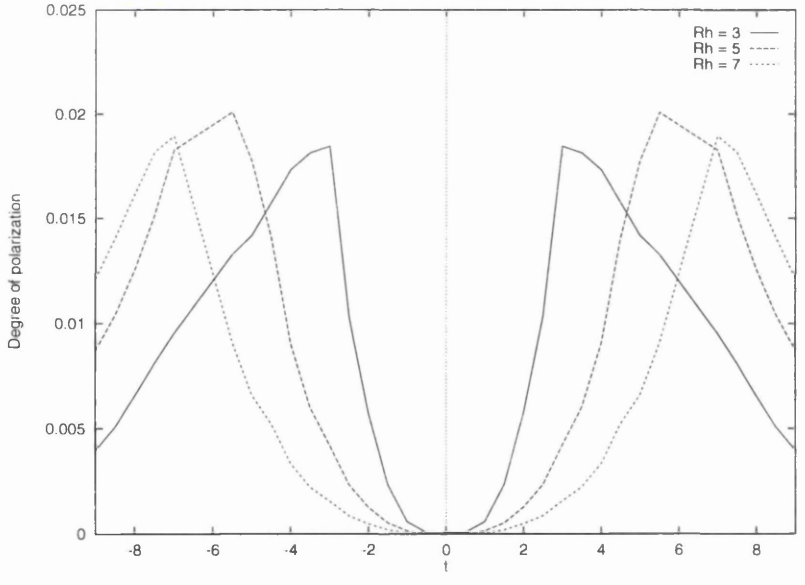

Figure 3.15: The effect of the dust forming radius on the polarized light curves for microlensing of a red giant star. Three cases are shown: $R_h = 3R_*$, $5R_*$ and $7R_*$. Impact parameter = 0. Optical depth $\tau = 0.1$, Einstein radius = $8R_*$.

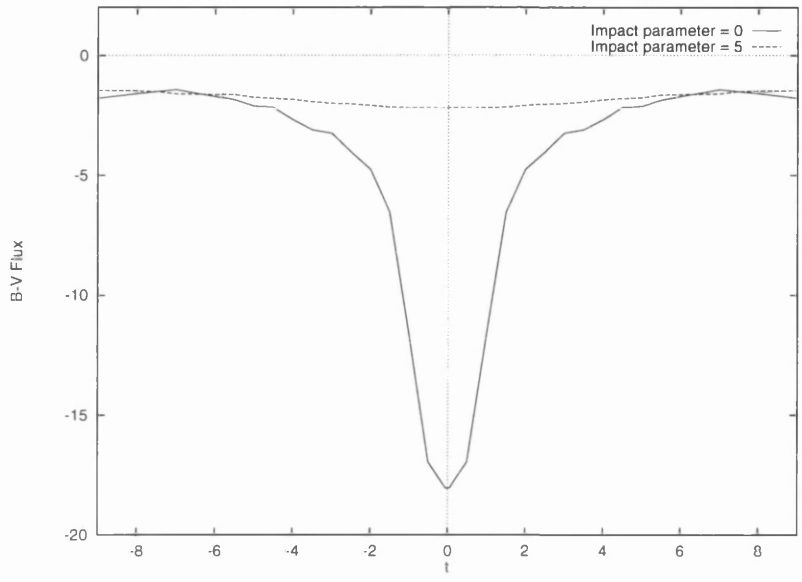

Figure 3.16: The difference between the unpolarized light curves in the B and V bands for a red giant stars with $R_h = 5R_*$. Impact parameter = 0 and $5R_*$. Optical depth $\tau = 0.1$, Einstein radius = $8R_*$.

3.3 Chromaticity

The cool dusty red giant envelope can be expected to show chromatic effects under microlensing, as the scattering is wavelength-dependent. Figs. 3.16, 3.17 and 3.18 illustrate this for a $T_{eff} = 3500K$ black body star whith an envelope whose scatterers have a λ^{-4} wavelength dependency. The difference between the signals in the standard B and V photometric bands is plotted against time.

The unpolarized flux is dominated by the central star. Only the polarized light curves are significantly affected by the scatterers. The dependence on the impact parameter and on R_h are qualitatively similar to the monochromatic cases, simply reflecting the distribution of dust across the disk. Quantitatively, the difference in polarization never gets much higher than 0.2% in the $\tau = 0.1$ atmosphere: even with a higher optical depth this difference would be barely on the bounds of detectability.

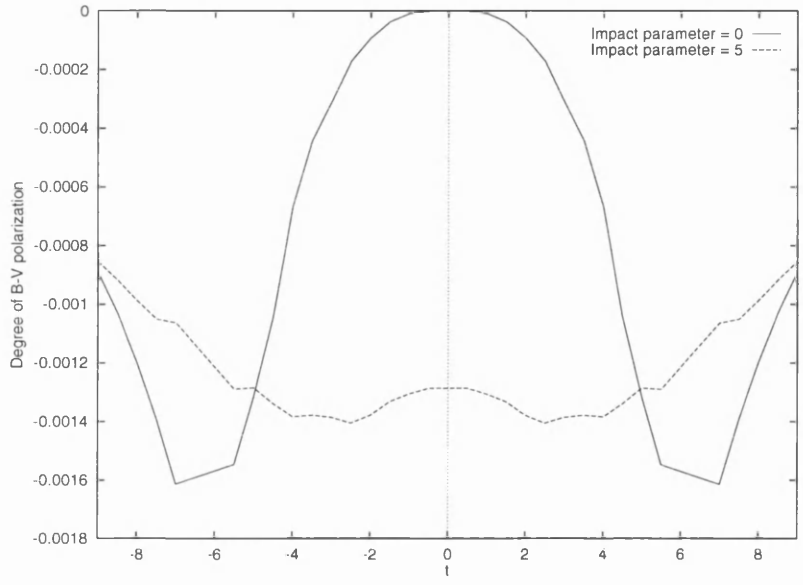

Figure 3.17: The difference between the polarized light curves in the B and V bands for a red giant stars with $R_h = 5R_*$. Impact parameter = 0 and $5R_*$. Optical depth $\tau = 0.1$, Einstein radius = $8R_*$.

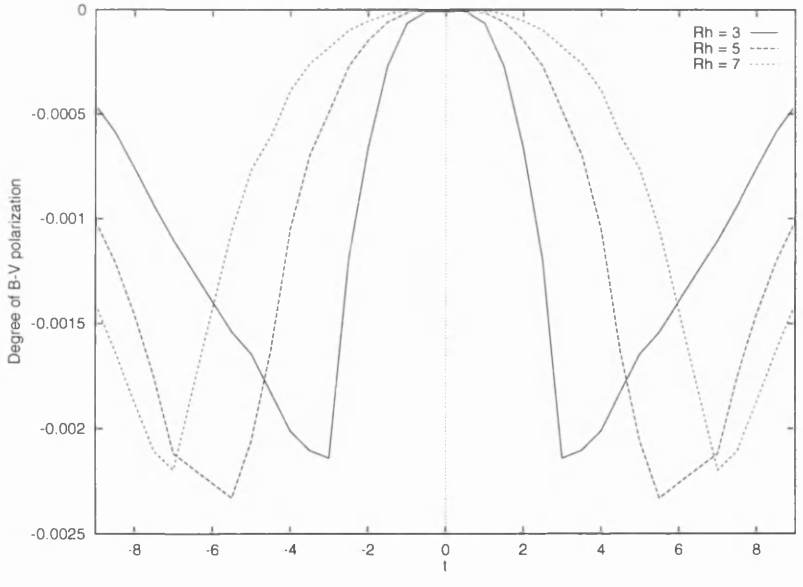

Figure 3.18: The difference between the polarized light curves in the B and V bands for red giant stars with $R_h = 3R_*$, $5R_*$ and $7R_*$. Impact parameter = 0. Optical depth $\tau = 0.1$, Einstein radius = $8R_*$.

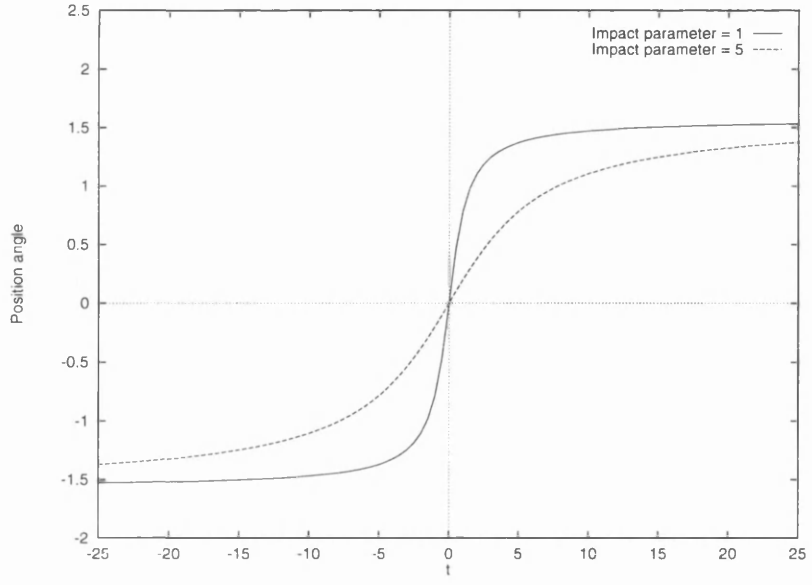

Figure 3.19: The effect of the impact parameter b upon the direction of polarization. Two cases are shown: $b = R_*$ and $b = 5R_*$.

3.4 The direction of polarization

For every event, the behaviour of the position angle of polarization is exactly the same. The rotation of the polarization direction is independent of the details of the atmosphere, and only depends on the impact parameter b. This is a purely geometric effect, and applies to any atmosphere in which the scattered light is polarized at right angles to the direction of the incident ray: if ϕ is the position angle,

$$\tan \phi = \frac{v_\perp t}{b}, \tag{3.6}$$

where b is the impact parameter.

This is significant, not only because it gives a clean determination of the impact parameter, but also because the position angle can be measured much more easily than the degree of polarization [56]. Thus, even when the polarization signal is too small to tell us much about the stellar atmosphere directly, it can still be invaluable in constraining the lens parameters.

3.5 Non-spherical envelopes

We can extend this analysis to the case of a non-spherical, optically thick stellar envelope. The polarimetric signal is of a similar size to the spherical case, but some new and interesting phenomena appear when spherical symmetry is broken.

Figs. 3.20 to 3.25 show the results of a Monte-Carlo simulation, carried out by Jon E. Bjorkman, of lensing a star with an optically thick, disk-shaped envelope ($n = n_0(a + sin^m\theta)r^{-3}$). Because this object is axisymmetric, it has an intrinsic unlensed polarization. which depends on the angle of inclination i.

In general, the flux profile is symmetric, but the polarization profile is markedly asymmetric. This is because the polarized flux is emitted from the (axisymmetric) envelope, while the unpolarized flux mainly comes directly from the central star. There is potentially a great deal of information contained in the polarimetric profile: the shape of the polarized and unpolarized light curves can tell us about its density structure, and the rotation of the polarization angle indicates the thickness of the disk. Thus, the polarized and unpolarized flux are powerful diagnostics of the structure and form of the disk.

A similar model could apply to quasars, which are the other important microlensing candidate, although in that case the signal is more likely to be complicated by multiple microlensing. The amplification function in such a case becomes much more complicated, with extended cusp structures, making the calculations much more intensive and the interpretation of the light curve more ambiguous

Confining ourselves to the stellar case, there are of course many more possible sources of polarization and chromaticity in a stellar atmosphere. Starspots, for example, would give rise to narrow but potentially significant features in the light curves, and we have not even touched on spectroscopy (which is the ultimate extension of the work on chromaticity). One particularly interesting case is jets from a star or quasar. These could give a unique double signal, as the lens passes separately over the disk and over the jet, with the two peaks polarized at right angles to each other. It should be apparent by now that this

is a very fertile area, with scope for building up more and more complex features onto the source model and seeing how they feed through into the light curves. The general principles remain the same as in this chapter, however: the closer the feature is to the lens position, and the further away from the main source of direct flux, the more distinguishable and informative the signal.

3.6 Polarisation as a microlensing diagnostic

One of the main problems - possibly *the* main problem - in microlensing is determining whether some brightness variation is due to lensing rather than some intrinsic variability in the source itself. A number of criteria may be (and have been) adopted in order to make this distinction, but none of them are perfect.

1. *Symmetry:* This is actually the most reliable criterion. Figs. 3.20 to 3.22 show that even when the envelope is asymmetric, the (unpolarized) light curve will be symmetrical. Thus, demanding symmetry is unlikely to result in dismissing genuine microlensing events. On the other hand, it is a somewhat weak condition, and cannot be relied upon to discriminate microlensing events from other forms of variability.

2. *Achromaticity:* For a point source this criterion must hold true, but any variations in colour across an extended source will manifest themselves in a microlensing event due to differential amplification across the source. This thesis is only concerned with extended sources, so for our purposes any interesting event is likely to be excluded by a strict achromaticity condition. Fortunately, the MACHO group have stopped demanding achromaticity in their candidate events.

3. *Uniqueness:* This demand generally leads to variable stars being dismissed as sources for microlensing. However, as we shall see, it is possible to be a little more subtle.

If we combine polarimetric measurements with our photometric light curve we have a new and powerful way to distinguish microlensing events from other types of variability.

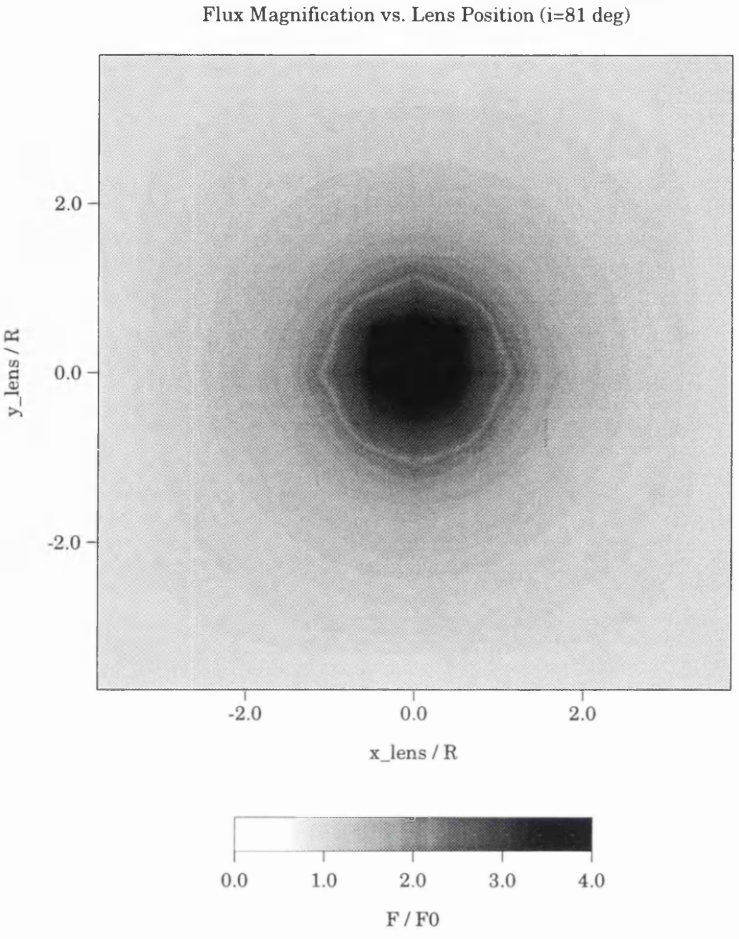

Figure 3.20: Unpolarized signal from an axisymmetric disk, inclined at 81° from the line of sight (i.e. almost edge-on).

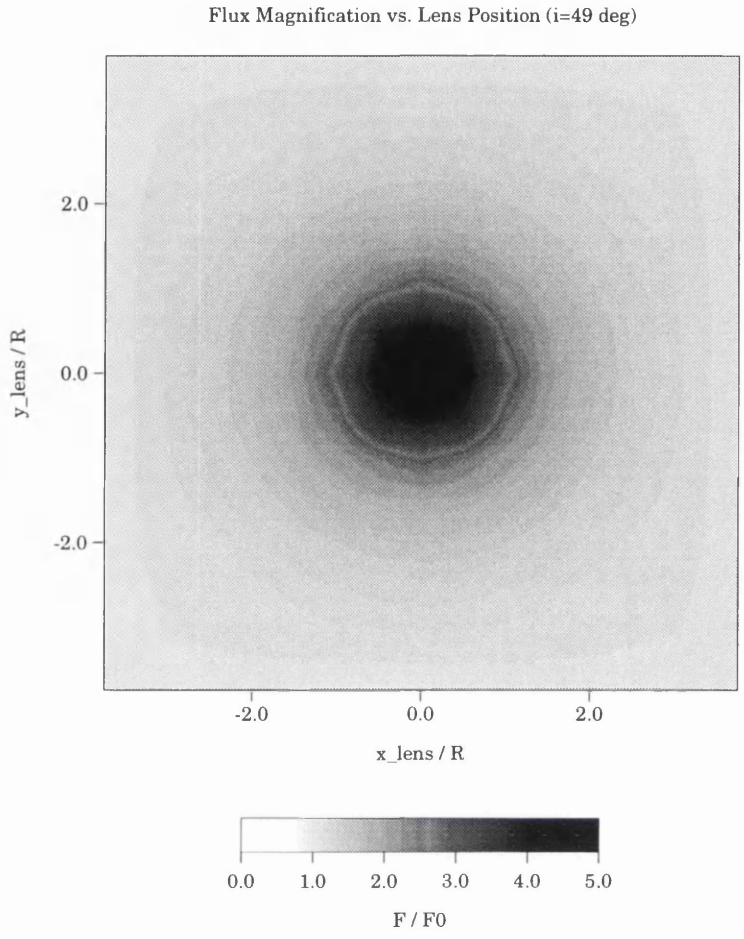

Figure 3.21: Unpolarized signal from an axisymmetric disk, inclined at 49° from the line of sight.

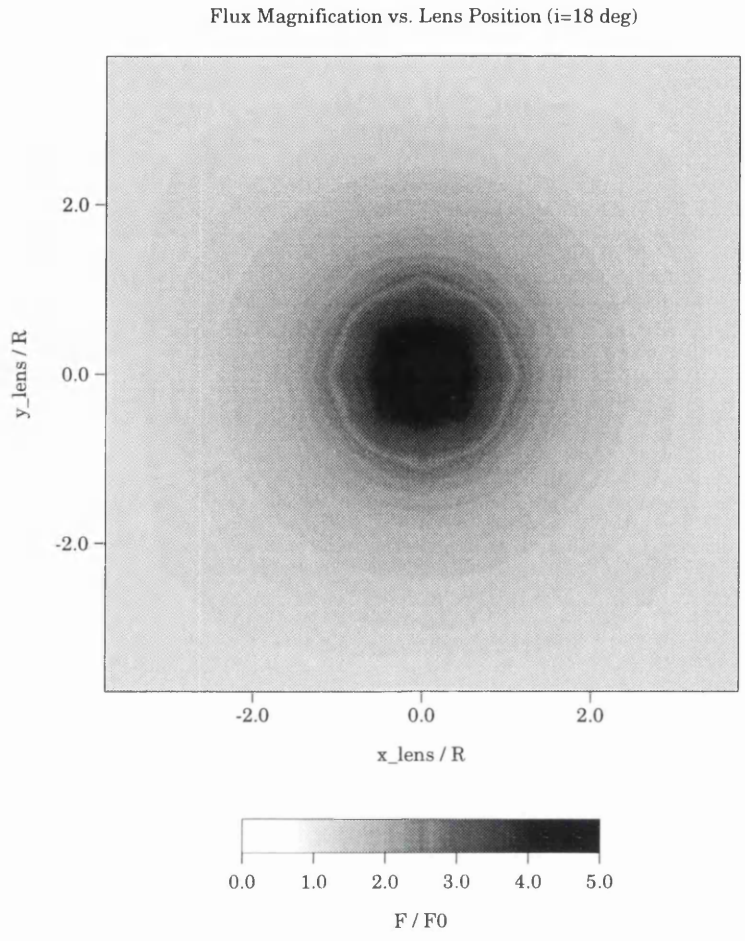

Figure 3.22: Unpolarized signal from an axisymmetric disk, inclined at 18° from the line of sight (i.e. almost face-on).

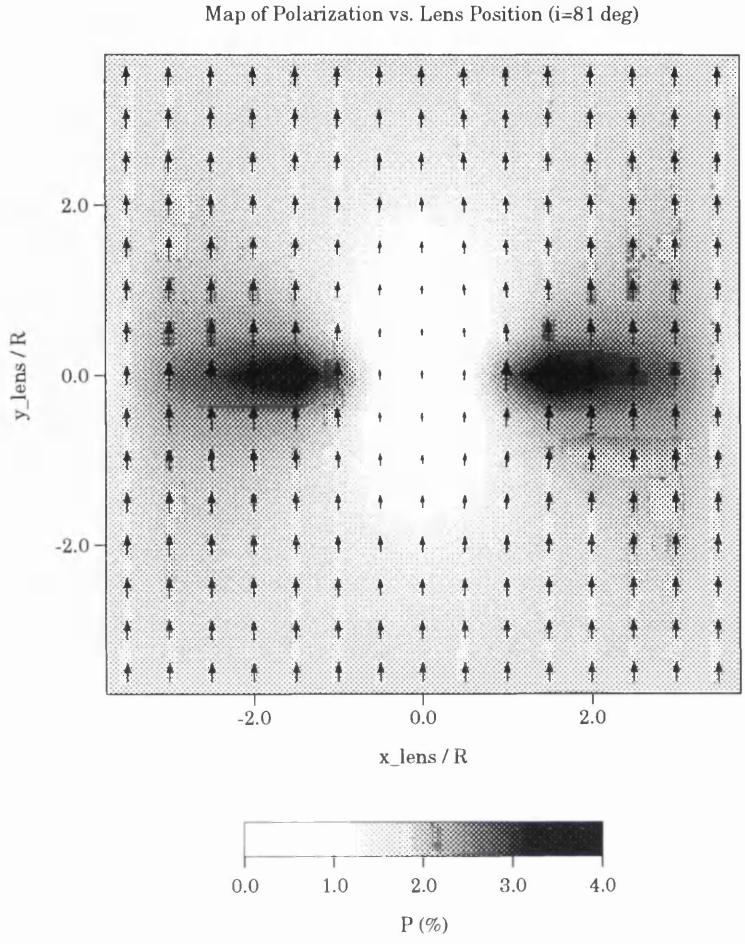

Figure 3.23: Polarized signal from an axisymmetric disk, inclined at 81° from the line of sight (i.e. almost edge-on).

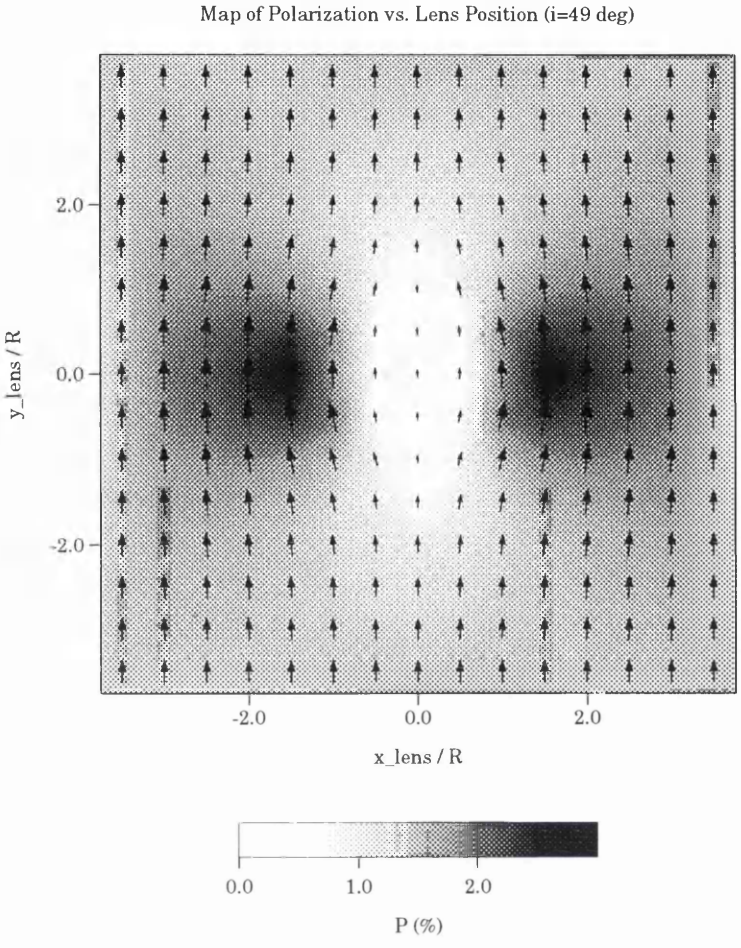

Figure 3.24: Polarized signal from an axisymmetric disk, inclined at 49° from the line of sight.

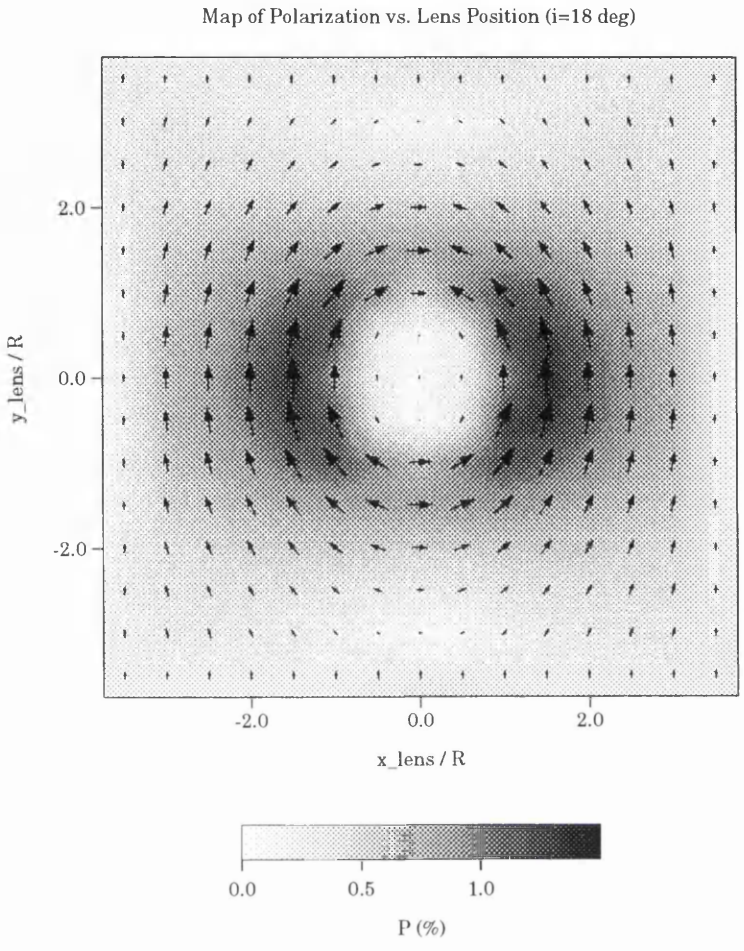

Figure 3.25: Polarized signal from an axisymmetric disk, inclined at 18° from the line of sight (i.e. almost face-on).

The polarization signatures obtained in this chapter are quite unique to microlensing, and should be able to pick out microlensing candidates even in a variable star. Any star whose variability is due to primarily radial pulsations will show little or no polarimetric variability, and even in stars with some degree of variable polarization the characteristics of this variation are quite different. For example, the peak polarization in luminous late-type variables coincides with the *minimum* unpolarized flux [52].

The other main point of this section is that polarization can be an effective probe of the stellar envelope. It is not too difficult to see why. Virtually all the unpolarized light comes from the central star, so the photometric light curve contains essentially no information about the envelope. In contrast, all the polarized intensity is emitted from the extended envelope. This means that polarimetric measurements quite naturally see only this part of the star.

Microlensing can make some unique contributions here. It allows essentially *model - independent* estimation of important stellar parameters, such as the density profile in the envelope and (in red giant stars) the extent of the ionized region within the dust-forming shell. Of course, it is not the only possible method, but its ability to probe the atmosphere directly makes it very powerful. For example, in Be stars the azimuthal density distribution in the envelope is poorly understood, and difficult to determine by "traditional" methods [57]. A glance at Figs. 3.23 to 3.25 shows that the width of the polarimetric microlensing light curve gives a direct indication of this otherwise inaccessible parameter.

It is worth mentioning the direction of polarization separately. As was seen in section 3.4, the behaviour of this angle gives the impact parameter directly (in a spherically symmetric system). Independent knowledge of this value is extremely useful, not only in determining lens parameters but also when inverting the light curve (see chapter 6). Even in the non-spherical case, the polarization direction can tell us about the impact parameter and the inclination of the disk: here, however, the situation is not quite so clear-cut.

3.7 Observational prospects

Unfortunately, microlensing of a given star is an unpredictable, one-off event. If the results of this chapter are to have any practical consequences, there must be a reasonable probability that at least a few events will involve a giant star being lensed, and that the parameters will be such that the extended source effects can be detected. Current microlensing surveys are already able to distinguish the effects of an extended source on the photometric light curve [58], but the polarimetric signal is much fainter. Can we hope to detect it?

Let's start by setting a detectability threshold. Giant stars in the microlensing surveys have apparent magnitudes $m_V \sim 17$ in the Galactic Bulge, and $m_V \sim 19$ in the LMC [33]. If we assume that photon shot noise dominates the polarimetric errors, and consider a 1 hour integration time on a 1m telescope, the polarimetric accuracy achievable is $\pm 0.2\%$ for a bulge giant, and $\pm 0.6\%$ for a giant in the LMC [59]. Requiring the polarimetric signal to be greater than the noise sets our threshold for a detectable polarization signal.

Next, we need some idea of the event rate. Recall the microlensing optical depth, τ, introduced in Eqn. (1.20). The MACHO collaboration has measured the optical depth for microlensing of giant stars in the Bulge, obtaining $\tau = 3.9^{+1.8}_{-1.2} \times 10^{-7}$ based on 13 events [32]. No separate estimate of τ for giants has been published for the LMC, but Monte-Carlo simulations predict $\sim 10\%$ of all LMC microlensing events will involve giant stars [31].

Consider the LMC. The most probable MACHO mass is $\sim 0.5 M_\odot$: if the object is half-way between Earth and the LMC, the projected Einstein radius $\xi_0 \sim 3 \times 10^3 R_\odot$, or about $8 R_*$ for the models discussed in this chapter. If such an object lenses an LMC star, the event will be considered as a microlensing candidate if the amplification is greater than 1.34. Neglecting the small contribution of the unpolarized scattered flux, we can see from [70] that the impact parameter must be $\lesssim 10 R_*$ for the amplification to reach that level.

Fig. 3.26 shows the polarized light curve for a red giant source in this marginal case.

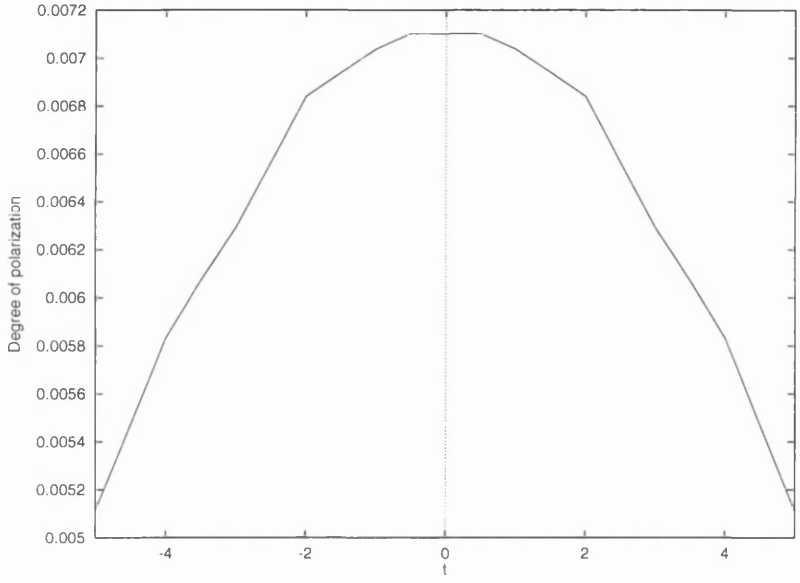

Figure 3.26: The polarized light curve for an LMC red giant ($R_h = 5R_*$) whose unpolarized microlensing signature is on the threshold of detectability. Optical depth $\tau = 0.1$, Einstein radius $= 8R_*$.

The peak polarization is just over 0.7%, which exceeds the detectability threshold for polarization. Given that the optical depth here is a very conservative 0.1, and that the polarization could therefore easily be 3 or 4 times this large, we conclude that *every* LMC microlensing event with a red giant source has a measurable polarization signature. Thus the prospects for polarimetric follow-up observations of LMC microlensing alerts are excellent: since the typical timescale of these events is $\sim$ 37 days [31], a substantial part of the light curve could realistically be observed in this way.

The prospects for the Bulge are not so easy to analyse, as estimates of the mass of lensing objects in that direction are not yet forthcoming. However, since we can expect to be able to measure signals as low as 0.2% polarization, every light curve presented in this chapter is observable, including the chromatic effects. As a rough guide, for a given lens mass, and assuming the lens is half-way between Earth and the Bulge, the projected Einstein radius is approximately $\sqrt{5}$ times smaller than in the LMC case, or just less than half as large. If the mass distribution of lenses is similar to that toward the LMC, we can again expect

all red giant lensing events to display clearly observable polarization. On the other hand, if the lenses are much smaller towards the bulge, hot stars such as Be stars become more likely to show polarimetric variability. For example, $M_{lens} = 0.001 M_{\odot}$ yields a projected Einstein radius of $28 R_{\odot}$ towards the Bulge, which is $\sim$ a few R_{*} for a Be star ([54], [60]).

We have so far entirely ignored the effects of interstellar polarization on the signal. This is justified to some extent. We are interested in variable polarization: provided the interstellar polarization towards the lensed star is does not change on these timescales, it can in principle be measured after the event and subtracted from the data. In practice, this will increase the errors on the polarization measurements, and a small variable polarization may be swamped by the interstellar component. However, for reasonably large polarimetric signals we may assume that the microlensing and interstellar polarizations can be disentangled.

In conclusion, then, microlensing can produce interesting and informative polarimetric signals from extended stellar envelopes. These signals are readily measurable in the fields of existing microlensing surveys, and the necessary polarimetric follow-up observations are eminently practicable. Given the great statistical difficulties involved in interpreting the current, limited microlensing data, such observations can and should be made as a matter of course.

We now leave envelope modelling, though one could certainly continue adding features to the relatively simple models developed here, and investigate a related aspect of microlensing. Can we exploit microlensing to image stellar atmospheres directly, without any underlying model? To answer this question, we must first go into the theory of inverse problems, to which the next chapter is devoted.

Chapter 4

Inverse problem theory

> "This obsession with the specific activity of quantified functions is what science shares with pornography."
>
> Dr. Nathan, *The Atrocity Exhibition*, (J. G. Ballard)

Inverse problems are an inevitable feature of remote sensing. Loosely speaking, any observational data is the result of some mechanism (an instrumental response, say, or a propagation function) processing the information you want into a far less useful form. Inverting this data to find the original source is a little like trying to determine the breeding behaviour of the hedgehog from a random sample of roadkill.

The numerical and mathematical properties of inverse problems have been studied most extensively in the context of geophysics, but they arise in many other fields. Indeed, astronomy has been called the ultimate inverse problem [61], since the physical processes are uncontrollable and *in situ* measurements impossible.

An understanding of the theory and practice of inverse problems would therefore seem essential in astronomy. However, with a few notable exceptions ([62], [63]), few astronomers have appreciated this. Instead, they have generally preferred their traditional weapons of forward modelling and parameter fitting. In this chapter we outline the need for a more

sophisticated approach, and discusses the particular strategy which will be used later in this thesis.

4.1 Ill-posedness and ill-conditioning: the problem with inverse problems

Whenever we measure anything in science, we do so in the hope of using the results to find out about some feature of a physical system. To put this in rather more formal terms, we want to find a solution $f \in F$ given a data set $g \in G$. One can classify such problems into two categories, well-posed and ill-posed, based on their mathematical properties [64], [65]. A well-posed problem is one which satisfies the following criteria:

1. There exists a solution $f \in F$ for every $g \in G$.
2. The solution is unique.
3. The solution f depends continuously on g, that is the solution is stable to small perturbations in the data.

If one or more of these conditions is not satisfied, the problem is ill-posed.

Let us write the relationship between the data and the source function as

$$Kf = g \tag{4.1}$$

where K is an integral operator. Unless K is a delta function, it will in general have a smoothing effect. As a consequence, an arbitrarily large localized variation in f can produce an arbitrarily small variation in g. Hence the problem is ill-posed.

As a more concrete example, introduce a perturbation $\delta f = A_0 \sin(\omega y)$, where A_0 is an arbitrary constant. Clearly the corresponding perturbation in the data, δg, can be made arbitrarily small by considering sufficiently large values of ω (for a continuous kernel

$k(x, y)$). In effect, the kernel smooths out the high frequency contributions to the source function. Of course, this also works the other way: small perturbations to g can result in arbitrarily large perturbations to f.

One can think of the operator K as mapping a large region of the source function space F into a small region of the data space G. The dangers of the forward-fitting approach are then clear. Simply because a given source model f fits the data g closely is no guarantee that it is in any way a good approximation of the true source function.

4.2 Hypotheses and data

So what does all this mean in practice? Well, in the first instance we see that forward modelling can lead to a rather blinkered approach. Any model will give some kind of best fit to the data, and if this fit seems close enough the model will generally be accepted even if the physical ideas behind it are wrong. In a strictly falsificationist approach this is perfectly sound: the hypothesis has not been ruled out by the data. However the philosophical niceties are often overlooked in the squalid trench warfare of data analysis, and an attractive curve can distract attention from the fact that whole classes of solution have been rejected *a priori*. We have only allowed the data to answer a specific, limited question, rather than listening to what it is really trying to say.

So why not work directly back from the data, and explore all the solutions it allows? Well, there are serious difficulties here too. The source function is essentially a derivative of the data. Differentiating such discontinuously varying data gives a wildly oscillating solution: thus, the naïve solution of Eqn. (4.1) is highly unstable and yields little useful data.

The most obvious way of dealing with these problems is not to differentiate the data itself, but to draw a continuous curve through the data points and then invert this curve. This is a (poor) form of *regularisation*: the data has been smoothed in order to stabilise the inversion. While such an approach will work, in the sense of giving a stable, well-behaved answer, there is a nasty sting in the tail. This kind of smoothing is a subjective process -

real features in the data may be lost, making the whole exercise seem somewhat pointless.

It is therefore necessary to take a far more rigourous approach to the whole issue. In doing so, we shall see that regularised inversion can enable us to extract the meaningful information from the data without fooling us into thinking we know more than we do. Furthermore, we can determine which regions of the source function are well-constrained by the data, and which are essentially unresolved.

4.3 The Backus-Gilbert method

The Backus-Gilbert method is one of a family of methods for attacking inverse problems. There are several general introductions to the method: Parker [67] gives an excellent review, and Loredo & Epstein [66] give an example in an astrophysical context. For a deep and rigourous treatment, the courageous reader is referred to Backus & Gilbert's 1970 paper [68]: in this section, we will try as far as possible to bring out the underlying physical ideas.

We wish to recover a *source function* $f(r)$. We cannot measure this function directly, but instead measure an integral of it, $G(\mathbf{s})$. For all the cases considered in this thesis, G is related to f through an integral of the form

$$G(\mathbf{s}) = \int_0^1 f(r)K(r;\mathbf{s})\,\mathrm{d}r, \tag{4.2}$$

where the kernel $K(r;\mathbf{s})$ can be calculated *a priori*. The set of N observations that we make, $g_i \equiv G(\mathbf{s}_i)$, is therefore related to the source function by

$$g_i = \int_0^1 f(r)K_i(r)\,\mathrm{d}r + n_i, \tag{4.3}$$

where $K_i(r) \equiv K(r;\mathbf{s}_i)$ and n_i is a random admixture of noise. From these measurements we wish to produce an estimator $\hat{f}(r)$ of the underlying function $f(r)$.

In the Backus-Gilbert method, we assume that the source function is related to the mean of its estimator through

$$E\left(\hat{f}(r)\right) = \int_0^1 \Delta(r,r')f(r')\,\mathrm{d}r', \tag{4.4}$$

where $\Delta(r, r')$ is known as the *averaging kernel.*

Now, since we do not know the underlying function, the averaging kernel is of no use to us directly; however we can study its properties, and use our data g_i in such a way as to optimise those properties, and so minimise the dependence of the estimate $\hat{f}(r)$ on the underlying function and the noise. It is clear from Eqn. (4.4) that $\hat{f}(r) = f(r)$ if $\Delta(r, r')$ is the Dirac delta function. However, such a solution is highly sensitive to noise in the data and hence very unstable. We attain stability by increasing the width of $\Delta(r, r')$, and hence smoothing the recovered value over a wider region of the source function – that is, we minimise the width of $\Delta(r, r')$ while trying to ensure that the resolution of $\Delta(r, r')$ remains sufficient for the problem at hand, in a sense we shall make more precise below.

We define the estimator $\hat{f}(r)$ through a set of *response kernels* $q_i(r)$, which produce an estimate of the underlying function through

$$\hat{f}(r) = \sum_i q_i(r) g_i. \tag{4.5}$$

If we substitute Eqn. (4.3) into Eqn. (4.5), and *assume* $E\left(\sum_i q_i(r) n_i\right) = 0$, i.e. that the weighted noise has zero mean, then Eqn. (4.4) implies

$$\Delta(r, r') = \sum_i q_i(r) K_i(r'). \tag{4.6}$$

This allows us to form some measure of the *width* of $\Delta(r, r')$ such as

$$\begin{aligned} \mathcal{A} &\equiv \int (r - r')^2 [\Delta(r, r')]^2 \, \mathrm{d}r', \qquad (4.7) \\ &= \sum_{ij} q_i(r) W_{ij}(r) q_j(r) \\ &= \mathbf{q}(r)^T \mathbf{W}(r) \mathbf{q}(r), \end{aligned}$$

where

$$W_{ij}(r) \equiv \int_0^1 (r' - r)^2 K_i(r') K_j(r') \, \mathrm{d}r' \tag{4.8}$$

and

$$\mathbf{q}(r)^T = (q_1(r), ..., q_N(r)). \tag{4.9}$$

This is the usual definition of the width; others are reasonable, and may be preferable in different circumstances (though Gough [63] asserts that the final result is not sensitive to the particular form of $\mathbf{W}$ provided it rises steeply enough for $r' >> r$).

Again assuming that $E(\mathbf{q} \cdot \mathbf{n}) = 0$, one can easily show that the variance of $\hat{f}$ is given by

$$\mathcal{B} \equiv \mathrm{Var}\, \hat{f}(r) = \mathbf{q}(r)^T \mathbf{S} \mathbf{q}(r), \tag{4.10}$$

where the noise covariance matrix $S_{ij} \equiv E(n_i n_j)$. In this thesis, we take the n_i to be independent and Gaussian with standard deviation σ; in this case, $S_{ij} = \delta_{ij}\sigma^2$, and our assumption $E(\mathbf{q} \cdot \mathbf{n}) = 0$ is necessarily satisfied.

Finally, the demand that $\Delta(r, r')$ be normalised, i.e.

$$\int_0^1 \Delta(r, r')\, \mathrm{d}r' = 1, \tag{4.11}$$

requires, from Eqn. (4.6),

$$\mathbf{q}(r) \cdot \mathbf{R} = 1, \tag{4.12}$$

where $R_i \equiv \int K_i(r)\, \mathrm{d}r$.

The Backus-Gilbert method consists of finding the set of $q_i(r)$ which minimise $\mathcal{A} + \lambda\mathcal{B}$, where

$$\begin{aligned} \mathcal{A} + \lambda\mathcal{B} &= \mathbf{q}(r) \cdot [\mathbf{W}(r) + \lambda \mathbf{S}] \cdot \mathbf{q}(r) \\ &= \int (r - r')^2 [\Delta(r, r')]^2\, \mathrm{d}r' + \lambda\, \mathrm{Var}\, \hat{u}(r), \end{aligned}$$

for some selected parameter λ, subject to the constraint $\mathbf{q} \cdot \mathbf{R} = 1$. The minimisation problem has the explicit analytic solution

$$\mathbf{q}_\lambda(r) = \frac{[\mathbf{W}(r) + \lambda \mathbf{S}]^{-1} \cdot \mathbf{R}}{\mathbf{R} \cdot [\mathbf{W}(r) + \lambda \mathbf{S}]^{-1} \cdot \mathbf{R}}. \tag{4.13}$$

Eqn. (4.5) then gives $\hat{f}_\lambda(r)$ in terms of the data g_i. The nature of the trade-off in the minimisation is clear: in order to improve the stability of the recovery, we choose a λ which makes $\Delta(r, r')$ broader, and so generate response kernels q_i which extend the weighted

average over a greater number of the data points g_i. The cost of this is that the estimate of the recovered point will be biased by the inclusion of the extra data, and this will be more marked when the underlying function is rapidly varying.

The Backus-Gilbert scheme is hardly transparent, and the best way to get a feel for how it works is to put it into practice (as we shall do in the next two chapters). In the meantime, we can gain some insight by looking again at equations 4.10 and 4.12. Consider the simple case where all the R_i are equal to 1 and the noise has $\sigma = 1$ so that $S_{ij} = \delta_{ij}$. Then Eqn. (4.12) becomes

$$\sum_{i=1}^{N} q_i = 1 \tag{4.14}$$

and Eqn. (4.10) becomes

$$\mathcal{B} = \sum_{i=1}^{N} q_i^2 \tag{4.15}$$

Eqn. (4.14) implies that as the number of data points (and hence the number of q_i increases, $\mathcal{B}$ will decrease, improving the recovery. This is what one would hope and intuitively expect, but it is now possible to quantify the impact of increased data on a particular inversion.

The first important point about the Backus-Gilbert method is that the parameter λ allows us to adjudicate between the conflicting demands of minimising the width of the kernel $\Delta(r, r')$ and minimising the sensitivity of the recovered value (which is a realisation of the statistical variable $\hat{f}_\lambda(r)$) to the measurement noise, and that this adjudication can be done *prior to any data being collected*, based only on the characteristics of the kernel $K(r; \mathbf{s})$ and the noise.

Secondly, we must emphasise that the $\mathbf{q}_\lambda(r)$ we obtain gives us, through Eqn. (4.5), a single point in the recovered function, $\hat{f}_\lambda(r)$. This means that in this simplest version of the Backus-Gilbert method we must perform the inversion for each value of r for which we wish to find $\hat{f}_\lambda(r)$. Since the calculation of the coefficients $\mathbf{q}_\lambda(r)$ involves a matrix inversion, which is an n^3 procedure, it can be computationally expensive, but this limitation will be acceptable in our particular case, as the number of data points will usually be $\lesssim 100$. This

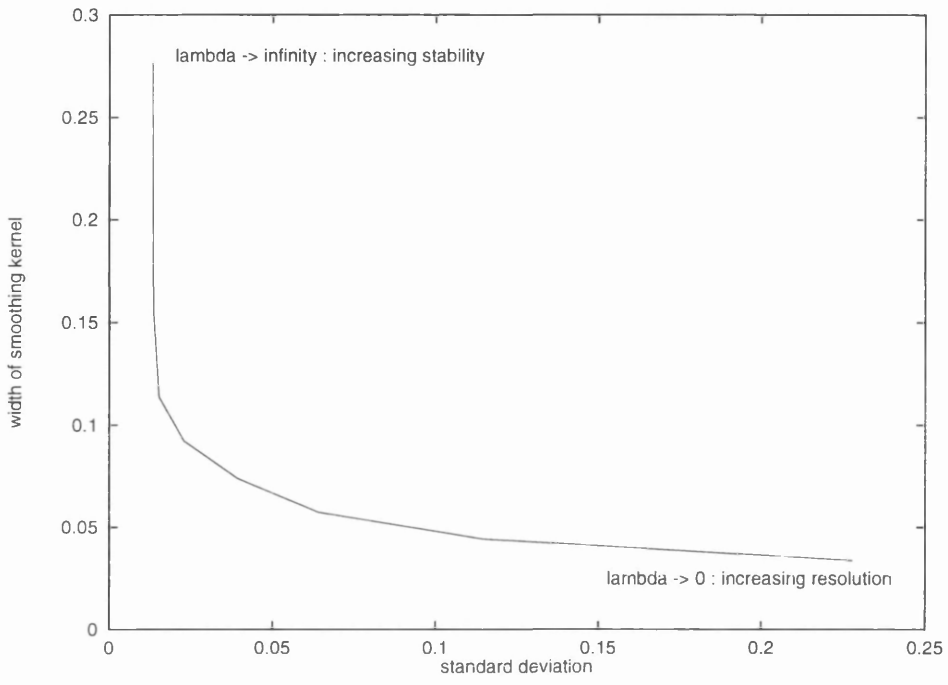

Figure 4.1: An example of a trade-off curve for the Backus-Gilbert inversion scheme.

feature has the compensation that we can if necessary select a different optimal value of λ for each recovered point. A modified, faster inversion method is presented in [69].

4.3.1 Theoretical limits on inversions

One strength of the BG method is that we can do a lot of the analysis before we have any data. This gives us an understanding of the limitations of our analysis, and allows us to pick an optimal value for the smoothing parameter λ.

Eqn. (4.13) produces a one-dimensional family of solutions, parametrised by λ. We can represent this as a solution curve on a graph of standard deviation of the recovered $\hat{f}$ against the chosen measure of the width of the resolution function : the resolution is inversely related to the width, so such a curve illustrates the trade-off between accuracy and bias in the recovered solution. Fig. 4.1 shows an example of a trade-off curve (in fact, this curve was generated from the kernels of Chapter 5, a purely arbitrary choice).

The features common to all these curves are that they are monotonic and non-increasing, approaching a minimum width at one limit and a minimum standard deviation at the other. (Proving this is rather involved: a thorough discussion and geometrical interpretation are provided in [68].) In general, one usually considers intermediate values of λ, around the turning point between the two extremes. Precisely which λ one chooses depends on the relative importance of stability and resolution in the particular problem.

It is clear from Fig. 4.1 that the high resolution can only be obtained at the cost of a high standard deviation in the recovered value. If we try to increase the accuracy, we end up no longer measuring the source function proper, but rather a "blurred" value of this function, smoothed by convolution with the averaging kernel. In general, $E\left(\hat{f}(r)\right) \neq f(r)$, and the more rapidly varying the function at the point of interest, the greater this biasing will be.

4.3.2 The method in practice

The Backus-Gilbert method is one of many inverse problem methods in which one functional of the recovered solution, $\mathcal{A}$, is minimised subject to *regulation* by another quantity $\mathcal{B}$. In this case, $\mathcal{A}$ is the width of the averaging kernel, and this is regulated by the variance of the estimate. In other inverse problem methods, the functional $\mathcal{A}$ is some measure of the goodness of fit between the data and the forward problem, such as a χ^2, regulated by the demand that the solution be smooth, or that some non-linear functional of the solution, such as its negentropy, be minimised.

So why pick this particular method out of the many possibilities? Well, one attractive feature is that it makes no prior assumptions about the form of the solution. But inverting data to find the source function is really the secondary role of the B-G method. Its main purpose is in distinguishing real features in the recovered solution from artifacts. By analysing a given observational setup, we can say just how much (or little) information can be obtained about the source function, and we can pick out those regions of the source which are well resolved.

In Chapter 5 we will obtain a number of trade-off curves for the problem of measuring

limb polarization in an eclipsing binary system. These will show us the limitations on such measurements, and indicate the best strategy for overcoming these problems. Then in Chapter 6 we will invert microlensing light curves from extended objects. The Backus-Gilbert analysis will indicate which regions of the source star can be well-recovered from a microlensing event, and will show the feasibility of using gravitational microlensing as a stellar imaging tool.

Chapter 5

Inversion of eclipsing binary light curves

Vila: "Avon, this is stupid!"

Avon: "When did that ever stop us?"

Blake's 7: Star One, Chris Boucher

5.1 Detection of limb polarization in eclipsing binaries

We are now in a position to apply the inversion theory of the previous chapter to the problem of imaging stellar surfaces. Eventually, this will involve inverting microlensing light curves (Chapter 6). Before that, however, a digression into eclipsing binary stars is in order. There are three reasons for this detour. Firstly, observations of eclipsing binaries have been used to constrain stellar limb polarization. This is clearly of interest as far as the feasibility of using polarimetry to obtain lens parameters is concerned: if the intrinsic limb polarization is too low, measurable polarimetric effects from microlensing are unlikely. Secondly, inverting eclipse light curves is a perfectly reasonable way in its own right of obtaining stellar surface information. And finally, the experience and insights

gained by tackling the relatively simple eclipsing case will prove invaluable when it comes to the much less intuitive problem of inverting microlensing data (see also [84].

Chandrasekhar ([71], [72]) calculated the polarization profile of a pure electron scattering atmosphere, showing that the degree of polarization is greatest at the limb ($\sim 11.7\%$ in this idealised case). Shortly thereafter ([73]) the first attempts were made to observe the effect of this limb polarization in the eclipse phase of a binary system, but it was not until the remarkably sensitive observations of the Algol system by Kemp et al. ([74]) that limb polarization was detected in this way.

Wilson and Liou ([75]) analyzed the Algol data to obtain a limb polarization in the primary of 0.219%. This was one of a large number of parameters they obtained by least-squares fitting a model to the data which included tidal and rotational distortion, gravity darkening, limb darkening, reflection, circumstellar polarization and an accretion stream. They simultaneously fitted the plane of rotation, residual constant polarization (interstellar or instrumental), circumstellar electron density, stream position and density and circumstellar cloud radius.

The dangers of such an approach should be evident from the previous chapter. With such an ill-conditioned problem it is easy to obtain an apparently excellent, but entirely wrong, parameter fit. In this chapter, we apply the Backus-Gilbert inversion scheme to the eclipsing binary problem.

5.2 An overview of the problem

We will assume that the light emerging from the stellar disk is partially linearly polarized perpendicular or parallel to the radial direction. One can calculate the total flux from the eclipsed star by integrating the intensity I over the visible part of the disc. Similarly, to obtain the total polarized flux one simply integrates the Stokes parameter Q over the same part of the disc, introducing a rotation factor to transform the polarized intensity at each point into the appropriate reference frame. The choice of frame is arbitrary: here,

the origin is at the centre of the eclipsed star and our x-axis is parallel to the transverse velocity of the occultor.

$$F_I(t) = \frac{1}{4\pi R^2} \iint_{\text{disc}} I(r)\, A(r,\chi,t) r\, dr d\chi \tag{5.1}$$

$$F_Q(t) = \frac{1}{4\pi R^2} \iint_{\text{disc}} Q(r)\, A(r,\chi,t) \cos 2\chi r\, dr d\chi \tag{5.2}$$

$$F_U(t) = \frac{1}{4\pi R^2} \iint_{\text{disc}} Q(r)\, A(r,\chi,t) \sin 2\chi r dr d\chi \tag{5.3}$$

where r, χ are polar coordinates on the stellar disk, R is the distance from the observer to the star, and $A(r,\chi,t)$ is zero for an occulted point on the disk, 1 otherwise.

Note that we assume the kernel $A(r,\chi,t)$ is known. This is equivalent to assuming that we already have some measurement of the stellar radii and the orbital elements of the system. The first of these can be obtained from the spectral classifications of the stars; the second, from the photometric light curve and/or spectroscopic observations (see [76] and references therein). We only consider spherically symmetric stars here, so we are assuming that the binary system is detached.

5.3 Kernels for the eclipsing case

In this section we derive the kernels for the case when one star is partially eclipsed by another. The geometry of this situation is as shown in Figs. 5.1 and 5.2.

We can take the occultor to be opaque, equivalent to subtracting off the occultor's (constant) flux from all measurements. Its 'transfer function' $A_0(d)$ is then

$$A_0(d) = \begin{cases} 0 & \text{for } d < \rho \\ 1 & \text{for } d > \rho \end{cases}, \tag{5.4}$$

where d is the (projected) radial distance from the centre of the *occultor*, and ρ is the radius of the occultor.

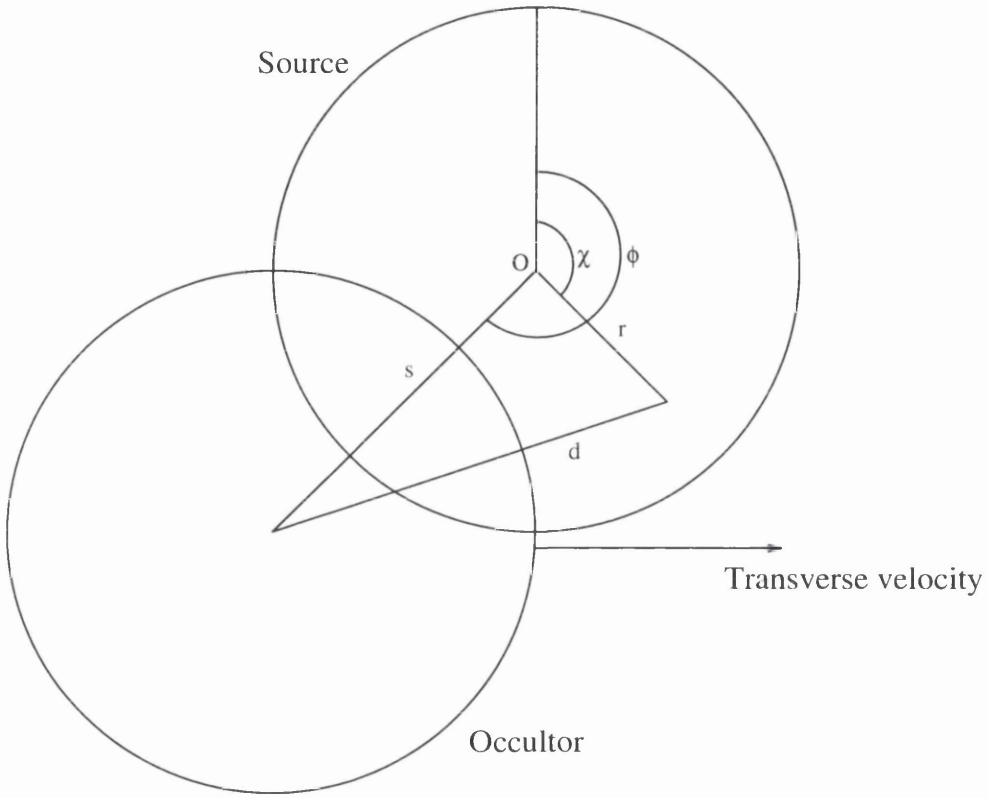

Figure 5.1: The coordinate system used in Section 5.3. (r, χ) are polar coordinates in the projected plane of the source, and $(s(t), \phi(t))$ are the coordinates of the centre of the occultor; both χ and ϕ are taken from a radius perpendicular to the transverse velocity of the occultor.

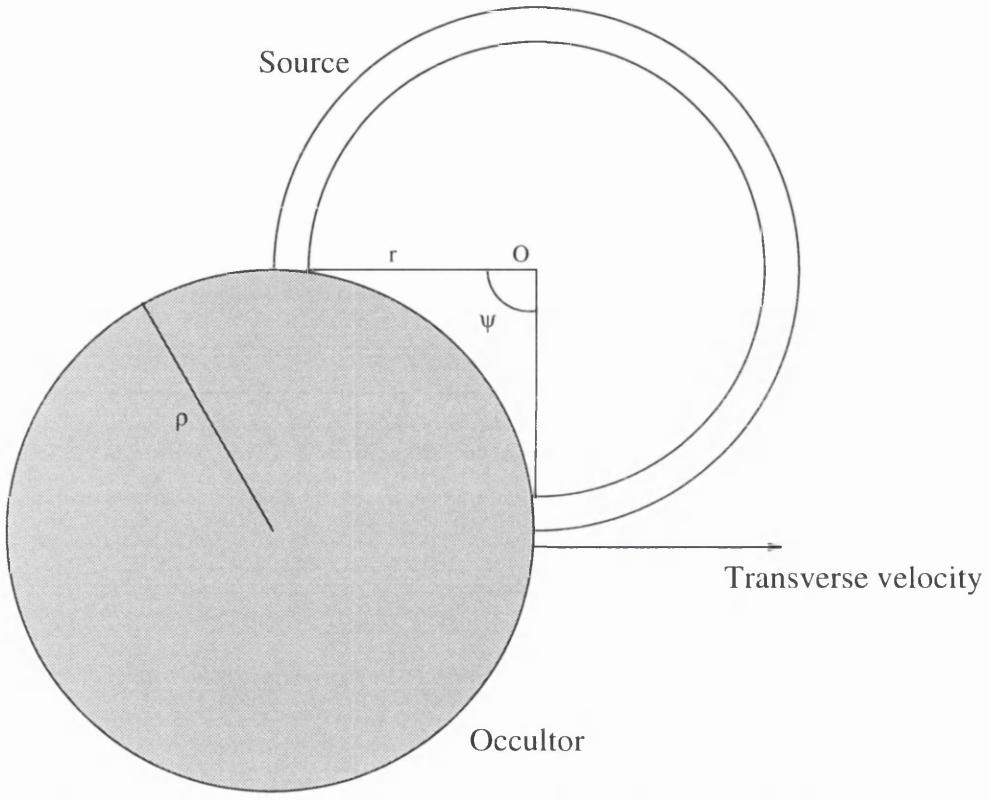

Figure 5.2: The eclipsed star has radius 1, and the occultor has radius ρ. For any annulus of radius r, the segment with opening angle $\psi(r; s; \rho)$ is occulted.

Here, the source star is spherically symmetric. In order to exploit that symmetry we use a polar coordinate system (r, χ) with its origin at the centre of the eclipsed star. In this coordinate system, the transfer function $A(r, \chi; s)$ does not have such a simple form.

In terms of $I(r)$, the intensity of the star as a function of (projected) radius, the total flux from the eclipsed star is

$$F_I(s) = \int_{\text{area}} I(r) A(r, \chi; s)\, r\, \mathrm{d}r\, \mathrm{d}\chi. \tag{5.5}$$

Now we would like to integrate the right-hand side of Eqn. (5.5) over χ: since the source star is spherically symmetric, the inverse problem is inherently one-dimensional. This allows us to reduce the inverse problem to the form of Eqn. (4.2), and hence to implement the techniques of Chapter 4.

We can rewrite Eqn. (5.5) in the form

$$F_I(s) = \int_0^1 I(r) \tilde{A}(r; s)\, \mathrm{d}r, \tag{5.6}$$

where $\tilde{A}(r; s) = r \int_0^{2\pi} A(r, \chi; s)\, \mathrm{d}\chi$. This is now in precisely the form we require (c.f. Eqn. (4.2)), with $I(r)$ as the unknown source function and $\tilde{A}(r; s)$ as the kernel. Once we have obtained an analytical expression for this kernel we can put the Backus-Gilbert inversion method to work.

It is easy to see that $\tilde{A}(r; s) = r \int_0^{2\pi - \psi(s)} 1\, \mathrm{d}\chi$. Writing $\gamma \equiv \cos[\psi(r; s)/2]$ we find that

$$\gamma = \begin{cases} 1 & , \quad 1 < \bar{\gamma} \\ \bar{\gamma} \equiv (r^2 + s^2 - \rho^2)/2rs & , -1 \leq \bar{\gamma} \leq 1 \\ -1 & , \quad \bar{\gamma} < -1 \end{cases} \tag{5.7}$$

We can now write

$$\tilde{A}(r; s) = \begin{cases} 2r(\pi - \psi/2) & \\ = 2r \arccos(-\gamma) & , |s - \rho| \leq r \leq s + \rho \\ 0 & , r < -(s - \rho) \\ 2\pi r & , \text{otherwise} \end{cases} \tag{5.8}$$

defined for $r \geq 0$.

The calculation is a little more intricate for the Stokes parameters. The light from each point on the star's disk must be linearly polarised in the tangential direction. Using the angle χ defined in Fig. 5.1, the Stokes parameters (in the (x, y) frame of Section 5.2) must therefore be $F_U(r, \chi) = -P(r) \sin 2\chi$ and $F_Q(r, \chi) = -P(r) \cos 2\chi$, for some function $P(r)$ which we wish to recover (note that we use the unnormalised Stokes parameters, since the normalised ones have contributions to the noise from the intensity as well as the polarization measurements). Defining

$$\tilde{A}_Q(r; s, \phi) = -r \int_0^{2\pi} \cos 2\chi A(r, \chi; s, \phi) \, \mathrm{d}\chi, \tag{5.9}$$

we therefore find that the total polarized flux in the Q direction, measured when the centres are a distance s apart, is

$$F_Q(s, \phi) = \int_0^1 P(r) \tilde{A}_Q(r; s, \phi) \, \mathrm{d}r, \tag{5.10}$$

and similarly for $A_U(r, \chi; s, \phi)$ and $F_U(s, \phi)$. This is now in the form of Eqn. (4.2). Setting $l = s \cos \phi$, we can thus see that

$$\begin{aligned} \tilde{A}_Q(r; s, \phi) &= r \cos 2\phi \sin \psi(r; s) \\ &= 2r \left(2\frac{l^2}{s^2} - 1 \right) \gamma \sqrt{1 - \gamma^2} \end{aligned} \tag{5.11}$$

$$\begin{aligned} \tilde{A}_U(r; s, \phi) &= r \sin 2\phi \sin \psi \\ &= 4r \frac{l}{s} \left(1 - \frac{l^2}{s^2} \right)^{\frac{1}{2}} \gamma \sqrt{1 - \gamma^2} \end{aligned} \tag{5.12}$$

Note that $s = s(t)$ and $\phi = \phi(t)$, so the kernels can also be expressed as $\tilde{A}(r, t)$, $\tilde{A}_Q(r, t)$ and $\tilde{A}_U(r, t)$. These kernels are broad and smooth, hence the ill-conditioning of the inverse problem.

In practice, we choose a reference frame such that $U \equiv 0$: this involves taking the Q, U data and rotating to a frame aligned along the line of centres, so that $\phi = 0$. This involves no loss of information, and simplifies the inversion since we now only have to work with one kernel function, $\tilde{A}_Q$.

5.4 Applying the Backus-Gilbert inversion

In the present case, we are interested in measuring the polarization at the limb, and it is clear from section 4.3.1 that the resolution we need can only be obtained at the cost of a high standard deviation in the recovered value. This is basically because almost all the polarized flux comes from a thin annulus at the limb, so if the solution is too smoothed the limb polarization will be greatly underestimated.

Looking at the low-λ limit (ie, no-noise), we find that the $\Delta(r, r')$ function is sharply peaked at $r = 1$, so that in principle we can extract a well-resolved limb-polarization (Fig. 5.3). In fact, the quality of this peak degrades substantially for $r < 1$: the method as presented *cannot* reasonably resolve polarizations on the disk. As we increase λ, the peak broadens, but the variance of the recovered $\hat{u}_\lambda(r)$ decreases.

Before we can go on to invert real or simulated data, we must decide what value of λ to use. To make that decision, we must consider the level and approximate functional form of the polarization P(r), and use this to set the scale for the resolution and standard deviation we need to achieve. In turn, this fixes the number of data points n we require in our data and the value of the parameter λ we must choose in our inversion. Despite the fact that we are invoking a particular model at this point in our analysis, we emphasise that this introduces no *practical* model dependence. We are using an approximate model purely to help us understand what counts as "sufficiently stable" or "sufficiently well resolved", and after this understanding is gained the numbers we recover remain model independent measurements, as opposed to any method of parameter fitting.

Firstly, Chandrasekhar suggests that the limb polarization is of the order of $P(1) = 0.117$; we therefore need a standard deviation which is at least as small as this. Secondly, if we are not to have an overly biased result, our resolution function must be narrow compared with the width of the underlying function $P(r)$. The resolution we need is therefore of order Width$[P(r)]$, where we define a width measure $\mathcal{A}$ analogous to Eqn. (4.7),

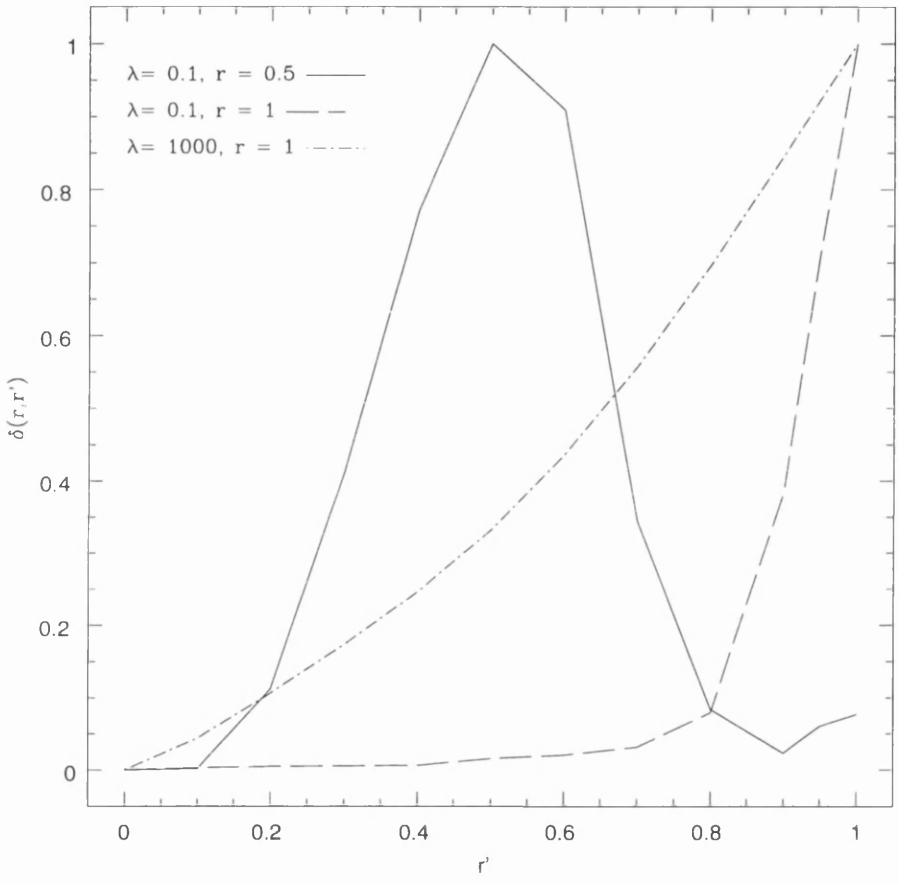

Figure 5.3: The averaging kernel $\Delta(r, r')$ as a function of r' for three different cases. The increase in the width of $\Delta(r, r')$ as λ increases is clear. Note the poor resolution at $r = 0.5$, even when λ is small. (Here there were 60 data points, with $\sigma = 0.017$.)

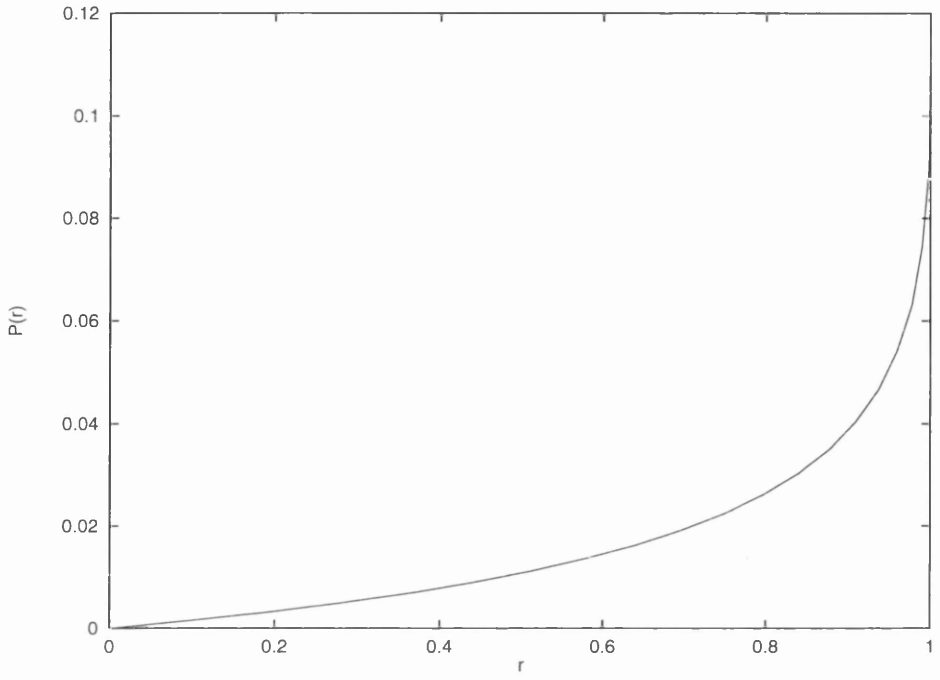

Figure 5.4: The polarization profile for a Chandrasekhar model atmosphere

$$\mathcal{A} \equiv \int (r - r')^2 [P(r')]^2 \, \mathrm{d}r'. \tag{5.13}$$

For the profile in Fig. 5.4, $\mathcal{A} = 0.031$ at the limb. These parameters allow us to define a region on the tradeoff diagram within which an acceptable inversion must lie. It is worth noting that the Chandrasekhar profile is particularly broad and has an especially high peak.

The trade-off curves for a number of different data sets are shown in Fig. 5.5. The region of acceptable solutions is contained within the box. The maximum accuracy achievable for a given resolution (or vice versa) can be read off from the graph.

All these cases are based upon the same eclipse parameters: the stars are of equal radii, and the impact parameter is 1 stellar radius. Tradeoff curves are plotted for 25, 50, 100 and 200 data points, with Gaussian data noise ($\sigma = 0.02$ in units of the unpolarized flux). Even the $n = 200$ case is only marginally acceptable. Given that the acceptability region is rather generous, we can say that such noisy data will not give any reasonable estimate

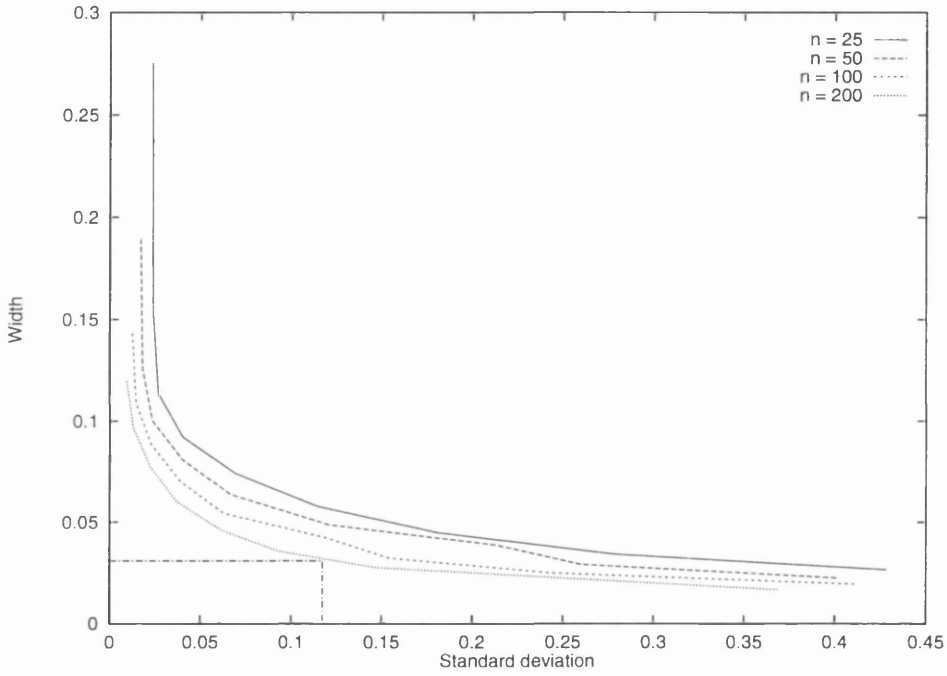

Figure 5.5: A series of trade-off curves for the polarization inversion. The region of acceptable solutions is contained within the box. (The stars are of equal radii, and the impact parameter is equal to the stellar radius: here, the noise level $\sigma = 0.02$)

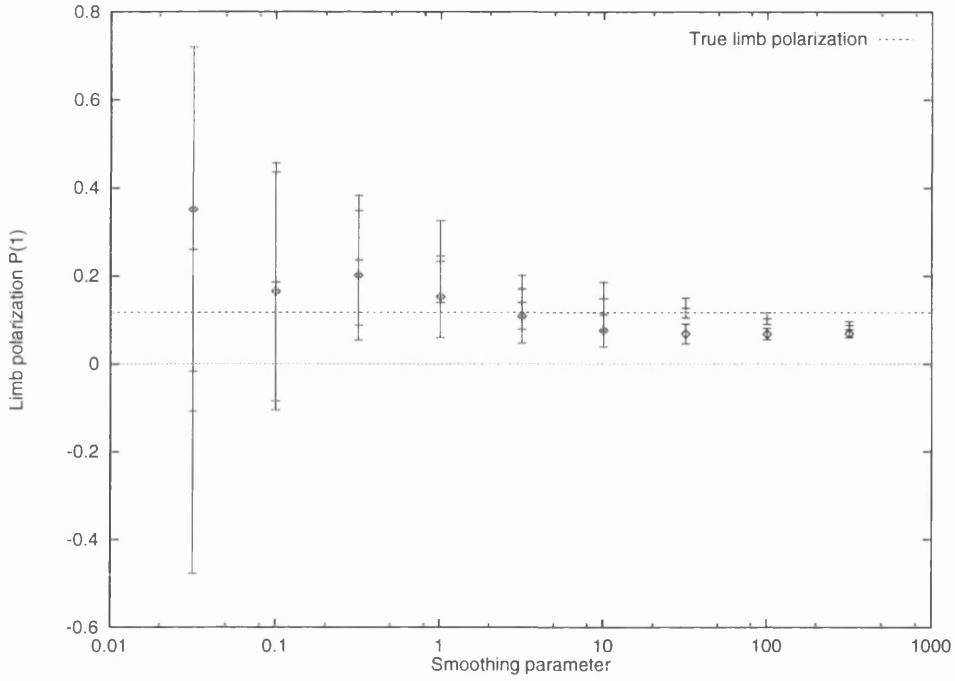

Figure 5.6: The recovered values of P(1) for two realisations of noisy simulated data with the same parameters. The horizontal line is the correct value of P(1).

of the limb polarization in this particular binary configuration.

The effect of the smoothing is illustrated in Fig. 5.6, which shows the recovery of the limb polarization from two sets of simulated noisy data, each with 200 data points, as a function of the smoothing parameter. It is clear that the solution becomes more stable as greater smoothing is imposed. However, this also causes the recovered value to be averaged over more and more of the stellar disk, gradually biasing it to lower values.

We can now adjust the various parameters to see how this situation can be improved.

5.4.1 Noise level

Reducing the noise by an order of magnitude greatly improves the situation. Fig. 5.7 shows that a reasonable inversion is now possible. A limb polarization profile about twice as sharp as the Chandrasekhar profile can be detected with this data, if the polarization level is as high as 11.7%. Conversely, if the actual limb polarization is only one tenth of

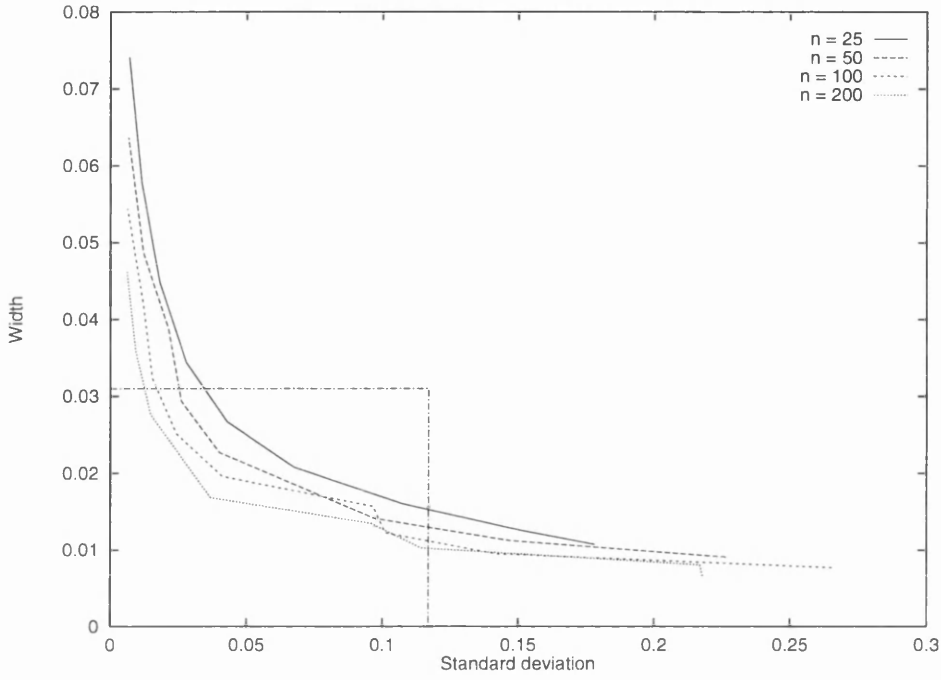

Figure 5.7: Noise level $\sigma = 0.002$. The stars are of equal radii, and the impact parameter is equal to the stellar radius.

the Chandrasekhar level it can still be detected with 200 data points - provided the profile is broad.

If we reduce the noise by another factor of ten we obtain the results in Fig. 5.8. Here we see that the number of data points is of little importance when the data is nearly noise-free. This is not too surprising, as the light curve will be well represented by only a few points in this case, and adding more points will not greatly improve the curve.

The most important point in this case is that the resolution rapidly approaches its theoretical limit. No matter how good the data, it cannot resolve limb polarization features narrower than 0.003 stellar radii. If the actual profile is this sharp, the only way to resolve it is to study another eclipsing binary system, with different orbital parameters.

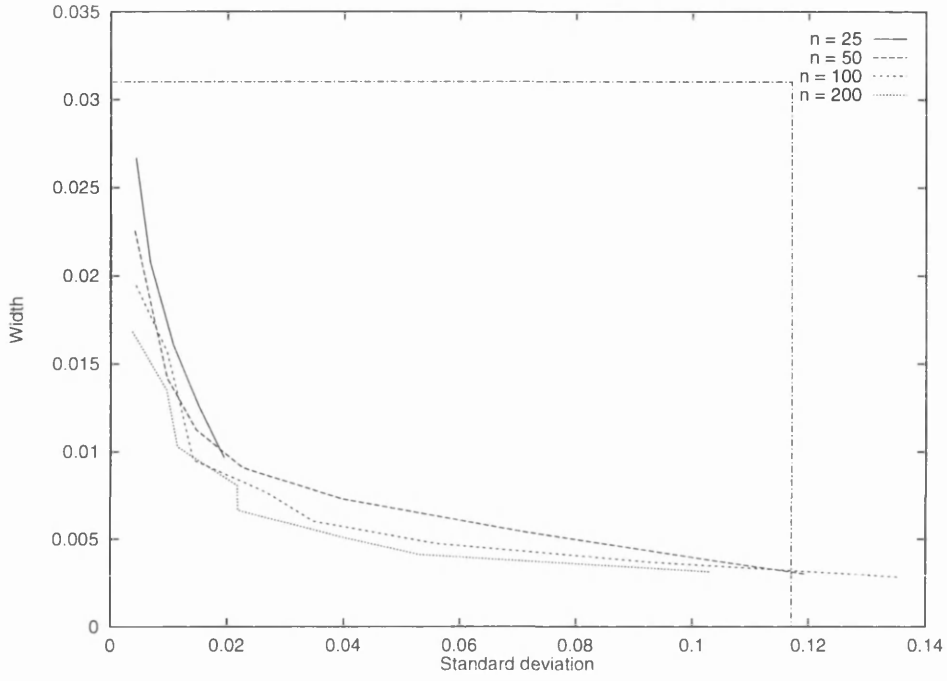

Figure 5.8: Noise level $\sigma = 0.0002$. The stars are of equal radii, and the impact parameter is equal to the stellar radius.

5.4.2 Impact parameter

Changing the impact parameter has a less drastic, but still significant, effect. Fig. 5.9 shows the case of a near-total eclipse, with all other parameters as in Fig. 5.5. There is a clear improvement, with 5% polarization now on the threshold of detectability. This improvement comes about because at the time of maximum eclipse the light from the occluded star comes from a small narrow region of the limb - exactly the place of interest. As the impact parameter increases, more of the star is visible and so the signal is increasingly lost (Figs. 5.10 and 5.5).

One might expect a similar effect from a near-grazing eclipse: the polarization signal obtained from occulting a small part of the limb should be as informative as the case where all but the limb is covered. In fact this is very far from the truth, as Fig. 5.11 illustrates. The reason is that the polarization is washed out by the unpolarized flux from the inner part of the stellar disk that is never eclipsed. The resulting weak signal

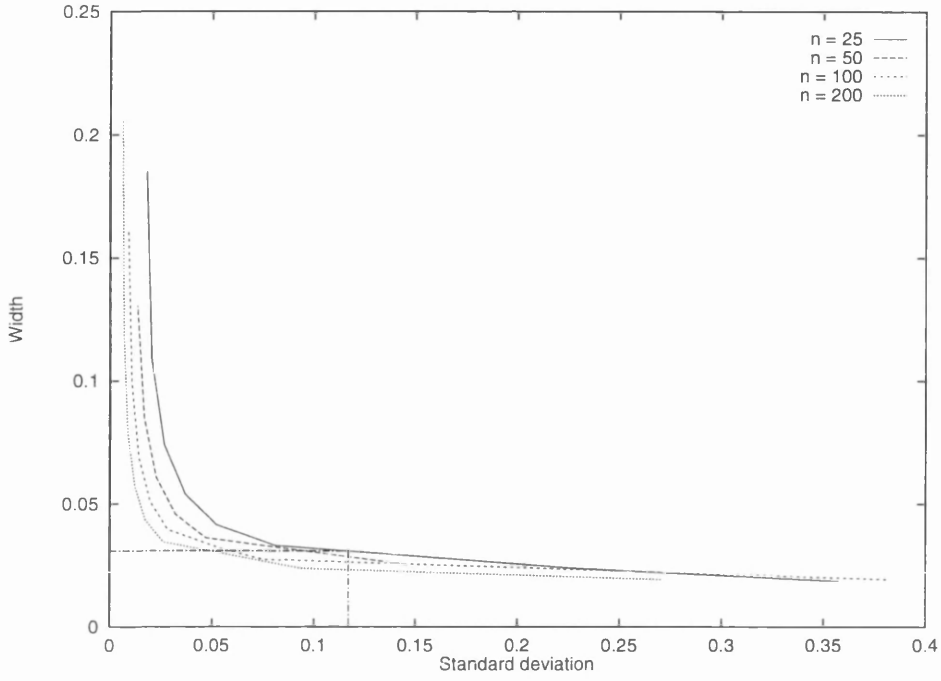

Figure 5.9: Impact parameter = 0.1 stellar radii. (σ = 0.02, equal stellar radii.)

is so thoroughly dominated by noise as to be virtually useless. Only when there are very many data points does the tradeoff curve enter the acceptable region, showing that a little information is making it through the noise.

5.4.3 Occultor radius

If changing the impact parameter afforded at best a factor of two improvement, could altering the radius of the occulting star give more impressive results? The answer, unfortunately, is no. It seems that the ideal case is when both stars are of approximately equal size: the results from both a smaller occultor (Fig. 5.12) or a larger (Fig. 5.13) are far worse than in the case of equal sizes (Fig. 5.5).

5.4.4 The best combination

Having studied the effects of altering the various parameters individually, we can now look at their effects in combination. Rather than calculate results for all the possible per-

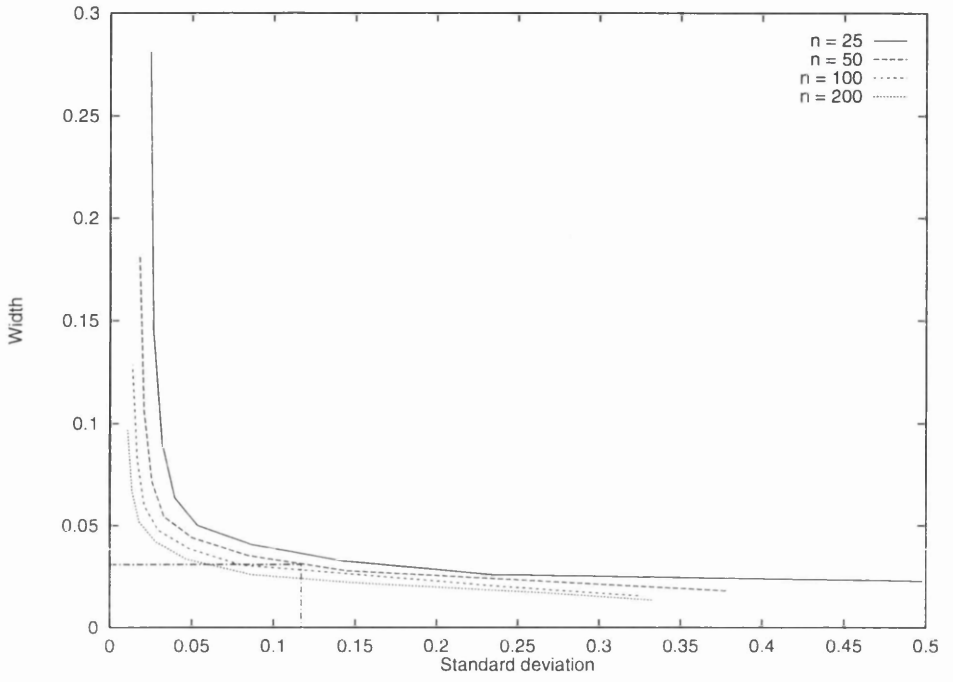

Figure 5.10: Impact parameter = 0.5 stellar radii. ($\sigma = 0.02$, equal stellar radii.)

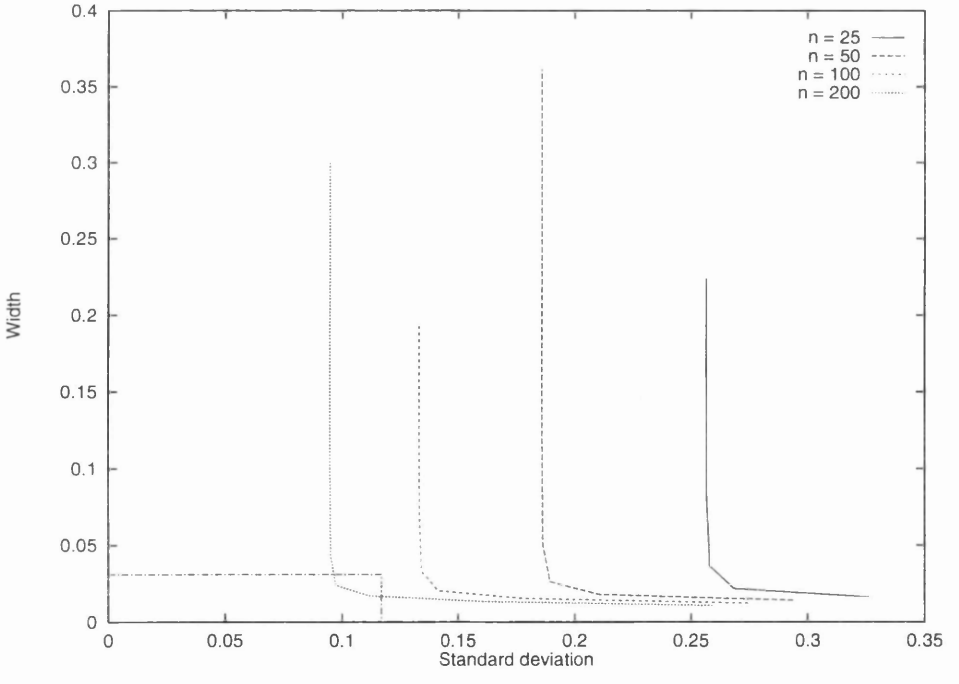

Figure 5.11: Impact parameter = 1.9 stellar radii. ($\sigma = 0.02$, equal stellar radii.)

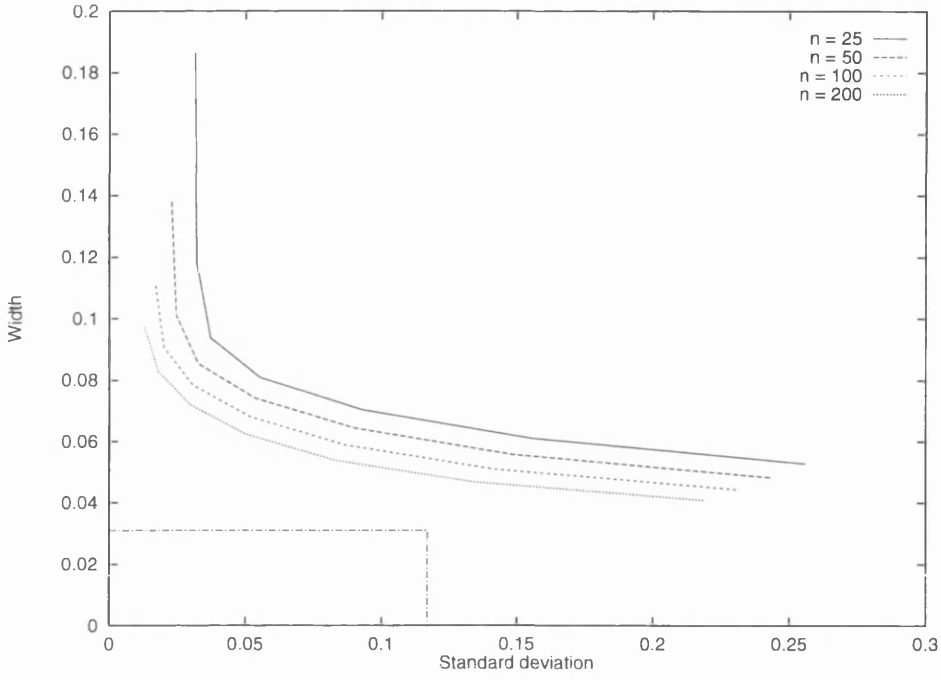

Figure 5.12: Occultor radius = 0.5 stellar radii. (σ = 0.02, impact parameter = 1 stellar radius.)

mutations, we can simply take the parameters from above which gave the best inversions and put them together to see what a "best-case" result looks like. Specifically, low-noise (σ = 0.0002), well-sampled (200 points) data from a system of two stars of equal size with near-total eclipse (impact parameter = 0.1 stellar radii).

The resulting tradeoff curve is shown in Fig. 5.14. The limits of the curve are instructive. Firstly, when the noise level is very small it is possible to reduce the standard deviation of the recovered value almost to zero. This is clearly good news if one wishes to measure low levels of limb polarization. The real problem comes at the other limit. We quickly reach the absolute resolution limit for this case, which turns out to be 0.00330 stellar radii. If we want to measure narrow limb polarization profiles, this resolution maximum will be the ultimate limiting factor. Looking at the intermediate case, a limb polarization $\sim$ 1% of width $\sim$ 0.005 stellar radii is just detectable in such a system.

It is quite clear from this analysis that choosing the right system to observe is at least

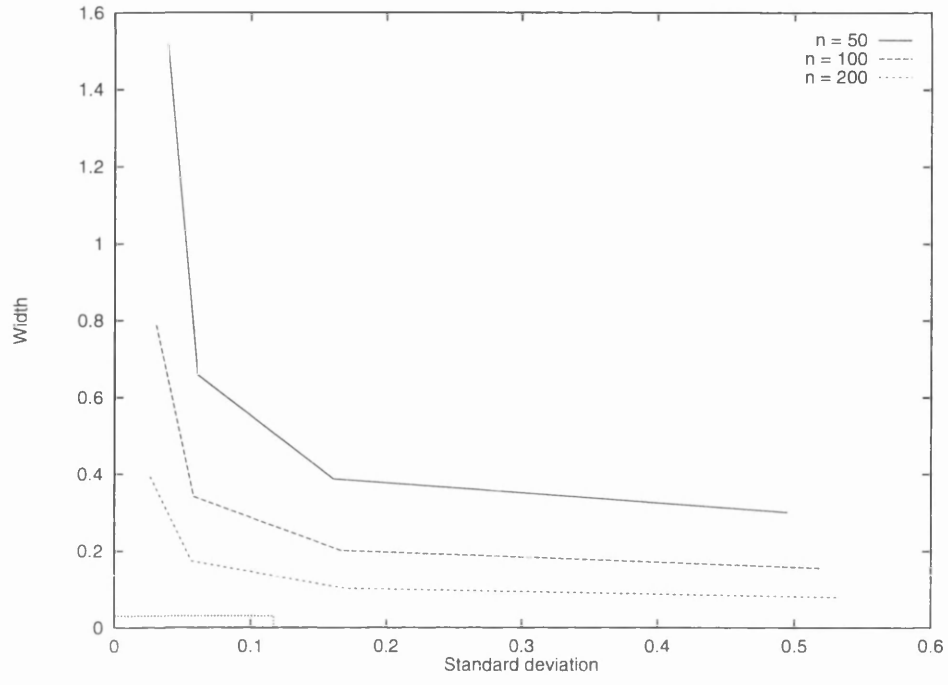

Figure 5.13: Occultor radius = 2 stellar radii. (σ = 0.02, impact parameter = 1 stellar radius.)

as important as obtaining the best possible data. What may be surprising is the limited improvement given by increasing the number of data points. It seems that a few high quality measurements of the right eclipsing system are worth far more than any amount of data from the wrong one.

5.5 Limb darkening profiles

In Section 5.3, we derived kernels for the unpolarized flux, as well as the polarized signal. We can use these to determine the limb darkening of the eclipsed star: that is, to estimate $I(r)$ across the stellar disk.

Limb darkening is not really the focus of this chapter, so we will just illustrate the basic idea with a small number of examples. This will give a slightly different perspective on the inversion method and its results, and will also anticipate the next chapter, in which

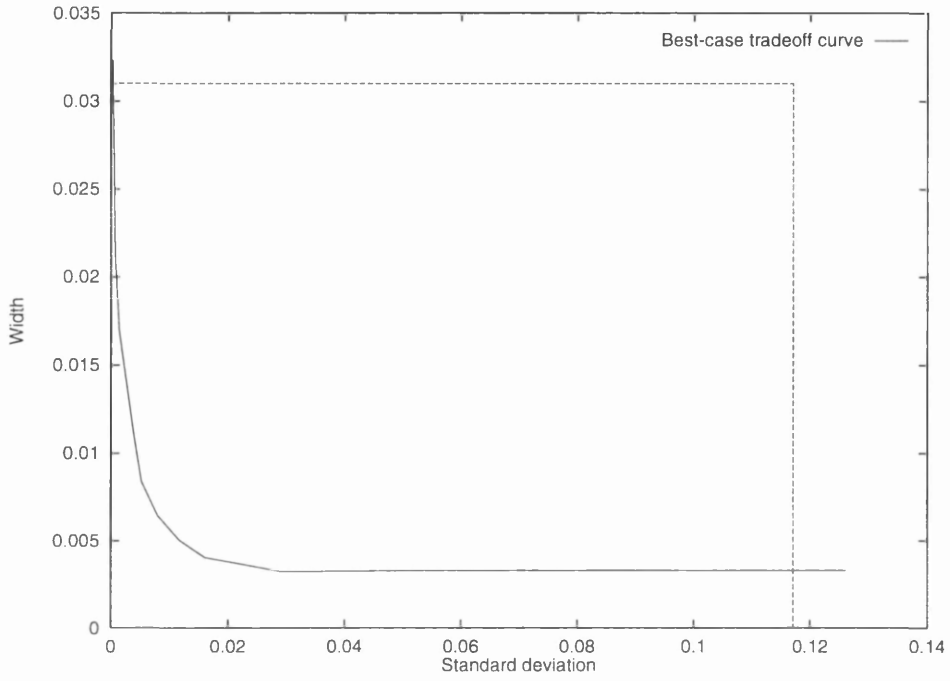

Figure 5.14: A "best-case" result, using a combination of the best parameters in previous sections: 200 data points, $\sigma = 0.0002$, impact parameter = 0.1 stellar radii.

microlensing light curves are inverted.

Here, we will only consider the case where both stars are of equal radius, and the eclipsed star has a linear limb-darkening profile

$$I(\mu) = I_0(1 - u(1 - \mu)) \tag{5.14}$$

where the emergent angle $\mu = \sqrt{1 - r^2}$ and u is the limb darkening coefficient. In this section, we adopt $u = 0.82$.

Figs. 5.15 to 5.17 show the inversion results for three different impact parameters, plotted against the true intensity profile. In these cases, the noise level $\sigma = 2\%$ of the baseline flux. This is rather a high error estimate for an eclipsing binary light curve: it has been chosen to allow easier comparison with the microlensing results of Chapter 6.

The most immediately obvious point about these figures is that the central portions of the disk are not recovered at all well. This is not so surprising, as these regions are eclipsed

for the least amount of time and therefore contribute least to the overall behaviour of the light curve. By contrast, the regions towards the limb are rather more accurately inverted, and the quality of the inversion increases as the eclipse becomes more nearly total. This is consistent with the behaviour noted in Section 5.4.2 for the polarization inversion.

What does come out very clearly in these figures is the biasing effect of the smoothing kernels. The limb intensity is in general overestimated, while the intesity at small r is underestimated. This is simply because the inversion at a particular point is stabilised by averaging over a region of the stellar disk - thus, the results are biased toward the average intensity. In these first three cases, the data quality is poor and so the trade-off between stability and bias leads to a fairly biased result with large error bars.

The next three figures (Figs. 5.18 to 5.20) show the same situation, but with much less noisy data ($\sigma = 0.005$, c.f. [78]). As the impact parameter decreases, a greater and greater region of the disk can be recovered reasonably accurately without unacceptable bias, until when the impact parameter is 0.1 stellar radii, only the extreme centre and edge of the star are poorly recovered.

In the next chapter we will perform similar inversions to these, but with microlensing light curves. One might expect the regions of the star closest to the projected lens position to be well resolved compared to the eclipsing results, and unlike eclipsing it does not seem that the lens will necessarily have to transit the source. We shall see how true these intuitive ideas are in Chapter 6.

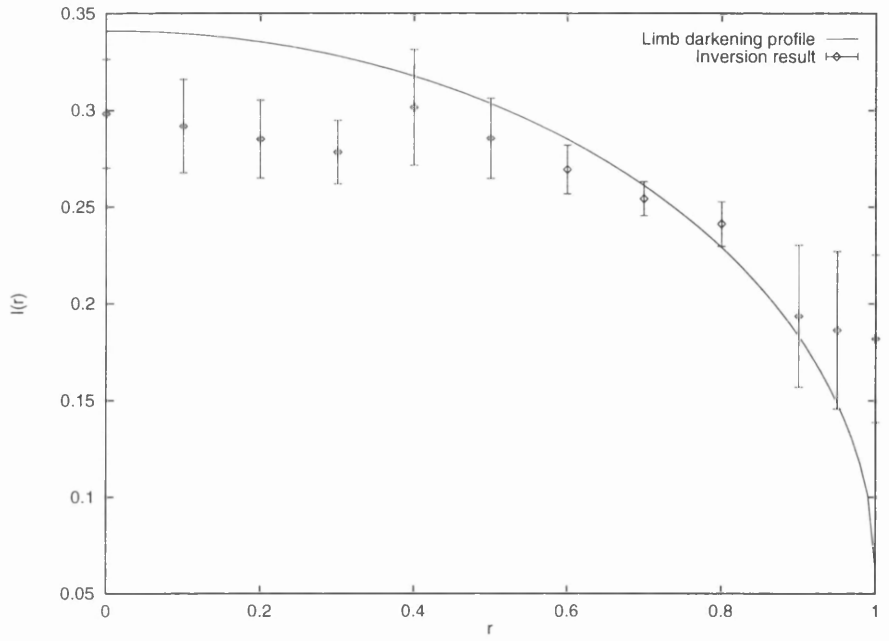

Figure 5.15: Model limb darkening profile and eclipse inversion results. Impact parameter = 1 stellar radius, $\sigma = 0.02$.

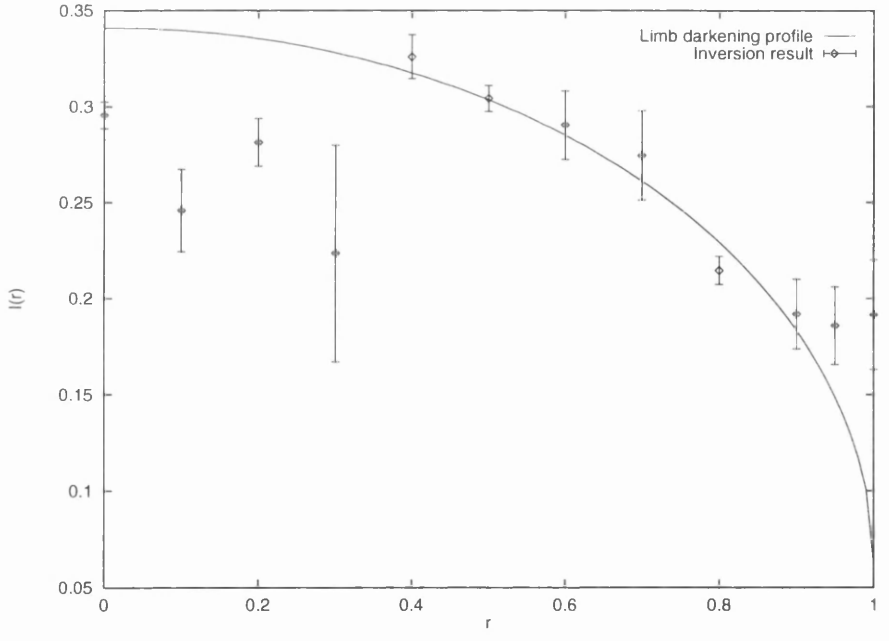

Figure 5.16: Model limb darkening profile and eclipse inversion results. Impact parameter = 0.5 stellar radii, $\sigma = 0.02$.

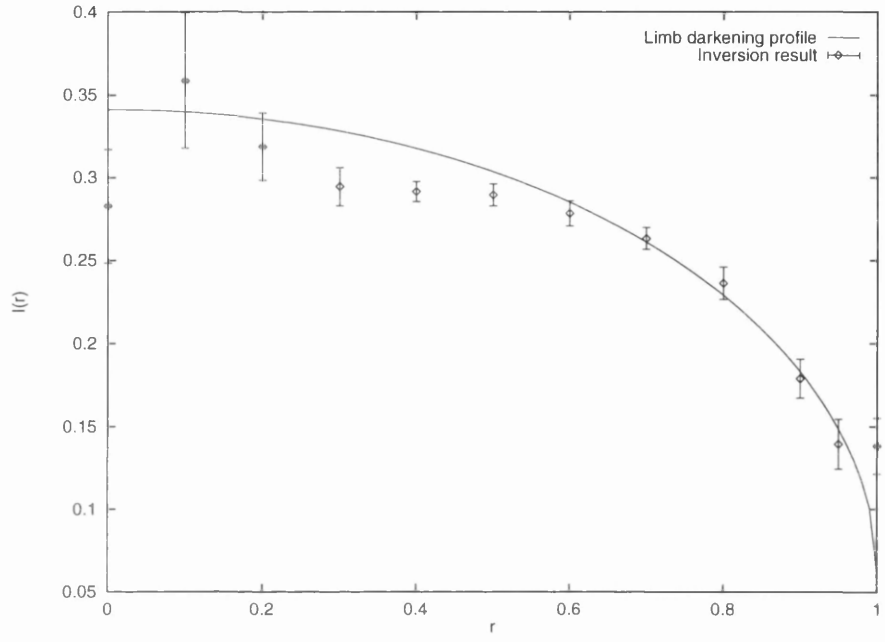

Figure 5.17: Model limb darkening profile and eclipse inversion results. Impact parameter = 0.1 stellar radii, $\sigma = 0.02$.

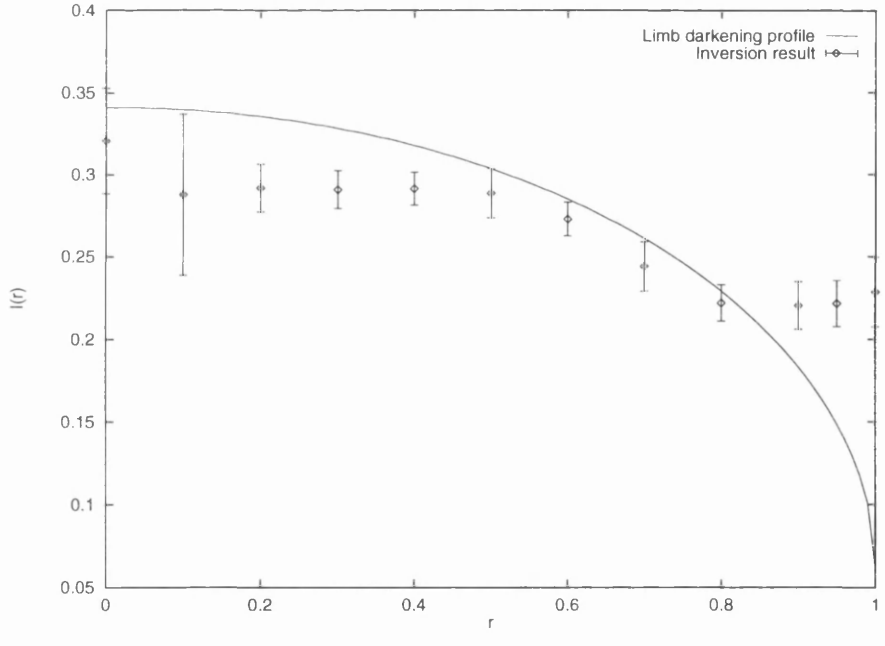

Figure 5.18: Model limb darkening profile and eclipse inversion results. Impact parameter = 1 stellar radius, $\sigma = 0.005$.

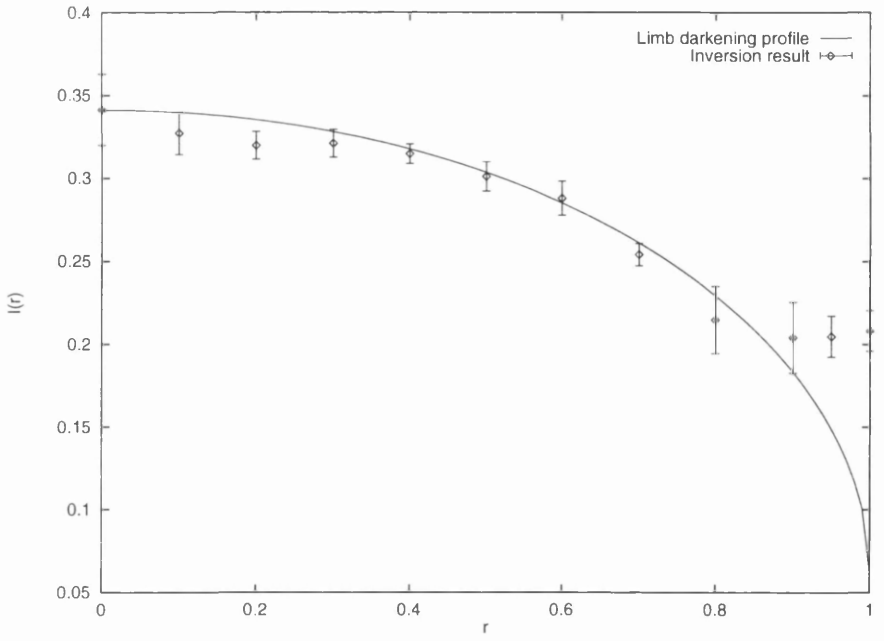

Figure 5.19: Model limb darkening profile and eclipse inversion results. Impact parameter = 0.5 stellar radii, $\sigma = 0.005$.

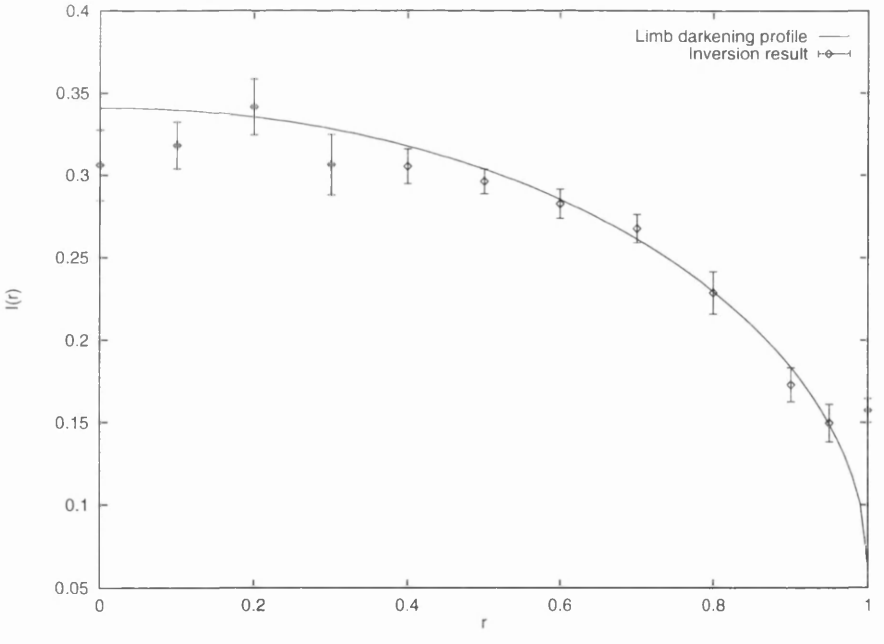

Figure 5.20: Model limb darkening profile and eclipse inversion results. Impact parameter = 0.1 stellar radii, $\sigma = 0.005$.

Chapter 6

Inversion of microlensing light curves

Seek, then,
No learning from the starry men,
Who follow with the optic glass
The whirling ways of stars that pass -
Seek, then, for this is also sooth,
No word of theirs - the cold star-bane
Has cloven and rent their hearts in twain,
And dead is all their human truth.

W.B. Yeats

6.1 Microlensing as a probe of stellar atmospheres

As a child, I was crestfallen to learn that no telescope on Earth could resolve a stellar disk, that the vast, beautiful stars described in my books would never be more than points of light. Later in life, it became clear that the radiation field of any stellar model would always

have to be integrated over the whole disk before any observational predictions could be made. Of course, there are cunning methods of teasing structural information out of the integrated light, from old standbys like rotational line broadening to sophisticated new techniques such as interferometry and Doppler image tomography [79]. Such approaches, while very useful, are somewhat unsatisfactory for two reasons. Firstly, any one technique is only suitable for a limited class of star; secondly, they are intrinsically model-dependent.

Microlensing offers a direct way of imaging a stellar surface, without making any model assumptions about the structure of the atmosphere. Furthermore, it can happen to any kind of star. The only drawbacks are that microlensing is a random, uncontrollable event and that the resulting light curve is not easy to interpret.

This chapter will focus on the latter issue, using the inversion methods from previous chapters to assess the informational content of microlensing data and to reconstruct surface brightness profiles (see also [86]). Sadly, arranging controlled microlensing on demand is beyond human ability.

6.2 Kernels for the microlensing case

The microlensing amplification function $A(r,\theta)$ is given by

$$A(r,\theta,d) = \frac{1}{2}\left[\left(1+\frac{4}{\zeta^2}\right)^{\frac{1}{2}} + \left(1+\frac{4}{\zeta^2}\right)^{-\frac{1}{2}}\right] \tag{6.1}$$

where

$$\zeta = r^2 + d^2 - 2rd\cos\theta \tag{6.2}$$

in the coordinate system of Fig. 6.1.

We can write the integrated flux F_i from the lensed star when the lens is at a distance d_i in the form

$$F_i(t) = F(d_i) = \int_0^R I(r)\tilde{A}_i(r)\,dr \tag{6.3}$$

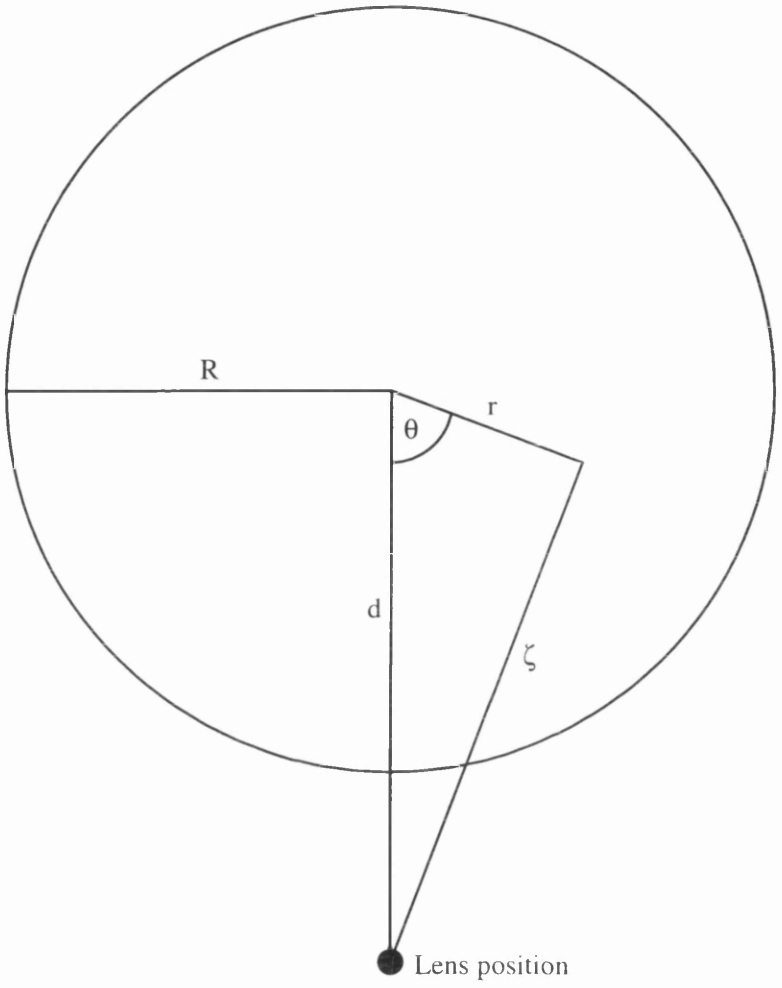

Figure 6.1: A microlensing object at a projected distance d (in the source frame) from the center of a spherically symmetric source of radius R.

where

$$\tilde{A}_i(r) = \int_0^{2\pi} A(r, \theta, d_i) r \, d\theta \tag{6.4}$$

This can be expressed in terms of elliptic integrals as

$$\tilde{A}_i(r) = 2\pi r - 2\xi \left\{ (x_1 - \bar{x}_1) \left[\Pi(n_1|w) - \Pi(\bar{n}_1|w) \right] + (a_1 - a_2) K(w) \right\} r \tag{6.5}$$

$$= 2\pi r - \xi \left\{ (x_2 - \bar{x}_2) \left[\Pi(n_2|w) - \Pi(\bar{n}_2|w) \right] + (a_2 - a_1) K(w) \right\} r \tag{6.6}$$

where

$$n_1 = x_1 \frac{x_2 - x_1}{x_1 x_2 - 1}$$

$$\bar{n}_1 = \frac{1}{x_1} \frac{x_2 - x_1}{x_1 x_2 - 1}$$

$$n_2 = x_2 \frac{x_1 - x_2}{x_1 x_2 - 1}$$

$$\bar{n}_2 = \frac{1}{x_2} \frac{x_1 - x_2}{x_1 x_2 - 1}$$

$$w^2 = n_1 \bar{n}_1 = n_2 \bar{n}_2 = \left(\frac{x_2 - x_1}{x_1 x_2 - 1} \right)^2$$

$$\xi = \frac{2\sqrt{x_1 x_2}}{x_1 x_2 - 1}$$

$$x_1 = a_1 + \sqrt{a_1^2 - 1}$$

$$x_2 = a_2 + \sqrt{a_2^2 - 1}$$

$$\bar{x}_1 \equiv \frac{1}{x_1}$$

$$\bar{x}_2 \equiv \frac{1}{x_2}$$

$$a_1 = \frac{r^2 + d_i^2}{2rd_i}$$

$$a_2 = \frac{4 + r^2 + d_i^2}{2rd_i}$$

and Π and K are elliptic integrals of the third and first kind respectively [80]. (This formulation of the kernel is due to Norman Gray: a brief derivation can be found in Appendix B.)

In this form, the kernels $\tilde{A}_i$ can be integrated numerically with a standard Gaussian quadrature. We can insert these into the Backus-Gilbert formalism of the previous chapter.

We will consider only the unpolarized light curves, and discuss basic chromatic effects, using a simple model stellar atmosphere. We will not treat line profiles here, as this would involve rather more complex atmosphere modelling, although the method could clearly be extended to this case. Furthermore, we do not invert any polarized light curves, as this would involve integrating the kernel as in Eqn. (6.5), but with an additional rotation factor. This introduces substantial mathematical difficulties, so we are at present confined to inverting the unpolarized signal.

6.3 Inversion of simulated data

This section seeks to answer the following questions:

1. How well can the intensity (or limb darkening) profile be reconstructed from a microlensing light curve?
2. How well can the colour dependence of this profile be determined?
3. How sensitive are these reconstructions to the lens parameters?
4. What improvements are possible with more extensive and accurate data?

6.3.1 Limb darkening profiles

Here we use the commonly-adopted linear intensity profile

$$I(\mu) = I_0(1 - u(1 - \mu)) \tag{6.7}$$

where the emergent angle $\mu = \sqrt{1 - r^2}$ and u is the limb darkening coefficient. These coefficients have been calculated by Claret & Giménez [81] for a range of stellar models with effective temperatures from $4000K$ to $6730K$ and surface gravity $\log g$ in the range 2.0 to 4.6.

The simulated data here assumed impact parameter and Einstein radius equal to the stellar radius. There were 100 data points, each with Gaussian noise added (standard deviation 2% of baseline flux). This is broadly in line with the actual data from the MACHO project (see e.g. [58]), although it is worth noting that the PLANET and GMAN projects can achieve considerably more accurate photometry . Results of the inversions are shown in Figs. 6.3 to 6.12.

In the upper figures, the error bars indicate the standard deviation of the recovered intensity, and thus the stability of the inversion at that point. The lower figures show the width of the averaging kernel at each point. These widths are indicated by vertical lines: the longer the line, the smoother the kernel. It might have been more intuitive to represent this by horizontal rather than vertical lines, but in practice such a presentation is cluttered to the point of incomprehensibility.

It is clear that the limb darkening profile is best recovered in the region $0.6 \lesssim r \lesssim 0.9$. At the limb, the recovery is somewhat more unstable since this is where the resolution must be narrowest. We can also see that the light curves contain virtually no information about the region $r \lesssim 0.5$: the results here are smoothed over most of the disk, and without such drastic smoothing are so unstable as to be meaningless.

The quality of the inversion is essentially unaffected by the limb darkening coefficient: in all cases the only useful information is in the region $r \gtrsim 0.6$.

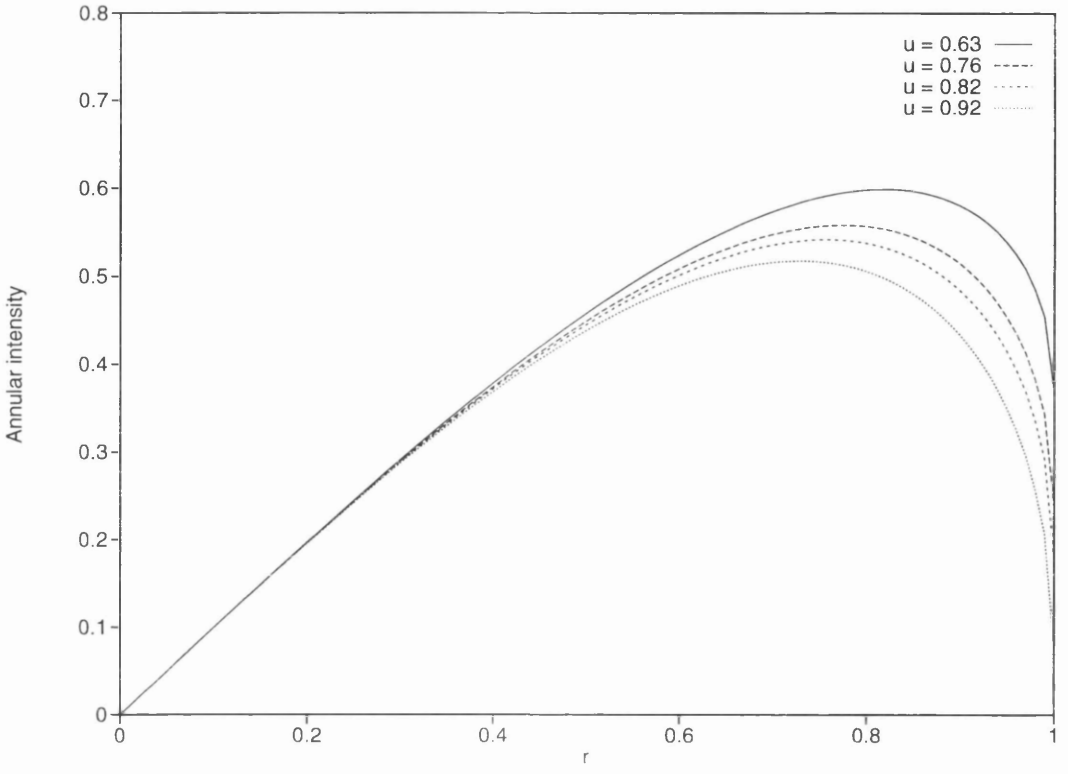

Figure 6.2: The function $\tilde{I}(r)/\pi I_0$ for four values of the limb darkening coefficient u.

Some indication of why this should be can be seen in Fig. 6.2. In the absence of lensing, the flux from an annulus on the disk, at a radius r and of width $\mathrm{d}r$ is $I(r)\pi r\mathrm{d}r \equiv \tilde{I}(r)\mathrm{d}r$. Clearly the region of the disk which makes the greatest contribution to the total flux is also the region which can most accurately be reconstructed from the light curve.

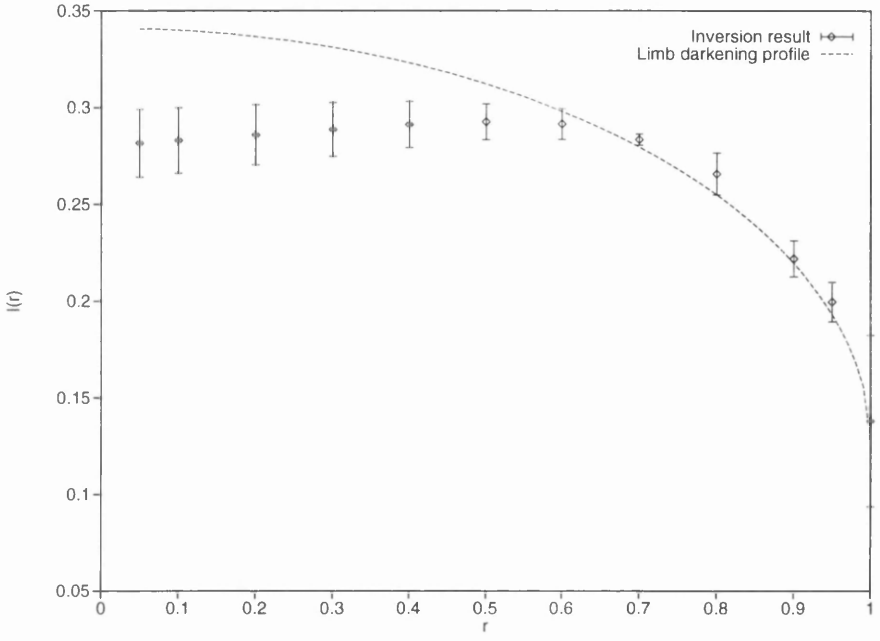

Figure 6.3: Inversion results for limb darkening coefficient $u = 0.63$. 100 data points, $\sigma = 0.02$, impact parameter = Einstein radius = stellar radius. Error bars indicate the standard deviation of the recovered intensity.

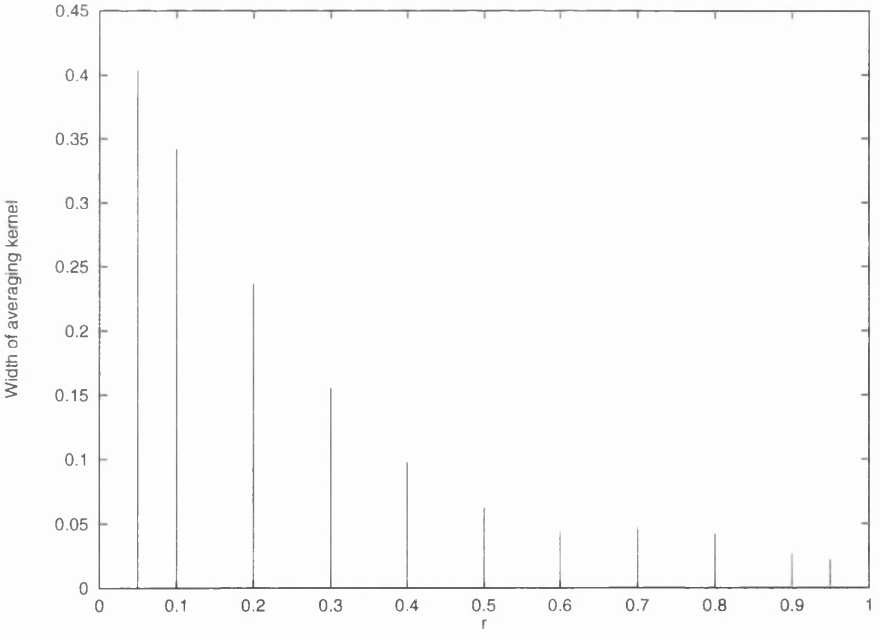

Figure 6.4: The width of the averaging kernel at each point for the $u = 0.63$ inversion, in units of the stellar radius.

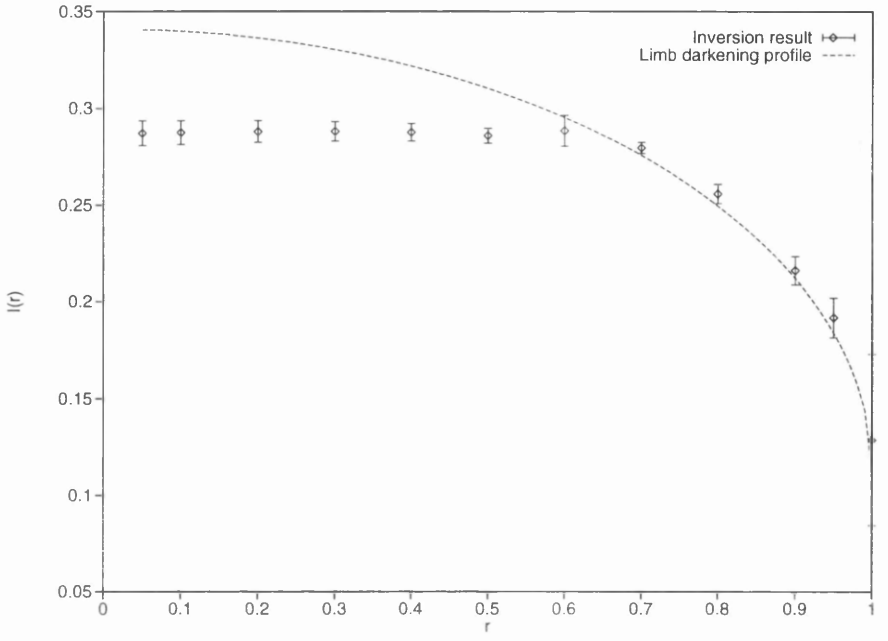

Figure 6.5: Inversion results for limb darkening coefficient $u = 0.67$. 100 data points, $\sigma = 0.02$, impact parameter = Einstein radius = stellar radius. Error bars indicate the standard deviation of the recovered intensity.

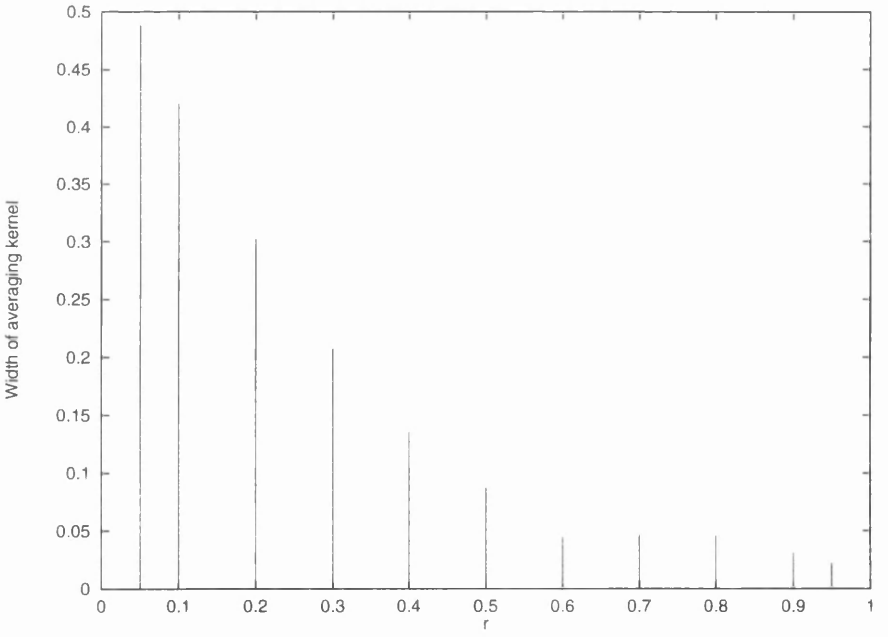

Figure 6.6: The width of the averaging kernel at each point for the $u = 0.67$ inversion, in units of the stellar radius.

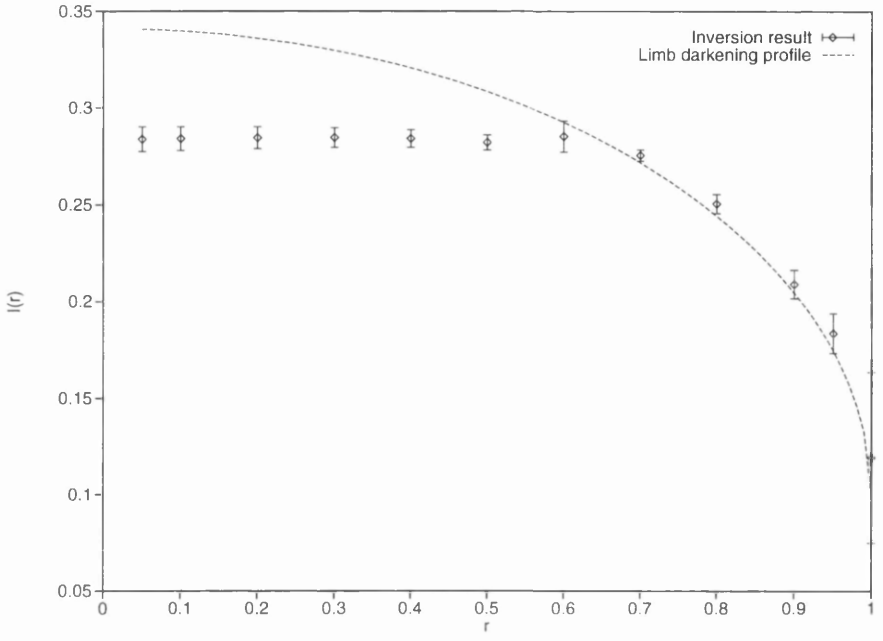

Figure 6.7: Inversion results for limb darkening coefficient $u = 0.71$. 100 data points, $\sigma = 0.02$, impact parameter = Einstein radius = stellar radius. Error bars indicate the standard deviation of the recovered intensity.

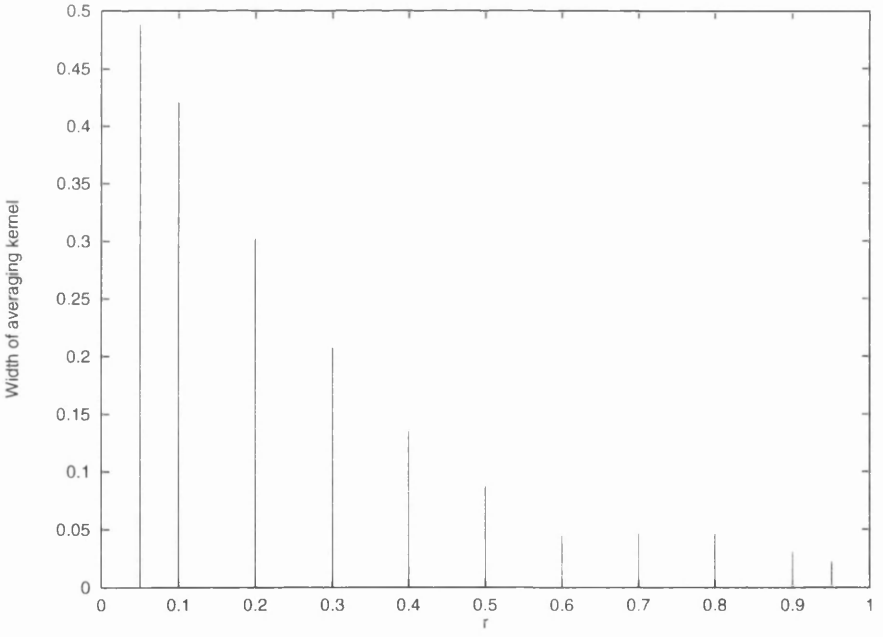

Figure 6.8: The width of the averaging kernel at each point for the $u = 0.71$ inversion, in units of the stellar radius.

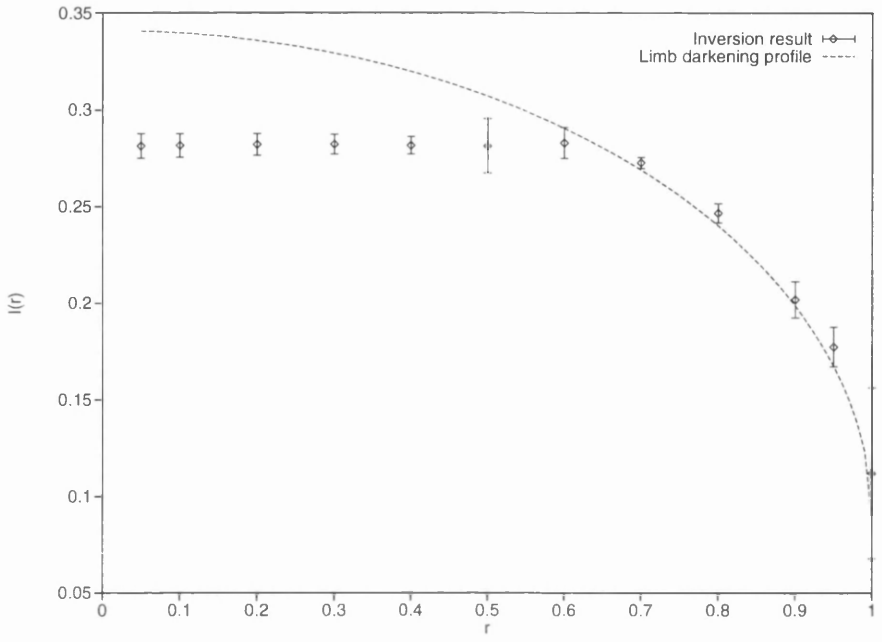

Figure 6.9: Inversion results for limb darkening coefficient $u = 0.74$. 100 data points, $\sigma = 0.02$, impact parameter = Einstein radius = stellar radius. Error bars indicate the standard deviation of the recovered intensity.

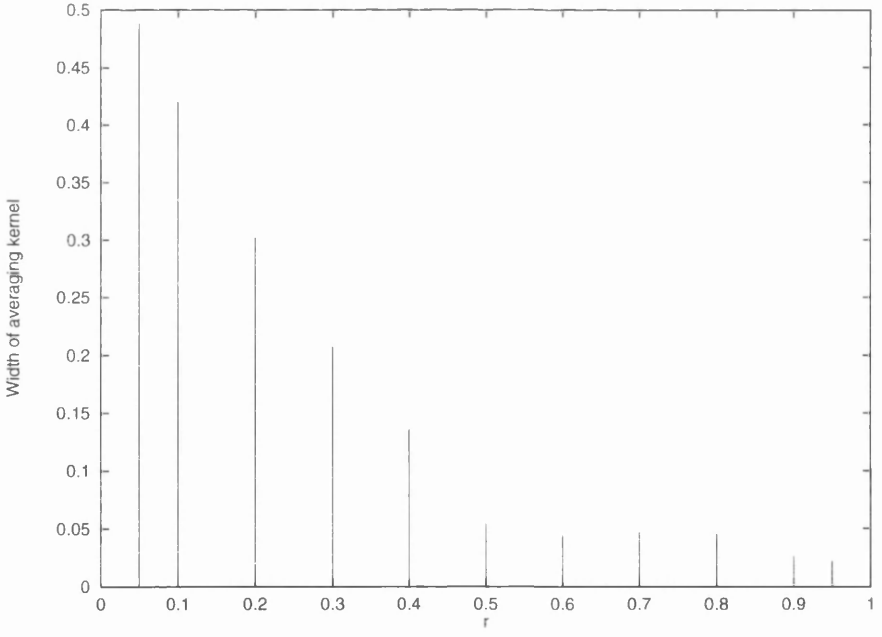

Figure 6.10: The width of the averaging kernel at each point for the $u = 0.74$ inversion, in units of the stellar radius.

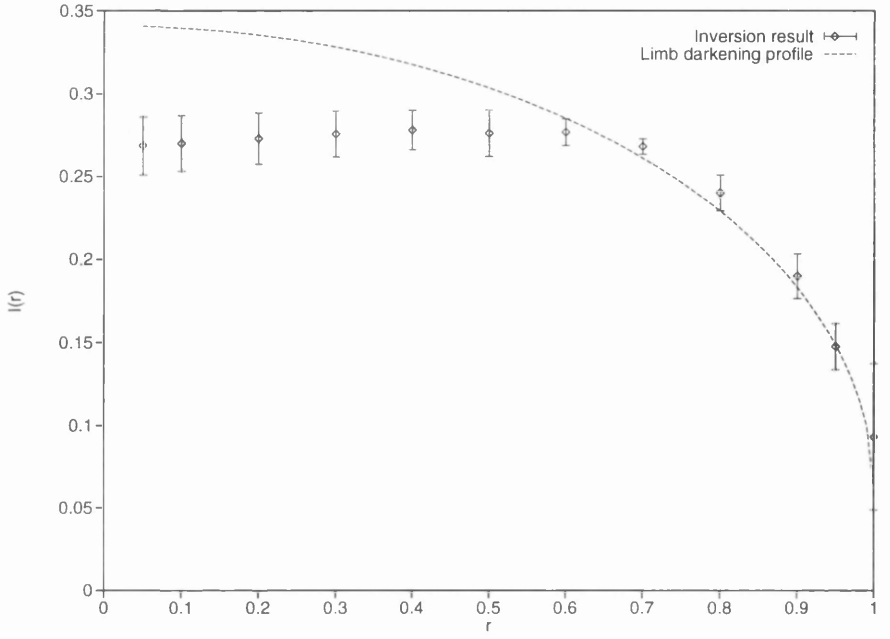

Figure 6.11: Inversion results for limb darkening coefficient $u = 0.82$. 100 data points, $\sigma = 0.02$, impact parameter = Einstein radius = stellar radius. Error bars indicate the standard deviation of the recovered intensity.

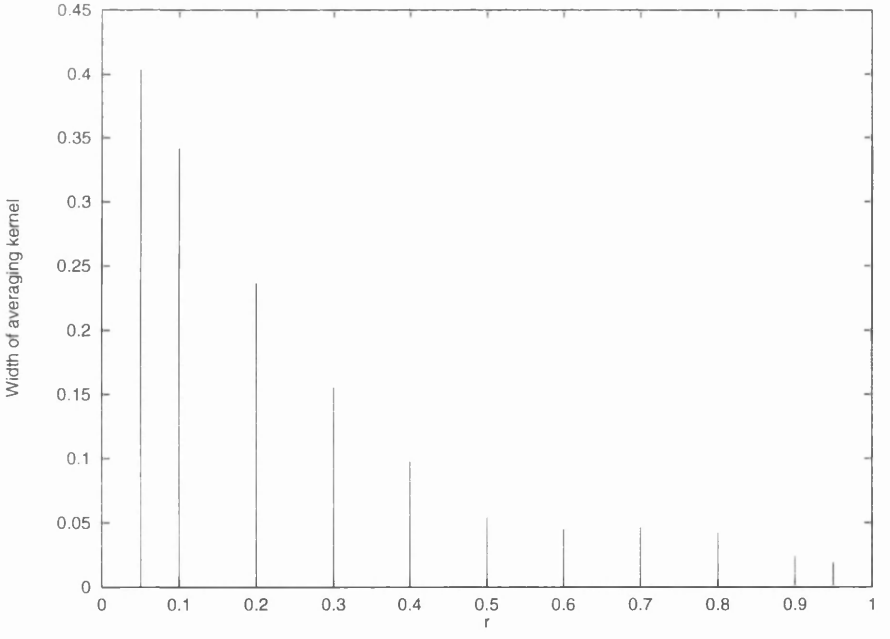

Figure 6.12: The width of the averaging kernel at each point for the $u = 0.82$ inversion, in units of the stellar radius.

6.3.2 Chromaticity

Here the lens and data parameters are the same as in the previous section. Figs. 6.13 to 6.16 present the results for two cases:

1. $T_{eff} = 4000K, \log g = 2.00$
2. $T_{eff} = 6730K, \log g = 4.50$

The "chromaticity profile" $I'(r)$ is the difference in intensity between two wave bands (in this case B and V), i.e. $I'(r) = I_B(r) - I_V(r)$. As before, the limb darkening coefficients for these wavebands are from Claret & Giménez [81].

The remarks about the quality of the limb darkening inversion apply here also, but the stability near the limb is even poorer. The only region that can well-resolved is $0.6 \lesssim r \lesssim 0.8$. This is not really bad news: if one is interested in discriminating between atmospheric models on the basis of their chromaticity, this is typically the region where the model profiles differ the most. Thus, observing chromatic effects in microlensing can produce tangible astrophysical results.

This point is illustrated in Fig. 6.17, which shows the profile and inversion results of Fig. 6.15 alongside a model profile which differs from the true model only in its surface gravity term. The recovered intensity differences at $r = 0.7$ and $r = 0.8$ can clearly distinguish between the rival models.

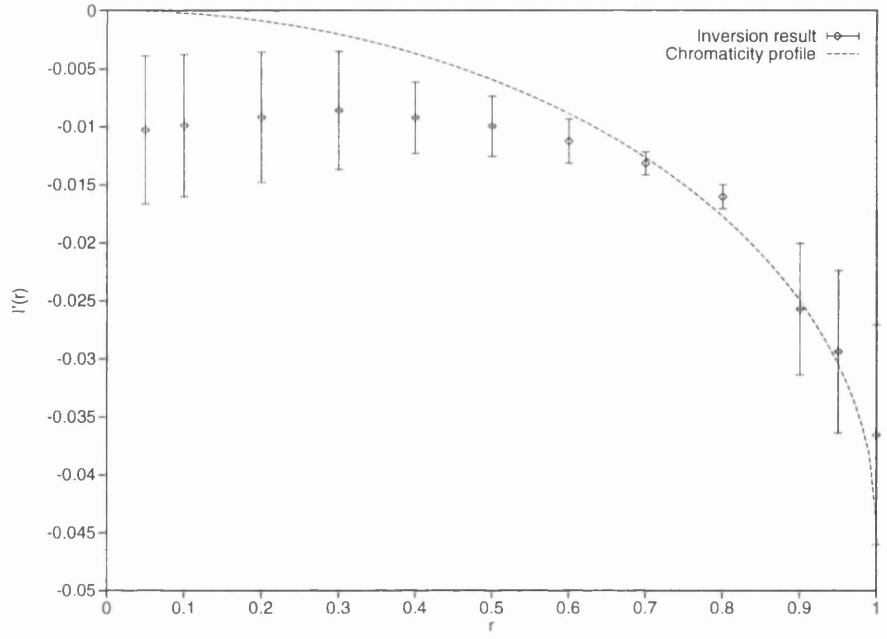

Figure 6.13: Inversion results for limb darkening coefficients $B = 0.76, V = 0.63$. 100 data points, $\sigma = 0.02$, impact parameter = Einstein radius = stellar radius. Error bars indicate the standard deviation of the recovered intensity.

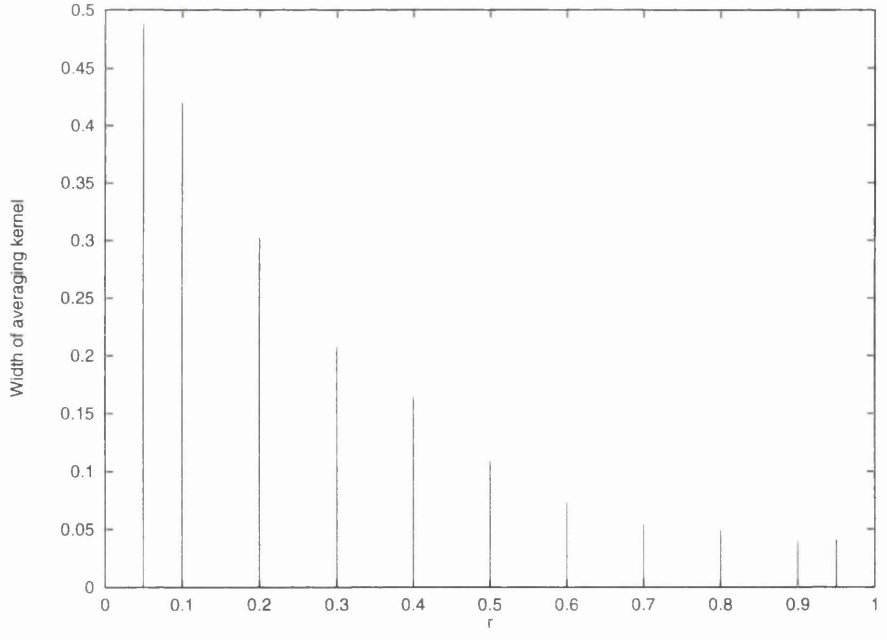

Figure 6.14: The width of the averaging kernel at each point for the $B = 0.76, V = 0.63$ inversion, in units of the stellar radius.

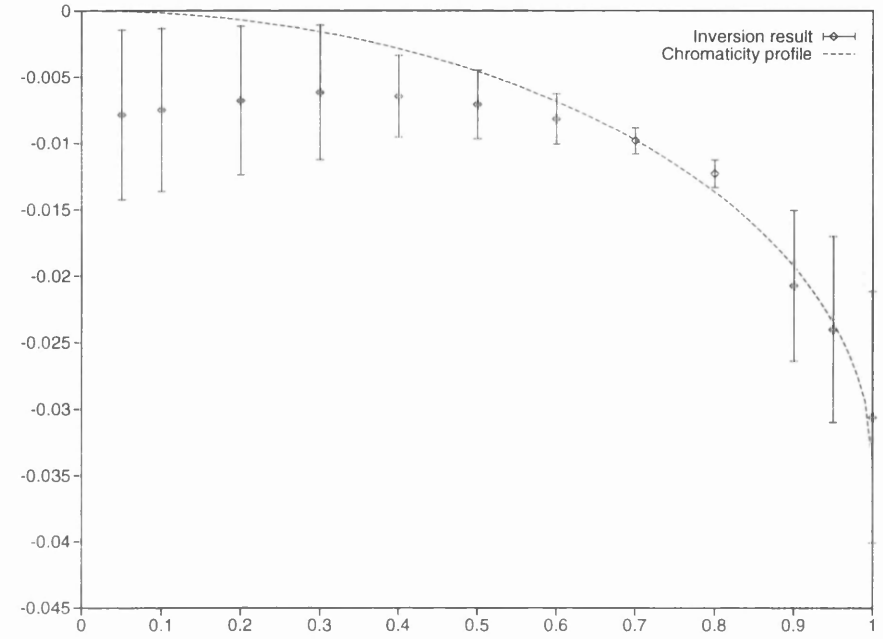

Figure 6.15: Inversion results for limb darkening coefficient $B = 0.92, V = 0.82$. 100 data points, $\sigma = 0.02$, impact parameter = Einstein radius = stellar radius. Error bars indicate the standard deviation of the recovered intensity.

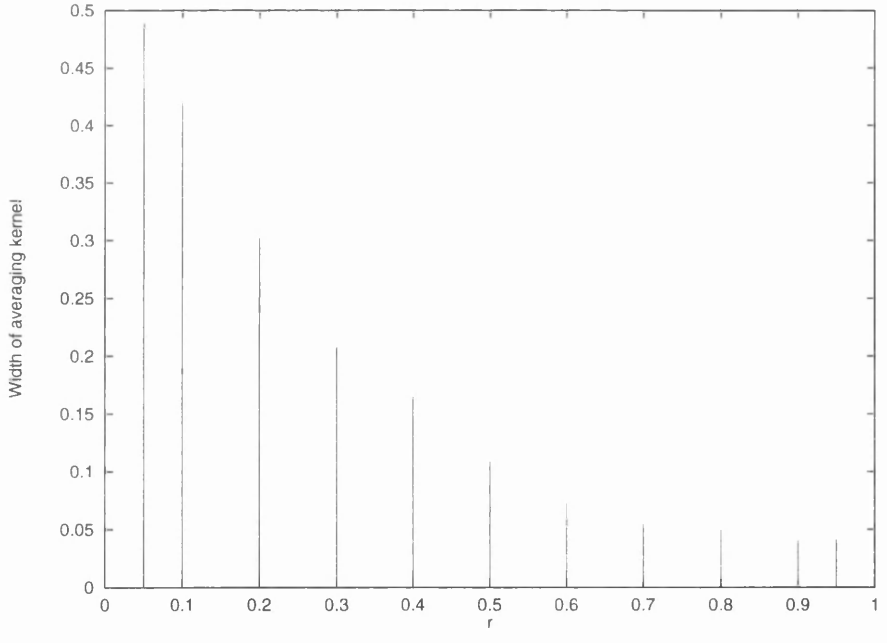

Figure 6.16: The width of the averaging kernel at each point for the $B = 0.92, V = 0.82$ inversion, in units of the stellar radius.

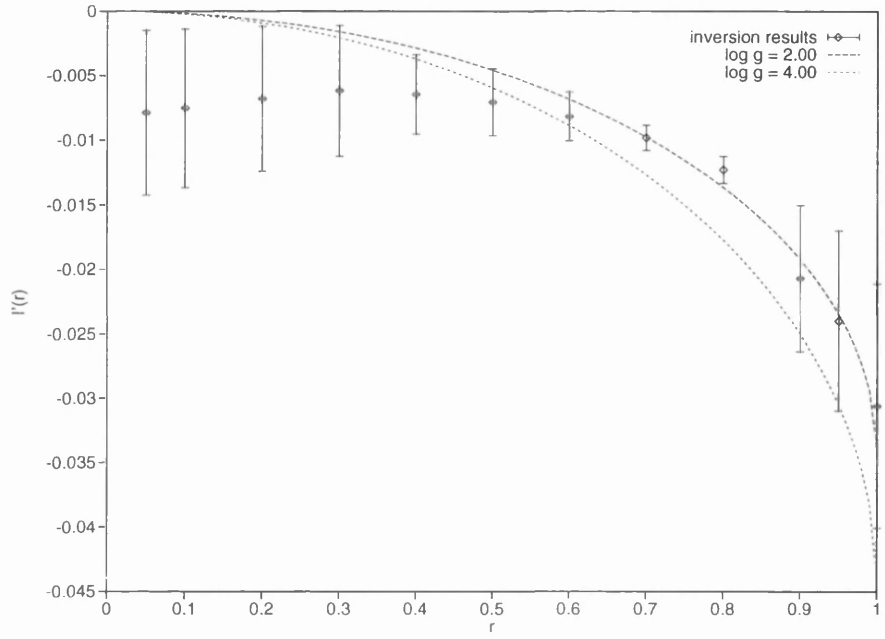

Figure 6.17: Chromaticity profiles for two atmosphere models (both have $T_{eff} = 4000K$), and the inversion results for the case $\log g = 2.00$. 100 data points, $\sigma = 0.02$, impact parameter = Einstein radius = stellar radius. Error bars indicate the standard deviation of the recovered intensity.

6.3.3 Sensitivity to lens parameters

Einstein radius

All the previous simulations have involved a lens with projected Einstein radius ξ equal to the stellar radius R. Figs. 6.18 to 6.21 illustrate the effects of increasing ξ while the other parameters remain unchanged.

Clearly, the increased Einstein radius greatly improves the inversion. Indeed, large Einstein radii allow the region around $r \sim 0.7$ to be recovered with virtually no error or bias. Since, as discussed in Section 3.7, we expect these larger Einstein radii from the survey data, this is excellent news as far as the prospects for microlensing inversion are concerned.

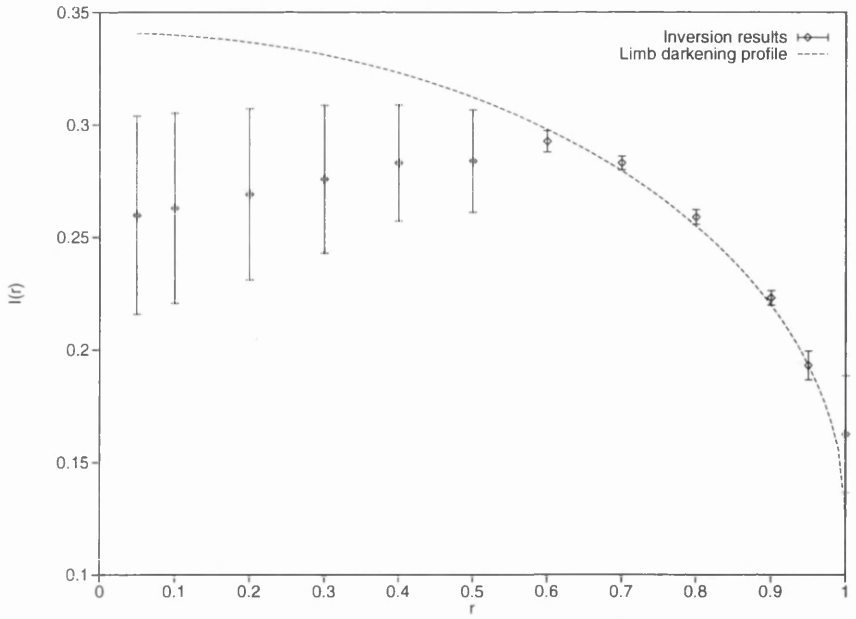

Figure 6.18: Einstein radius $\xi = 4R$, limb darkening coefficient $V = 0.63$. 100 data points, $\sigma = 0.02$, impact parameter = stellar radius. Error bars indicate the standard deviation of the recovered intensity.

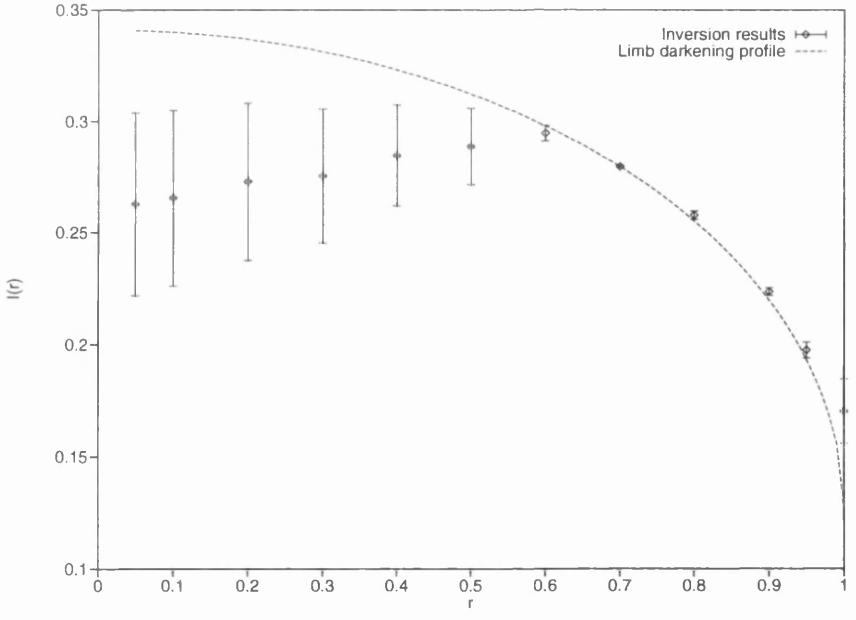

Figure 6.19: Einstein radius $\xi = 8R$, limb darkening coefficient $V = 0.63$. 100 data points, $\sigma = 0.02$, impact parameter = stellar radius. Error bars indicate the standard deviation of the recovered intensity.

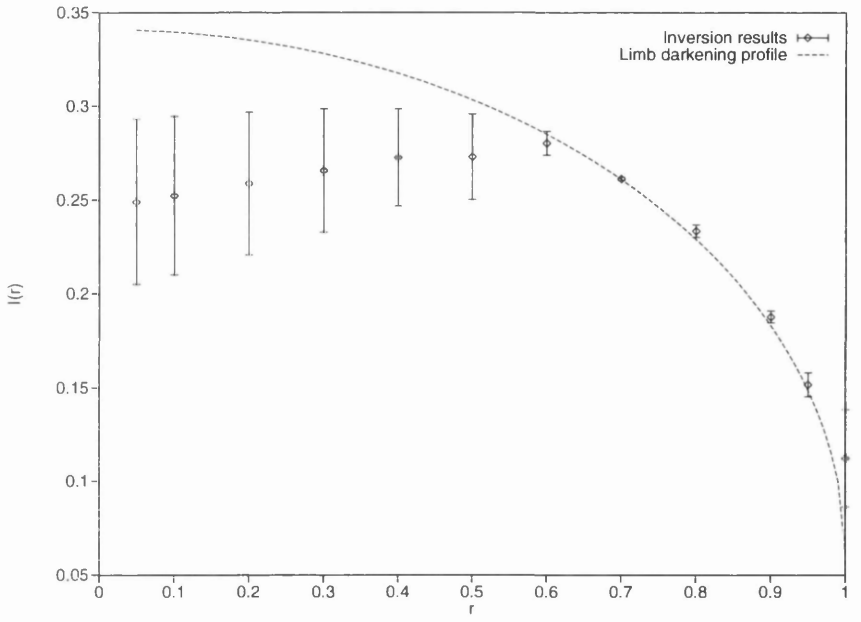

Figure 6.20: Einstein radius $\xi = 4R$, limb darkening coefficient $V = 0.82$. 100 data points, $\sigma = 0.02$, impact parameter = stellar radius. Error bars indicate the standard deviation of the recovered intensity.

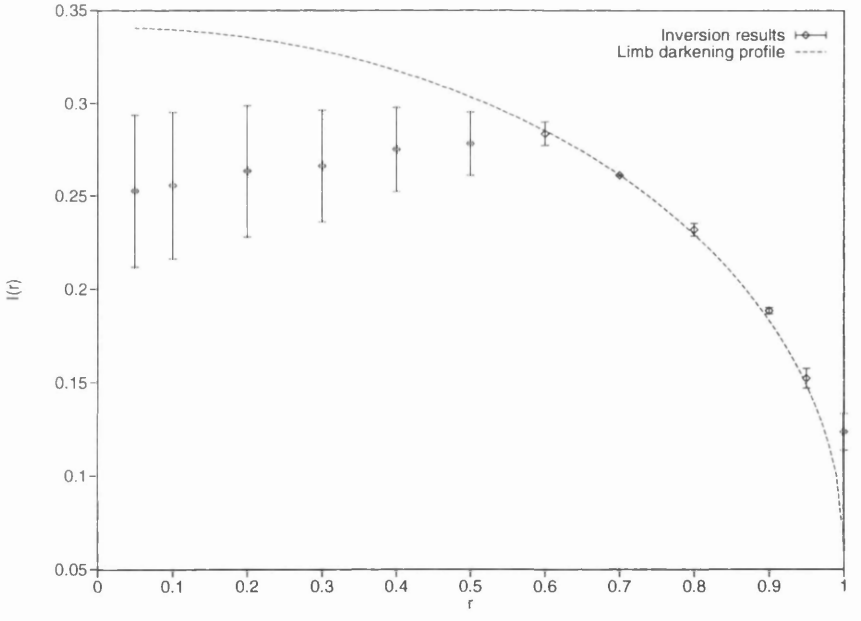

Figure 6.21: Einstein radius $\xi = 8R$, limb darkening coefficient $V = 0.82$. 100 data points, $\sigma = 0.02$, impact parameter = stellar radius. Error bars indicate the standard deviation of the recovered intensity.

Figs. 6.22 to 6.25 illustrate the improved quality of the chromaticity inversions with increased Einstein radius. As with the limb darkening case, the inversions improve dramatically with increased Einstein radius, allowing the chromatic structure to be picked out with great accuracy for $0.6 \lesssim r \lesssim 0.9$.

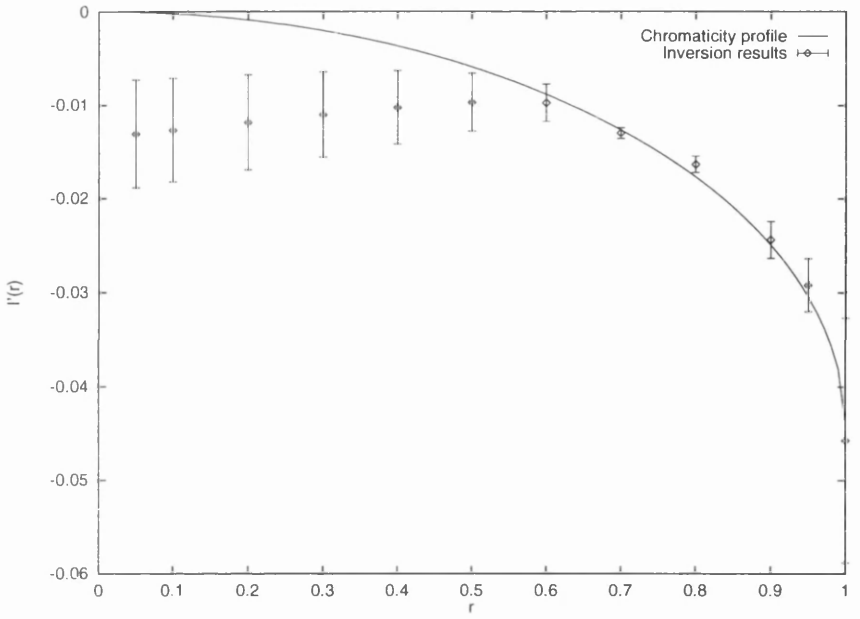

Figure 6.22: Chromaticity inversion for Einstein radius $\xi = 4R$: model parameters $B = 0.76$, $V = 0.63$. 100 data points, $\sigma = 0.02$, impact parameter = stellar radius. Error bars indicate the standard deviation of the recovered intensity.

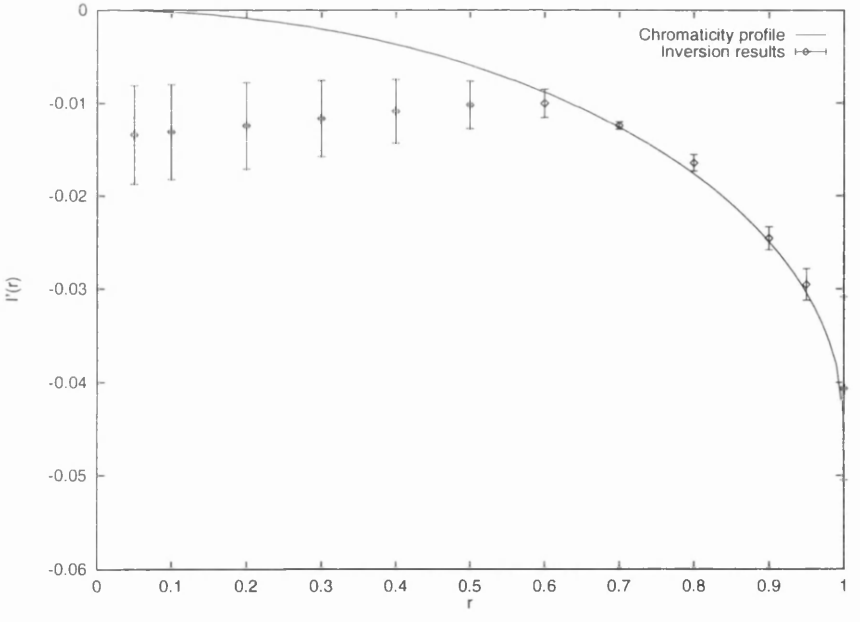

Figure 6.23: Chromaticity inversion for Einstein radius $\xi = 8R$: model parameters $B = 0.76$, $V = 0.63$. 100 data points, $\sigma = 0.02$, impact parameter = stellar radius. Error bars indicate the standard deviation of the recovered intensity.

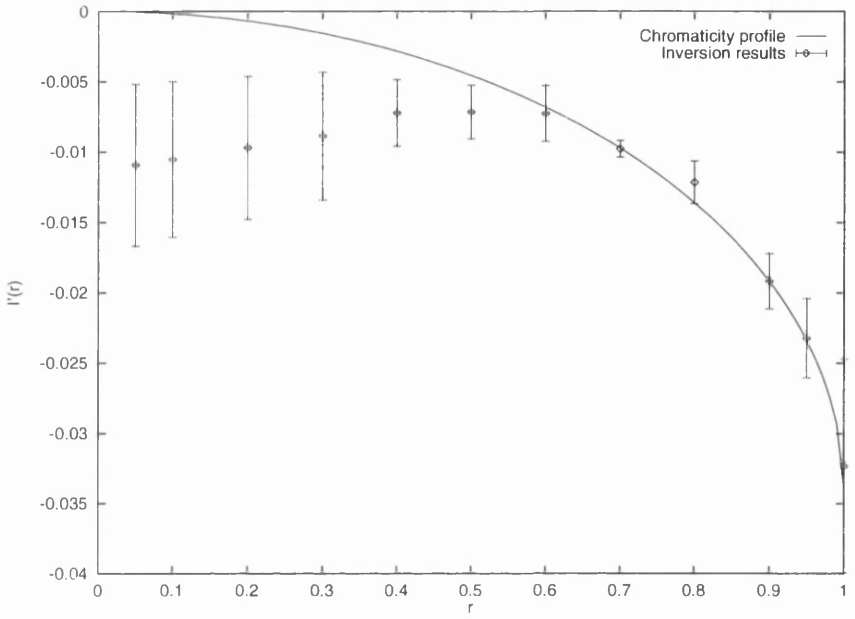

Figure 6.24: Chromaticity inversion for Einstein radius $\xi = 4R$: model parameters $B = 0.92$, $V = 0.82$. 100 data points, $\sigma = 0.02$, impact parameter = stellar radius. Error bars indicate the standard deviation of the recovered intensity.

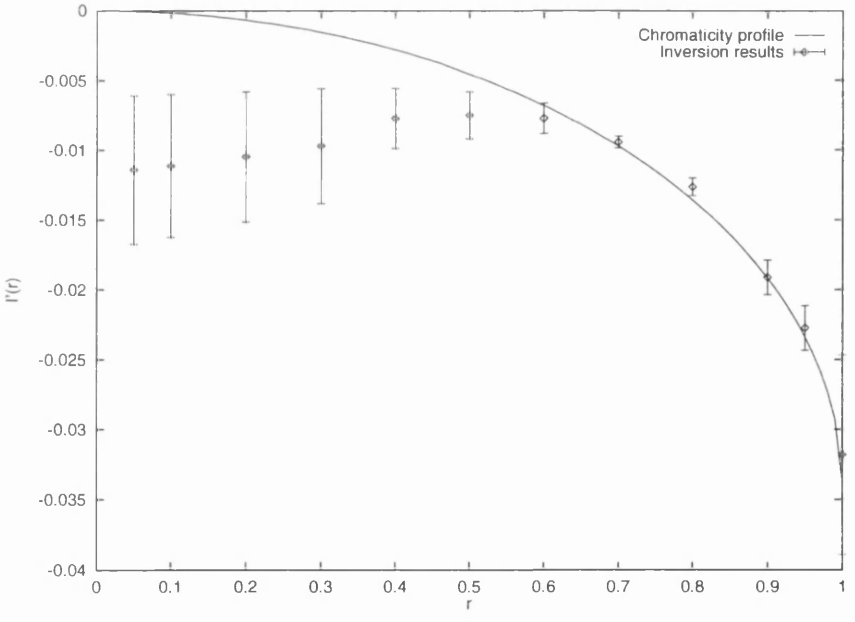

Figure 6.25: Chromaticity inversion for Einstein radius $\xi = 8R$: model parameters $B = 0.92$, $V = 0.82$. 100 data points, $\sigma = 0.02$, impact parameter = stellar radius. Error bars indicate the standard deviation of the recovered intensity.

Impact parameter

The impact parameter has a more dramatic effect. In the case of a transit, when the lens crosses the stellar disk, the intensity profile can be very well constrained. However, as the impact parameter becomes greater than the stellar radius the quality of the inversion quickly deteriorates.

Figs. 6.26 and 6.27 show the case where the impact parameter $b = 0.5R$ (and all other parameters are as in section 6.3.1).Compared to Figs. 6.3 and 6.11, the region $0.6 \lesssim r \gtrsim 0.8$ is much more accurately determined. Some improvement can be seen for $r \lesssim 0.5$, while the limb is a little less well recovered than in the case $b = 1.0$.

The results for larger impact parameters are less promising. Even when b is as small as $2R$ the inversion is rather poor (Figs 6.28 and 6.29), and the recovered profile for $b = 4R$ is indistinguishable from a constant intensity (Figs 6.30 and 6.31). In this case all that is determined is an average intensity across the disk, and the closer the true intensity at a given point is to this average the more accurate is the recovery.

Contrary to the expectations of Section 5.5, then, a transit does seem to be necessary for a lensing event to be usefully invertible.

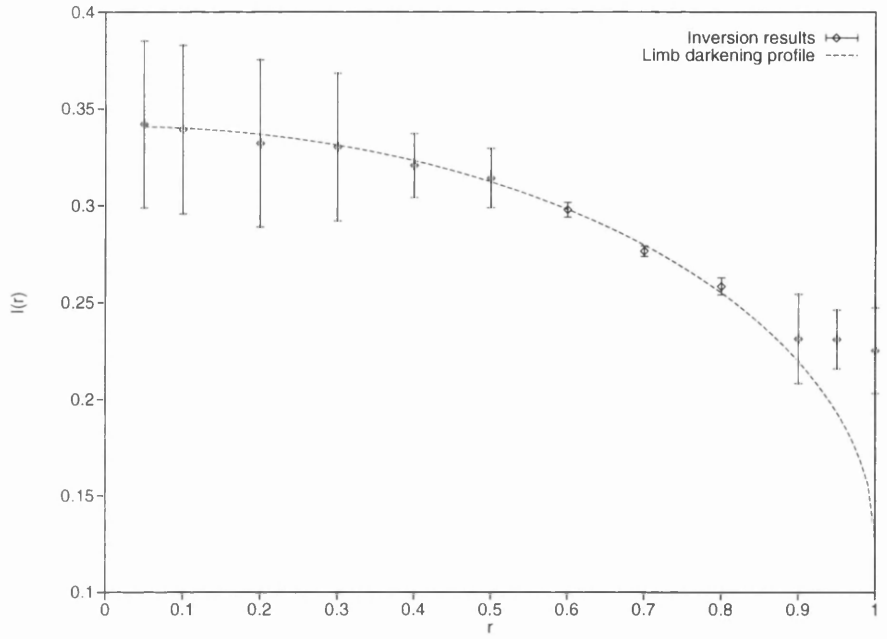

Figure 6.26: Transit: $b = 0.5R$, $V = 0.63$. 100 data points, $\sigma = 0.02$, Einstein radius = stellar radius. Error bars indicate the standard deviation of the recovered intensity.

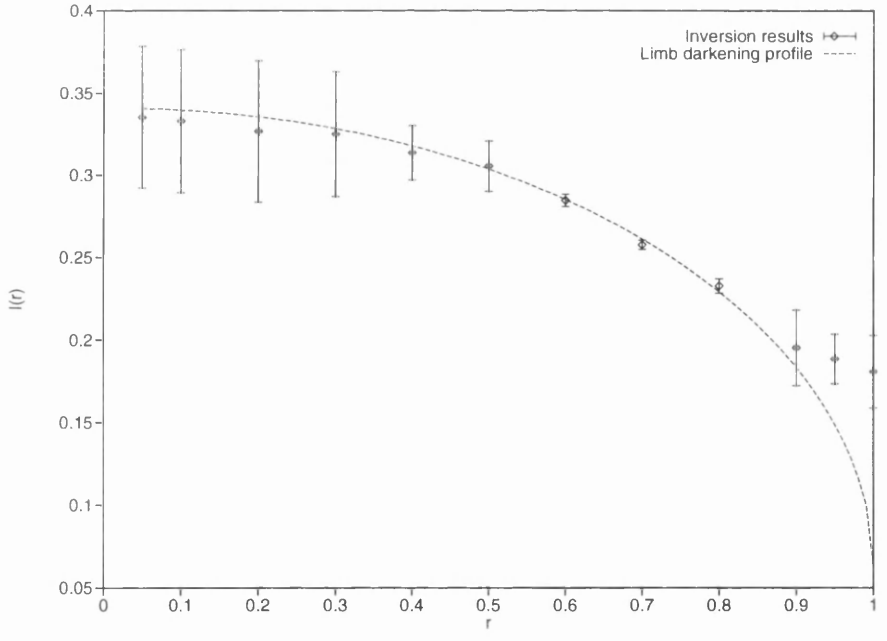

Figure 6.27: Transit: $b = 0.5R$, $V = 0.82$. 100 data points, $\sigma = 0.02$, Einstein radius = stellar radius. Error bars indicate the standard deviation of the recovered intensity.

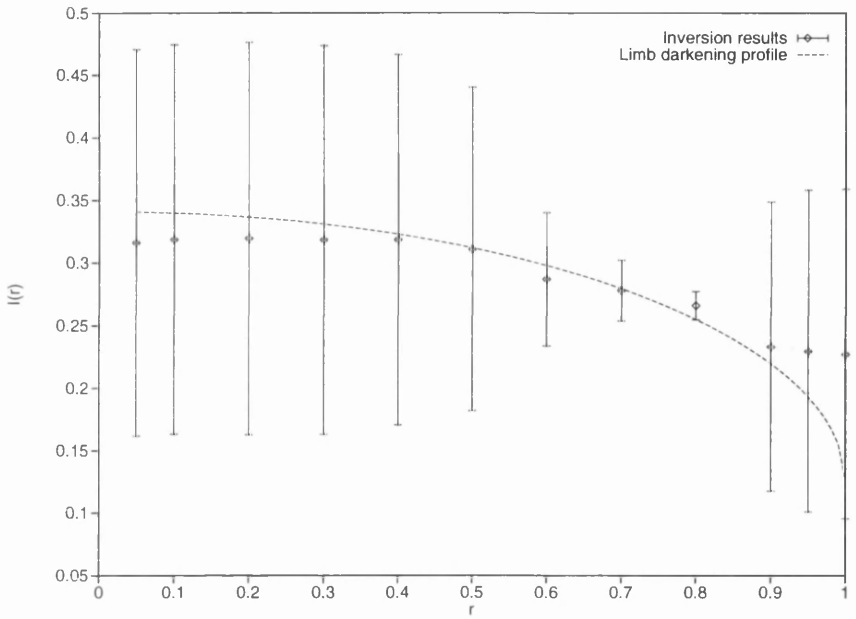

Figure 6.28: Impact parameter $b = 2R$, $V = 0.63$. 100 data points, $\sigma = 0.02$, Einstein radius = stellar radius. Error bars indicate the standard deviation of the recovered intensity.

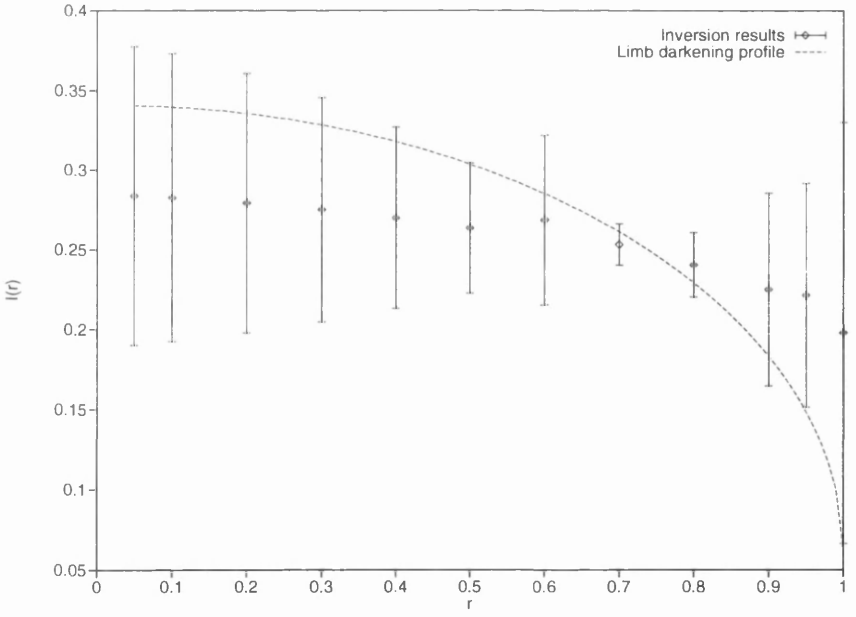

Figure 6.29: Impact parameter $b = 2R$, $V = 0.82$. 100 data points, $\sigma = 0.02$, Einstein radius = stellar radius. Error bars indicate the standard deviation of the recovered intensity.

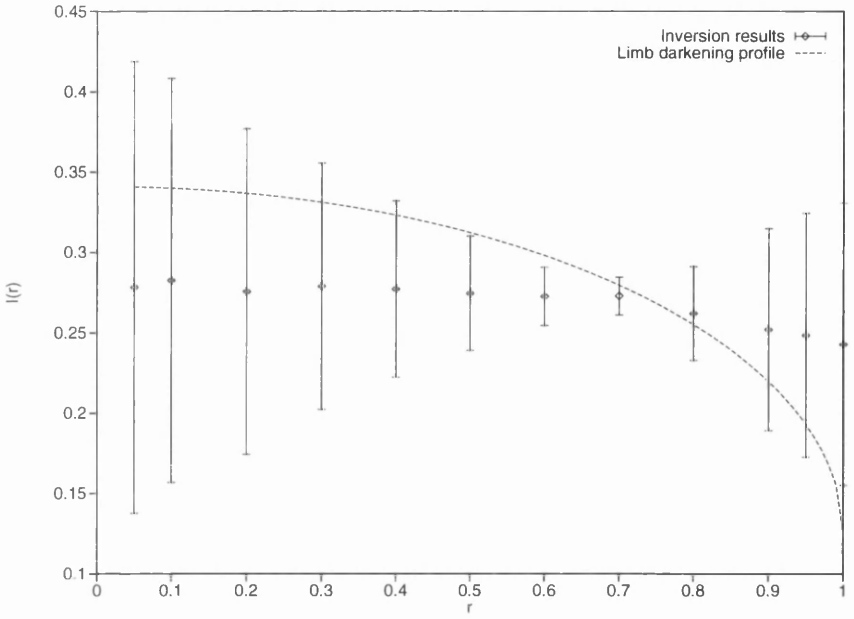

Figure 6.30: Impact parameter $b = 4R$, $V = 0.63$. 100 data points, $\sigma = 0.02$, Einstein radius = stellar radius. Error bars indicate the standard deviation of the recovered intensity.

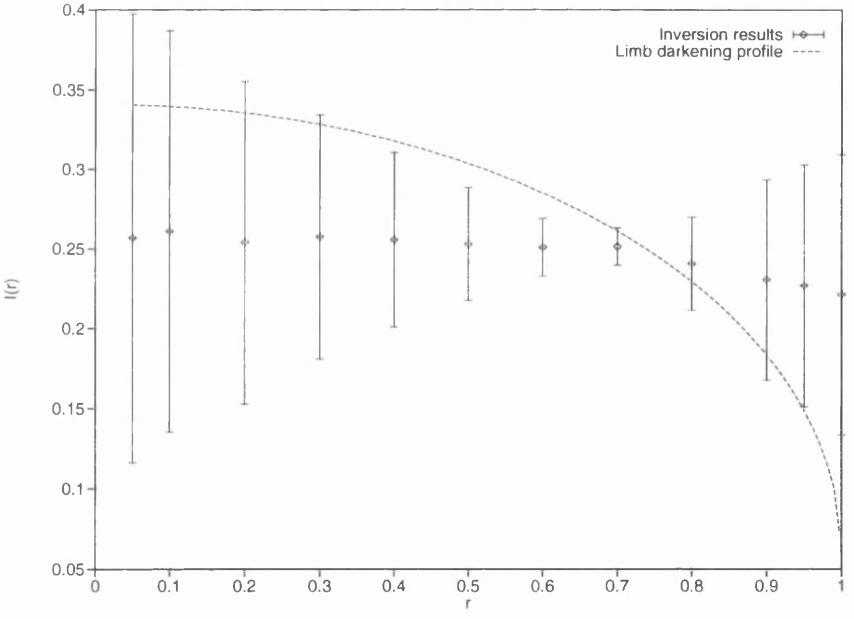

Figure 6.31: Impact parameter $b = 4R$, $V = 0.82$. 100 data points, $\sigma = 0.02$, Einstein radius = stellar radius. Error bars indicate the standard deviation of the recovered intensity.

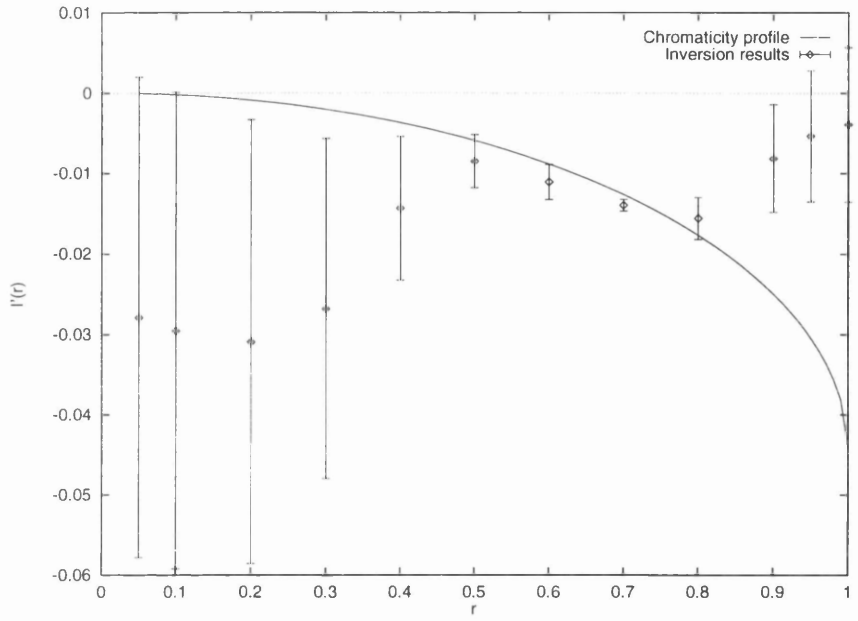

Figure 6.32: $b = 0.5R$, $B = 0.76, V = 0.63$. 100 data points, $\sigma = 0.02$, Einstein radius = stellar radius. Error bars indicate the standard deviation of the recovered intensity.

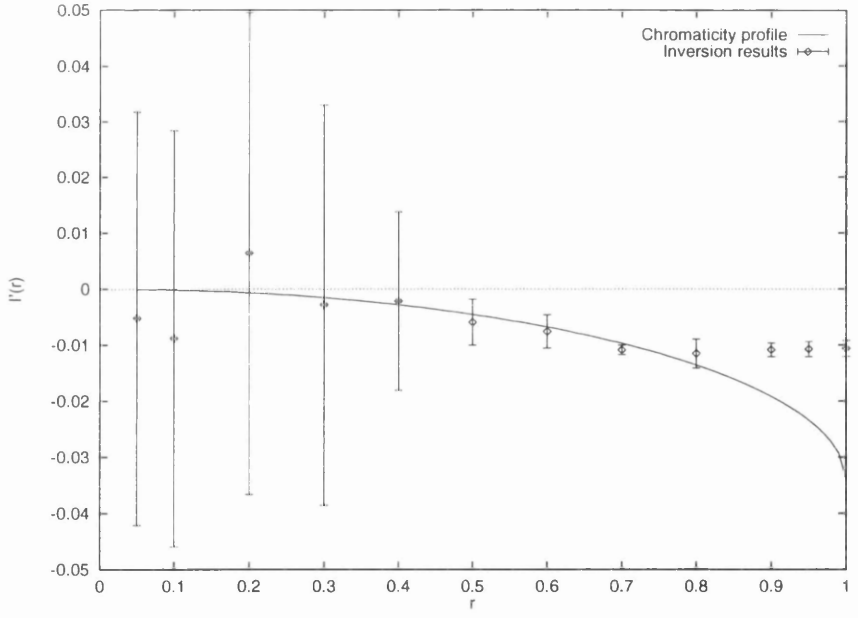

Figure 6.33: $b = 0.5R$, $B = 0.92, V = 0.63$. 100 data points, $\sigma = 0.02$, Einstein radius = stellar radius. Error bars indicate the standard deviation of the recovered intensity.

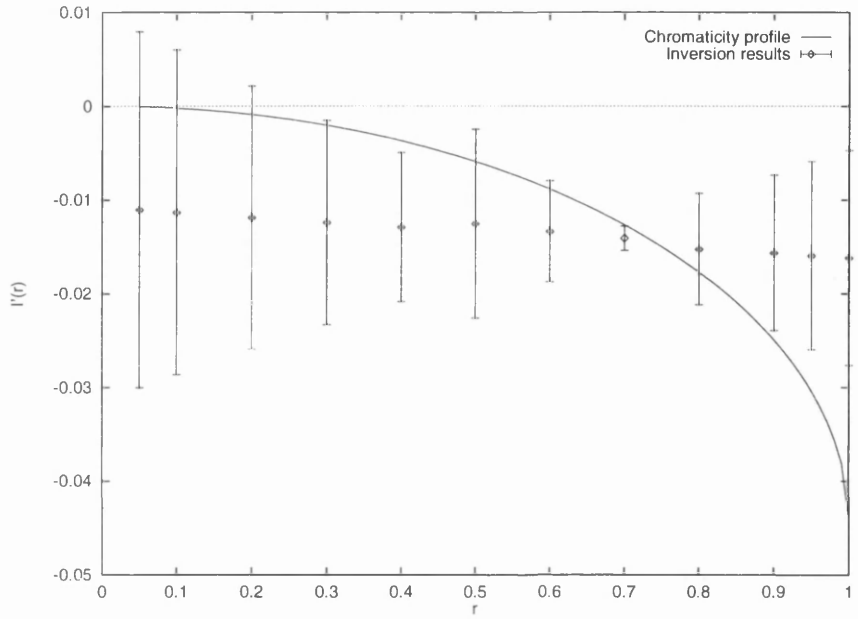

Figure 6.34: Impact parameter $b = 2R$, $B = 0.76, V = 0.63$. 100 data points, $\sigma = 0.02$, Einstein radius = stellar radius. Error bars indicate the standard deviation of the recovered intensity.

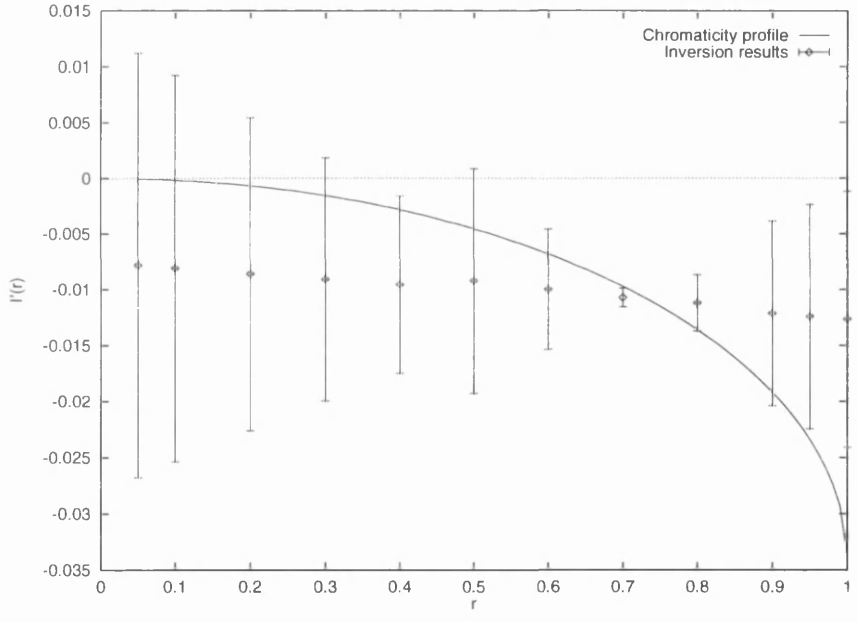

Figure 6.35: Impact parameter $b = 2R$, $B = 0.92, V = 0.82$. 100 data points, $\sigma = 0.02$, Einstein radius = stellar radius. Error bars indicate the standard deviation of the recovered intensity.

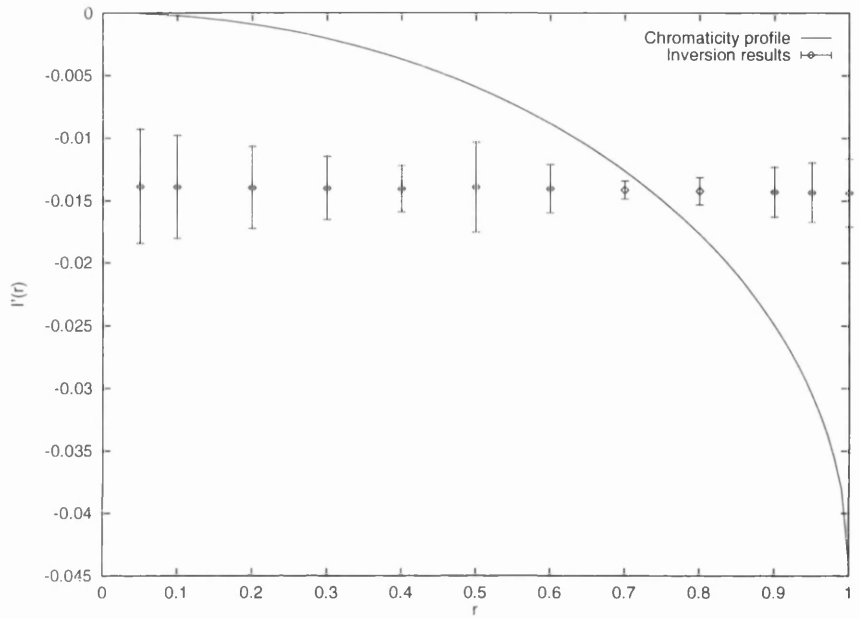

Figure 6.36: Impact parameter $b = 4R$, $B = 0.76, V = 0.63$. 100 data points, $\sigma = 0.02$, Einstein radius = stellar radius. Error bars indicate the standard deviation of the recovered intensity.

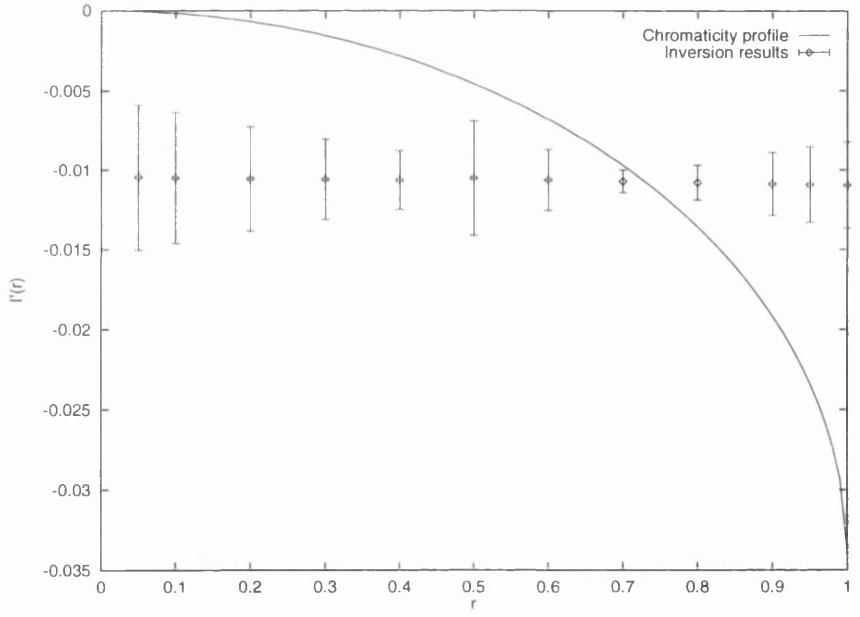

Figure 6.37: Impact parameter $b = 4R$, $B = 0.92, V = 0.82$. 100 data points, $\sigma = 0.02$, Einstein radius = stellar radius. Error bars indicate the standard deviation of the recovered intensity.

6.3.4 Data quality

Having seen how the inversion depends on the lens parameters, we can now experiment with altering the quality of the data. This is the kind of information that is needed to assess the feasibility or otherwise of a given proposal, as well as giving a guide to the best observing strategy, given the available resources.

In the present study, there are two parameters we can alter: the number of data points and the noise level. We consider them in turn.

Number of data points

A very poorly sampled light curve may have as few as 10 data points covering the lensing event. At the other extreme, some recent, long-timescale events have $\sim$ 200 points, and the PLANET collaboration's program of rapid-sampling follow-ups to microlensing alerts aims to achieve this level of coverage on a routine basis.

Figs. 6.38 to 6.40 show the inversion results for light curves with 10, 25, 50 and 200 points (all other parameters are the same as in section 6.3.1). The results are a little surprising.

When there are only 10 points in the data, the resulting inversion is unsurprisingly poor (Fig. 6.38). Going up to 25 points (Fig. 6.39) markedly improves the result, as one would expect. Further increasing the number of data points has a much less dramatic effect, and 200 points are not particularly better than 50.

This means that even short-timescale events can provide a reasonable amount of information, and that further investment in improving the sampling rate is really not necessary for this particular aspect of microlensing.

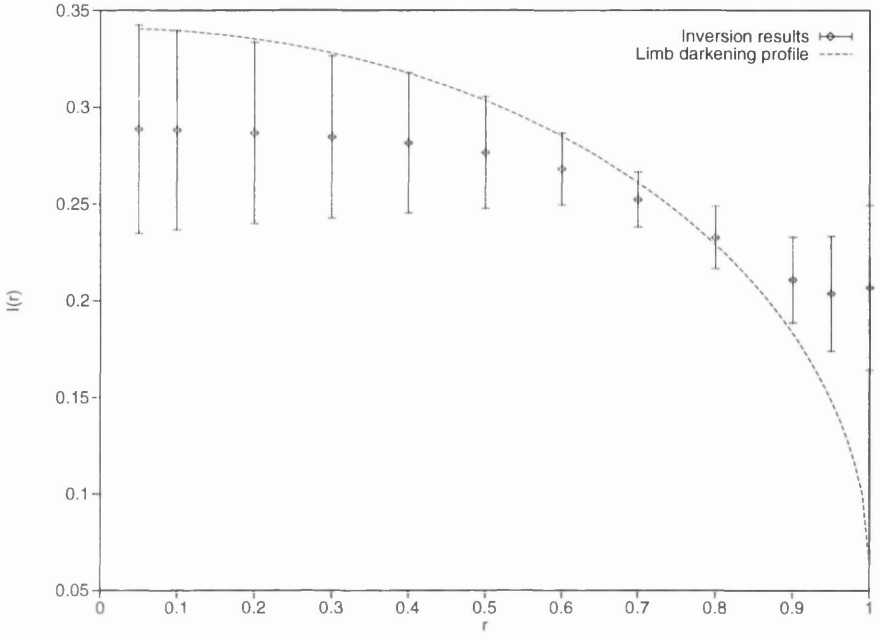

Figure 6.38: $n = 10$. $\sigma = 0.02$, impact parameter = Einstein radius = stellar radius. Error bars indicate the standard deviation of the recovered intensity.

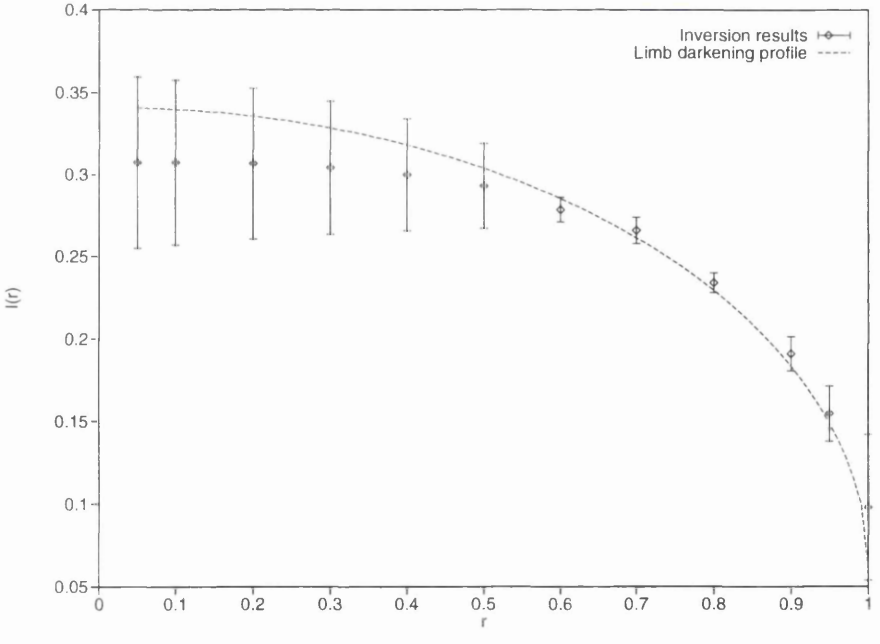

Figure 6.39: $n = 25$. $\sigma = 0.02$, impact parameter = Einstein radius = stellar radius. Error bars indicate the standard deviation of the recovered intensity.

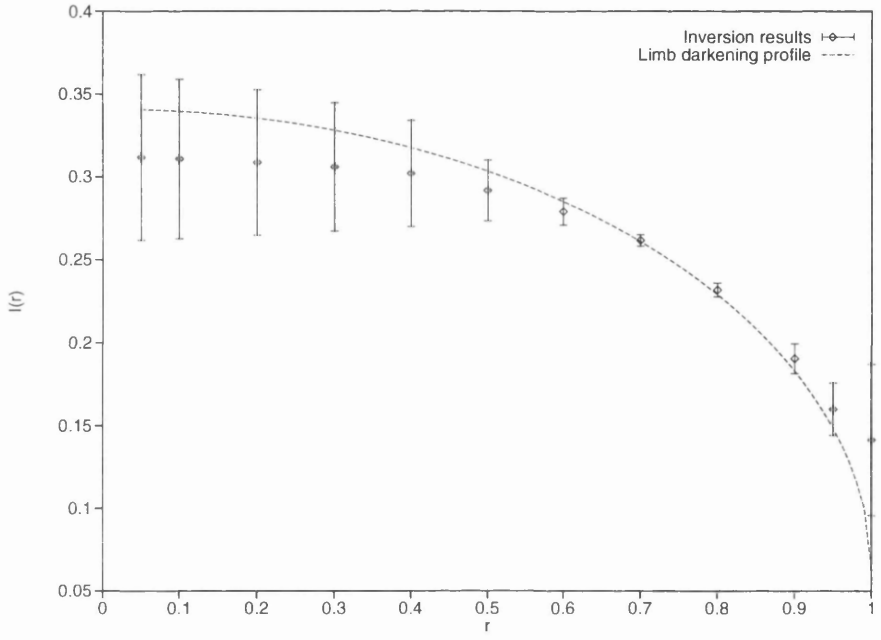

Figure 6.40: $n = 50$. $\sigma = 0.02$, impact parameter = Einstein radius = stellar radius. Error bars indicate the standard deviation of the recovered intensity.

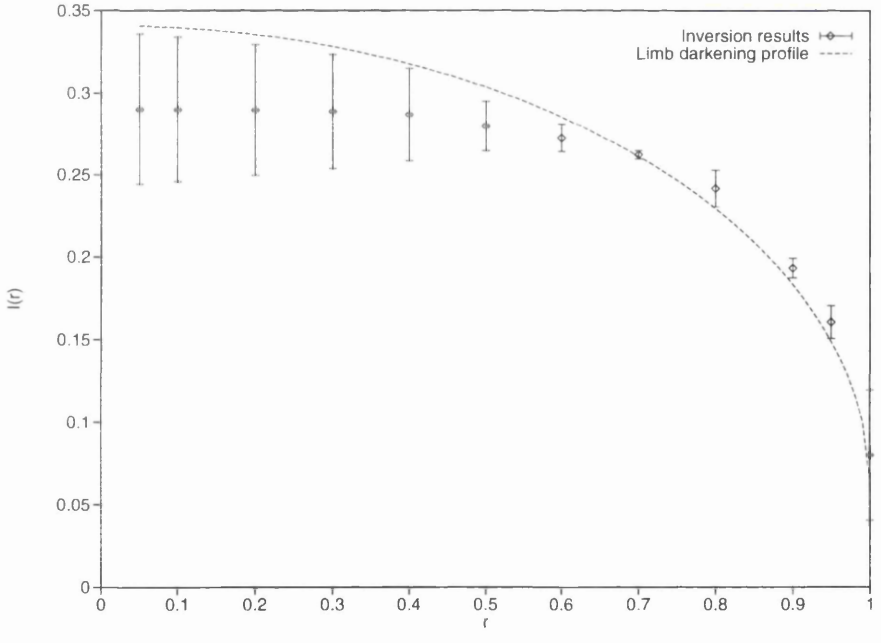

Figure 6.41: $n = 200$. $\sigma = 0.02$, impact parameter = Einstein radius = stellar radius. Error bars indicate the standard deviation of the recovered intensity.

Noise level

Playing around with the noise level can produce some quite instructive effects.

In Fig. 6.42 an inversion has been carried out as in section 6.3.1, but with the noise level reduced by a factor of 10. For $r \gtrsim 0.6$ the results are excellent, and even the limb intensity is relatively close to the mark. When the noise level is greatly increased, to 10% of the baseline flux (5 times the level in section 6.3.1), the results naturally deteriorate. But even in this case of extremely noisy data a meaningful inversion can be obtained, and the recovery compares favourably to Fig. 6.31 for which the data is much less noisy but the impact parameter is greater.

This indicates that the impact of data noise on the inversion is less serious than some of the other effects examined in this chapter, and that some information can be extracted even from very poor data.

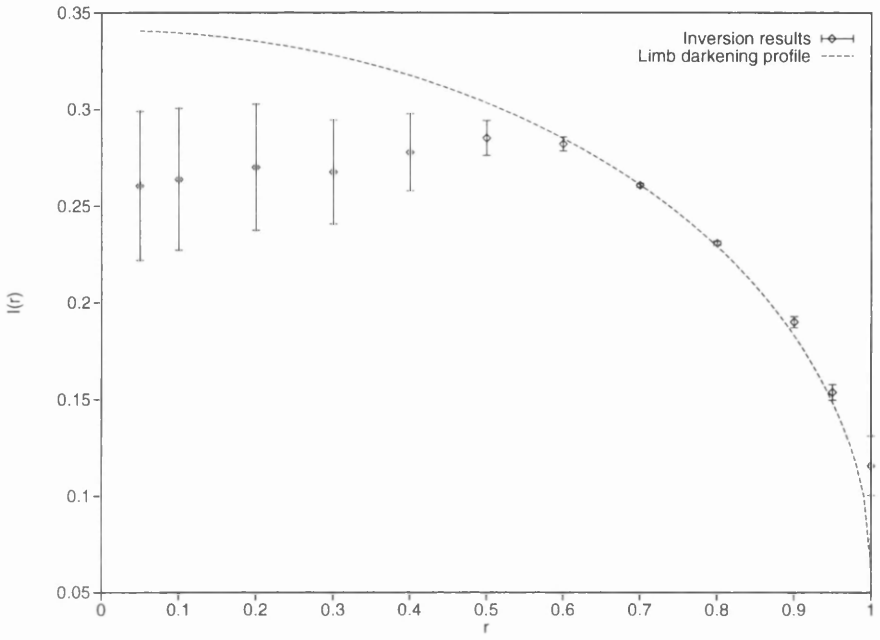

Figure 6.42: $\sigma = 0.002$. 100 data points, impact parameter = Einstein radius = stellar radius. Error bars indicate the standard deviation of the recovered intensity.

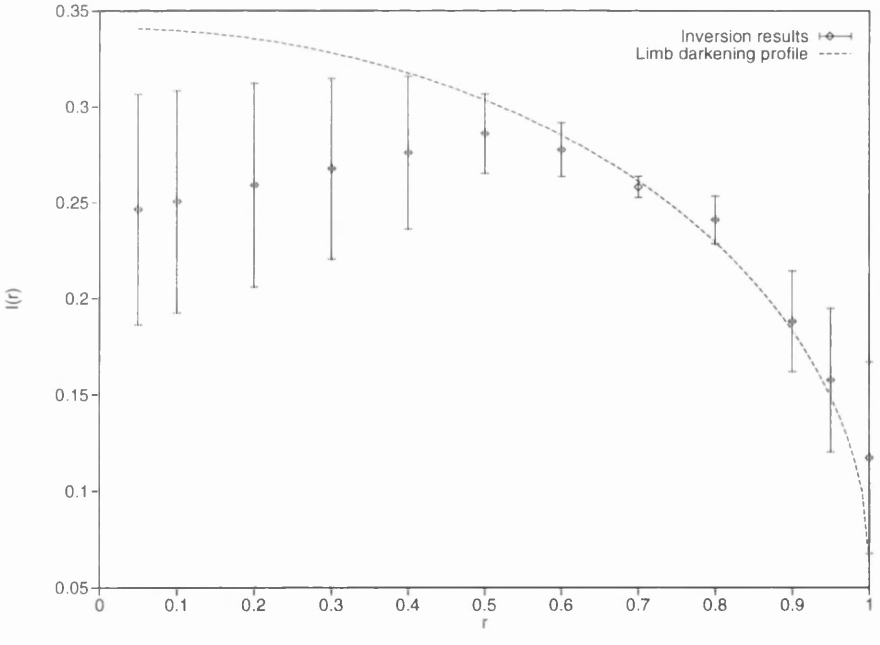

Figure 6.43: $\sigma = 0.1$. 100 data points, impact parameter = Einstein radius = stellar radius. Error bars indicate the standard deviation of the recovered intensity.

6.4 Putting it all together

So what are the implications of this chapter? Well, the most important point is that microlensing *can* resolve intensity and chromaticity profiles across a stellar disk. In particular, the regularised inversion method used in this chapter is able to pick out those regions of the disk which can be well determined from the data, and estimate the value of the profile at those points.

There are two types of parameters involved in this process: those we can control, and those we cannot. The analysis of data quality showed that low-noise data can result in very good profiles, but that having a large number of data points is not really so important. One of the limitations on the number of points is the timescale of the lensing event: we can thus expect to be able to obtain good inversions even from rapid events.

The most important limiting factor is the impact parameter. A transit can give a great deal of information, while events which are only moderately far from being transits are essentially useless. According to [70], somewhat more than half of all observed events will be transits, so we can reasonably anticipate finding useful information in a large fraction of microlensing events.

Comparing these results with the eclipsing inversions in Section 5.5, we see that eclipsing binary light curves provide much more even coverage of the intensity profile. Microlensing can produce far better results at particular regions of the disk, at the cost of poorer recovery elsewhere. However, the regions best resolved by microlensing are the most astrophysically interesting parts of the stellar disk, so this tradeoff is well worthwhile.

In conclusion, then, microlensing can provide a powerful probe of stellar atmospheres, independent of any atmospheric model. The prospects for this kind of analysis are excellent, and with the current interest in microlensing surveys we can look forward to new insights into stellar astrophysics from this novel tool.

The gnostics believed that the material universe is the flawed creation of an insane deity. I have always thought such a creator must have been cackling maniacally at astronomers

when it filled most of the cosmos with dark matter. Well, we can still have the last laugh.

Chapter 7

Future Prospects

> One of these days I'm gonna get in shape, become an astronaut
> One of these days my fears are gonna fall down the stairs
> One of these days I'll sell my soul and let 'em find out what they bought
> One of these days I'm gonna shave off all my hair
>
> Cop Shoot Cop, "Any Day Now"

When I began this project nearly three years ago, extended source effects in microlensing had only just started to be considered. The field has filled out a little since then, but huge regions remain to be explored. Throughout this thesis, I have consistently aimed for simplicity in the underlying models, so as to more clearly bring out the effects of interest.

There are many ways to fill in the framework presented in this thesis, and to extend it to cases of greater complexity. Take the modelling in Chapters 2 and 3 for example. The basic idea is simply to model a particular object, pass a lens in front of it and integrate up the amplification function across the source to obtain a light curve. Obviously, one could extend this to a wide variety of objects such as discs or jets, and could perform the calculations for optically thick atmospheres, stars with spots and other surface features,

and so on. Galactic radio jets in particular may show dramatic, and potentially resolvable, polarimetric variability when lensed.

A more ambitious step would be to simulate microlensing by several masses simultaneously. This is not just a linear combination of single lens cases: multiple lenses give rise to an amplification function with complicated structures of cusps. This is of some relevance to stellar microlensing, where at least one binary lens has been detected, but is more important at cosmological scales where quasars may be microlensed by many objects simultaneously. Calculating the amplification function in this case becomes a major computational task, but otherwise the approach is exactly the same as in this thesis, for both the photometric and polarimetric variability. This could settle the issue of quasar microlensing, by predicting an associated characteristic polarimetric behaviour.

As far as the inversion work is concerned, the most immediate next step is to extend the 1-D approach to the polarized light curve. This could be done along the same lines as the photometric inversions in Chapter 6, although the mathematics involved in integrating the kernel is nontrivial. The other major development will be inverting data from a 2-D source, a star with spots, for example. Spectral line inversions are another fruitful area where microlensing could provide a powerful diagnostic of stellar structure. The real goal, of course, is to apply this theoretical work to real data. As both the quantity and quality of recorded events improve, so too do the prospects for inversions.

Even as I write this, much of the above work has been started. We can look forward to fresh astrophysical insights from microlensing for a long time to come.

Appendix A

A guide to polarimetric jargon

The word "polarization" refers to the orientation of the direction of vibration of a classical wave with respect to some axis. In astronomy, the polarization of radiation carries information about asymmetries in the emitting object (or in the interstellar medium through which the radiation propagates). The two most important polarizing processes are scattering (which gives rise to linear polarization) and magnetic fields (resulting in circular polarization through the Zeeman effect). This thesis only considers scattering processes.

The most useful (though hardly the most intuitive) representation of polarized light is in terms of four intensities: the Stokes parameters. An excellent and thorough discussion of this formulation can be found in Clarke & Grainger [82], and Swihart [51] has a terser discussion: this section will focus only on those points which are necessary for the rest of the thesis.

Consider a plane electromagnetic wave travelling in the $\hat{\mathbf{z}}$ direction. The electric vector at a point z and a time t can be expressed in terms of two orthogonal components in the $\hat{\mathbf{x}}$ and $\hat{\mathbf{y}}$ directions as

$$\mathbf{E} = E_x \cos(\omega t - kz + \delta_x)\hat{\mathbf{x}} + E_y \cos(\omega t - kz + \delta_y)\hat{\mathbf{y}} \tag{A.1}$$

where E_x and E_y are the amplitudes of the $x-$ and $y-$ components, δ_x and δ_y are the phases at $z = 0$, ω is the angular frequency and k is the wave number.

In general, the electric vector will trace out an ellipse through time in the $x - y$ plane. There are three important special cases:

1. *Linear* polarization, when the phase difference $\delta_x - \delta_y = 0$.
2. *Circular* polarization, when the phase difference is $\pm\pi/2$.
3. *Unpolarized* radiation, when $E_x = E_y$ and the phases δ_x and δ_y vary randomly.

A combination of polarized and unpolarized radiation (the usual case in practice) is termed *partial* polarization.

Four parameters are required to completely describe the ellipse. In Eqn. (A.1) these are E_x, E_y, δ_x and δ_y. It is more convenient to combine these quantities into the *Stokes parameters*, given by

$$I = \left\langle E_x^2 + E_y^2 \right\rangle \tag{A.2}$$

$$Q = \left\langle E_x^2 - E_y^2 \right\rangle \tag{A.3}$$

$$U = \langle 2E_x E_y \cos(\delta_y - \delta_x) \rangle \tag{A.4}$$

$$V = \langle 2E_x E_y \sin(\delta_y - \delta_x) \rangle \tag{A.5}$$

Physically, I represents the total intensity of the radiation, Q is the difference in intensity of the x and y components of the electric vector, U is the intensity difference between orthogonal components of the electric vector along axes at an angle of 45° to the x and y axes and V is the difference in intensity between the left and right circularly polarized components. Circular polarization is not discussed in this thesis, and henceforth only I, Q and U will be considered.

In stellar astronomy we are usually concerned with the net polarization from an unresolved source. The total Stokes parameters are simply obtained by adding together the parameters at each element of the source, taking care to refer all the parameters to a single coordinate frame. In the limit this becomes

$$I_{tot} = \int_{source} I \tag{A.6}$$

$$Q_{tot} = \int_{source} Q' \tag{A.7}$$

$$U_{tot} = \int_{source} U' \tag{A.8}$$

where

$$Q' = Q\cos 2\theta + U\sin 2\theta \tag{A.9}$$

$$U' = -Q\sin 2\theta + U\cos 2\theta \tag{A.10}$$

and θ is the rotation angle between the source element frame and the observation frame.

Polarization is often described by the *degree* of polarization P and the *direction* of polarization ψ. In terms of the Stokes parameters, these are

$$P = \frac{\sqrt{Q^2 + U^2}}{I} \tag{A.11}$$

$$\psi = \frac{1}{2}\arctan\frac{U}{Q} \tag{A.12}$$

The above discussion has dealt only with purely polarized radiation, that is, radiation which can be resolved into two coherent orthogonal components. Usually the ray also

contains a component of unpolarized light. This provides an additional contribution to I, so that $I_{tot} = I + I_{unpolarized}$, while not affecting the other Stokes parameters. Eqn. (A.11) shows that such an admixture of unpolarized radiation reduces the degree of polarization, but clearly the direction is unchanged (Eqn. (A.12)). This "dilution" of the polarization plays an important role in this thesis.

Appendix B

The microlensing kernels

Here we derive the kernels for the microlensing inversion, as used in Chapter 6.

The amplification function is

$$A(r,\theta,s) = \frac{1}{2}\left[\left(1+\frac{4}{\zeta^2}\right)^{\frac{1}{2}} + \left(1+\frac{4}{\zeta^2}\right)^{-\frac{1}{2}}\right]$$

where

$$\zeta = r^2 + s^2 - 2rs\cos\theta$$

Put

$$z = e^{i\theta}, \quad \mathrm{d}z = iz\,\mathrm{d}\theta, \quad \cos\theta = \frac{1}{2}\left(z+\frac{1}{z}\right)$$

This gives

$$\zeta^2 = rs\left(\frac{r^2+s^2}{rs} - \left(z+\frac{1}{z}\right)\right)$$

yielding

$$1 + \frac{4}{\zeta^2} = \frac{\zeta^2 + 4}{\zeta^2} = \frac{z^2 - \frac{4+r^2+s^2}{rs}z + 1}{z^2 - \frac{r^2+s^2}{rs}z + 1}$$

This allows us to calculate $\tilde{A}(r,s) = \int_0^{2\pi} A(r,\theta,s) r \, d\theta$ in the following way. Let I be a contour integral in the complex plane, such that

$$I = -\frac{i}{2} \oint \frac{1}{z} \left[\left(\frac{(z-x_2)(z-\bar{x}_2)}{(z-x_1)(z-\bar{x}_1)} \right)^{\frac{1}{2}} + \left(\frac{(z-x_2)(z-\bar{x}_2)}{(z-x_1)(z-\bar{x}_1)} \right)^{\frac{-1}{2}} \right] \mathrm{d}z \qquad \text{(B.1)}$$

where

$$x_1 = a_1 + \sqrt{a_1^2 - 1}$$

$$x_2 = a_2 + \sqrt{a_2^2 - 1}$$

$$\bar{x}_1 \equiv \frac{1}{x_1}$$

$$\bar{x}_2 \equiv \frac{1}{x_2}$$

$$a_1 = \frac{r^2 + s^2}{2rs}$$

$$a_2 = \frac{4 + r^2 + s^2}{2rs}$$

Note that $1 < x_1 < x_2$

There is one pole inside the contour, at $z = 0$.

$$\mathrm{Res}(z = 0) = \frac{i}{2}(1 + 1) = i \qquad \text{(B.2)}$$

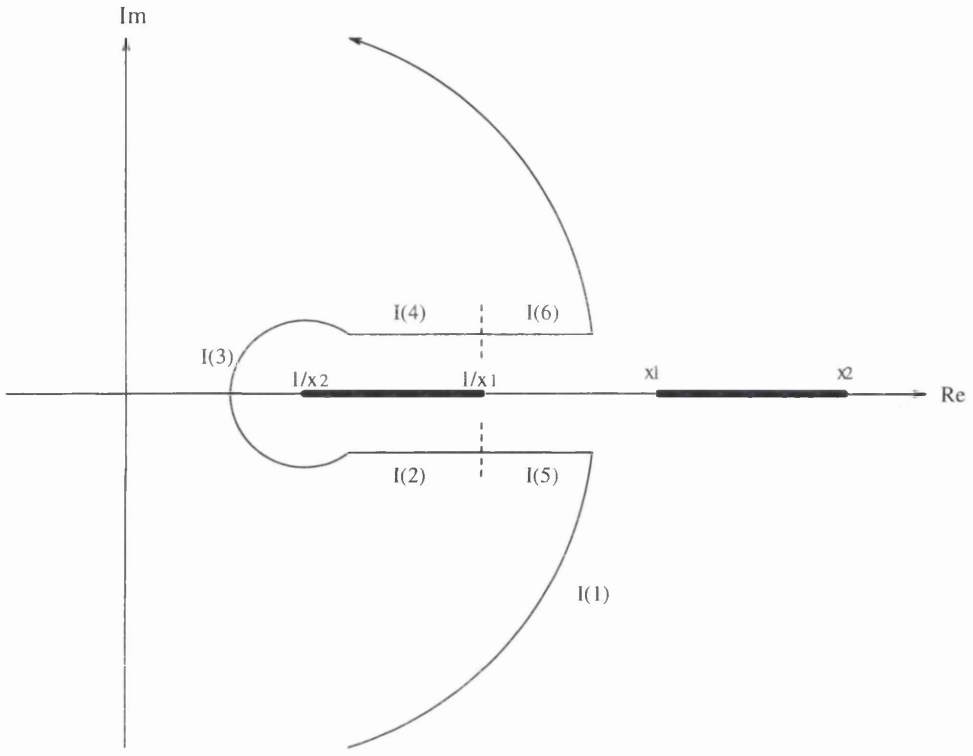

Figure B.1: A section of the contour. Note the cuts between x_1 and x_2, and between $\bar{x}_1$ and $\bar{x}_2$.

giving

$$I = 2\pi i(-i) = 2\pi \tag{B.3}$$

Now, we can also write

$$I = I_1 + I_2 + I_3 + I_4 + I_5 + I_6 \tag{B.4}$$

(see Fig. B.1) where

$I_1 = \tilde{A}/r$

$I_2 : z = \bar{x}_2 + \exp(2\pi i)\sigma,\ \sigma = (\bar{x}_1 - \bar{x}_2) \rightarrow 0,\ \mathrm{d}z = \exp(2\pi i)\mathrm{d}\sigma$

$I_3 : z = \bar{x}_2 + \rho\exp(i\theta),\ \theta = 2\pi \rightarrow 0,\ \mathrm{d}z = i\rho\exp(i\theta)\mathrm{d}\theta$

$I_4 : z = \bar{x}_2 + \sigma,\ \sigma = 0 \rightarrow (\bar{x}_1 - \bar{x}_2),\ \mathrm{d}z = \mathrm{d}\sigma$

$I_5 = -I_6$

Now

$$I_3 \sim \frac{1}{\bar{x}_2 + \rho\exp(i\theta)} \left(\frac{(\bar{x}_2 - x_2 + \rho\exp(i\theta))(\rho\exp(i\theta))}{(\bar{x}_2 - x_1 + \rho\exp(i\theta))(\bar{x}_2 - \bar{x}_1 + \rho\exp(i\theta))} \right)^{\pm\frac{1}{2}} i\rho\exp(i\theta)\,\mathrm{d}\theta$$

$$\to 0 \text{ as } \rho \to 0$$

and

$$I_2 = \frac{-i}{2}\int_{\bar{x}_1-\bar{x}_2}^{0} \frac{1}{\bar{x}_2+\sigma} \left(\frac{(\bar{x}_2 - x_2 + \exp(2\pi i)\sigma)(\exp(2\pi i)\sigma)}{(\bar{x}_2 - x_1 + \exp(2\pi i)\sigma)(\bar{x}_2 - \bar{x}_1 + \exp(2\pi i)\sigma)} \right)^{\pm\frac{1}{2}} \mathrm{d}\sigma$$

$$= \frac{-i}{2}\int_{\bar{x}_1-\bar{x}_2}^{0} \frac{1}{\bar{x}_2+\sigma} \left(\frac{(\bar{x}_2 - x_2 + \sigma)(\sigma)}{(\bar{x}_2 - x_1 + \sigma)(\bar{x}_2 - \bar{x}_1 + \sigma)} \right)^{\pm\frac{1}{2}} \exp(\pm i\pi)\,\mathrm{d}\sigma$$

$$= I_4$$

Thus we only have to worry about I_4. Changing notation such that $z = x$, $\mathrm{d}z = \mathrm{d}x$, $x = \bar{x}_2 \to \bar{x}_1$ gives

$$\begin{aligned}
I_4 &= \frac{-i}{2}\int_{\bar{x}_2}^{\bar{x}_1} \frac{1}{x} \frac{(x-x_2)(x-\bar{x}_2)}{[(x-x_1)(x-\bar{x}_1)(x-x_2)(x-\bar{x}_2)]^{1/2}}\mathrm{d}x \\
&\quad + \frac{-i}{2}\int_{\bar{x}_2}^{\bar{x}_1} \frac{1}{x} \frac{(x-x_1)(x-\bar{x}_1)}{[(x-x_2)(x-\bar{x}_2)(x-x_1)(x-\bar{x}_1)]^{1/2}}\mathrm{d}x \\
&= \frac{-i}{2}\int_{\bar{x}_2}^{\bar{x}_1} \frac{x - 2a_2 + \frac{1}{x}}{[(x_2-x)(x_1-x)(\bar{x}_1-x)(x-\bar{x}_2)]^{1/2}(-1)^{3/2}} \\
&\quad + \frac{x - 2a_1 + \frac{1}{x}}{[(x_2-x)(x_1-x)(\bar{x}_1-x)(x-\bar{x}_2)]^{1/2}(-1)^{3/2}}\,\mathrm{d}x \\
&= \int_{\bar{x}_2}^{\bar{x}_1} \frac{x - (a_1+a_2) + \frac{1}{x}}{[(x_2-x)(x_1-x)(\bar{x}_1-x)(x-\bar{x}_2)]^{1/2}}\,\mathrm{d}x \\
&= J_1 - (a_1+a_2)J_0 + J_{-1} \qquad \text{(B.5)}
\end{aligned}$$

where $J_{1,0,-1}$ correspond to elliptic integrals: in Gradshteyn & Ryzhick [83] J_1 matches Eqn.3.148.(2,3), J_0 matches Eqn.3.147.(2,3) and J_{-1} matches Eqn.3.149.(2,3).

Writing

$$w = \sqrt{\frac{(x_2 - x_1)(\bar{x}_1 - \bar{x}_2)}{(x_2 - \bar{x}_1)(x_1 - \bar{x}_2)}} = \sqrt{\frac{x_2\bar{x}_1 + x_1\bar{x}_2 - 2}{x_1x_2 + \bar{x}_1\bar{x}_2 - 2}}$$

and denoting the elliptic integrals of the first and third kinds by F and Π respectively, we can write $J_{1,0,-1}$ in two equivalent forms:

$$\begin{aligned}
J_1 &= \left[(\bar{x}_2 - x_2)\Pi(\frac{\pi}{2}, \frac{\bar{x}_2 - \bar{x}_1}{x_2 - \bar{x}_1}, w) + x_2 F(\frac{\pi}{2}, w)\right] \frac{2}{\sqrt{(x_2 - \bar{x}_1)(x_1 - \bar{x}_2)}} \\
J_0 &= \frac{2}{\sqrt{(x_2 - \bar{x}_1)(x_1 - \bar{x}_2)}} F(\frac{\pi}{2}, w) \\
J_{-1} &= \left[(x_2 - \bar{x}_2)\Pi(\frac{\pi}{2}, \frac{x_2(\bar{x}_2 - \bar{x}_1)}{\bar{x}_2(x_2 - \bar{x}_1)}, w) + \bar{x}_2 F(\frac{\pi}{2}, w)\right] \frac{2}{x_2\bar{x}_2\sqrt{(x_2 - \bar{x}_1)(x_1 - \bar{x}_2)}}
\end{aligned}$$

or

$$\begin{aligned}
J_1 &= \left[(\bar{x}_1 - x_1)\Pi(\frac{\pi}{2}, \frac{\bar{x}_1 - \bar{x}_2}{x_1 - \bar{x}_2}, w) + x_1 F(\frac{\pi}{2}, w)\right] \frac{2}{\sqrt{(x_2 - \bar{x}_1)(x_1 - \bar{x}_2)}} \\
J_0 &= \frac{2}{\sqrt{(x_2 - \bar{x}_1)(x_1 - \bar{x}_2)}} F(\frac{\pi}{2}, w) \\
J_{-1} &= \left[(x_1 - \bar{x}_1)\Pi(\frac{\pi}{2}, \frac{x_1(\bar{x}_1 - \bar{x}_2)}{\bar{x}_1(x_1 - \bar{x}_2)}, w) + \bar{x}_1 F(\frac{\pi}{2}, w)\right] \frac{2}{x_2\bar{x}_2\sqrt{(x_2 - \bar{x}_1)(x_1 - \bar{x}_2)}}
\end{aligned}$$

We can simplify the notation a little by introducing

$$\begin{aligned}
n_1 &= x_1 \frac{x_2 - x_1}{x_1x_2 - 1} \\
\bar{n}_1 &= \frac{1}{x_1} \frac{x_2 - x_1}{x_1x_2 - 1} \\
n_2 &= x_2 \frac{x_1 - x_2}{x_1x_2 - 1} \\
\bar{n}_2 &= \frac{1}{x_2} \frac{x_1 - x_2}{x_1x_2 - 1}
\end{aligned}$$

$$\xi = \frac{2\sqrt{x_1 x_2}}{x_1 x_2 - 1}$$

yielding two equivalent expressions for I_4:

$$\begin{aligned} I_4 &= \xi \left[(\bar{x}_2 - x_2)[\Pi(\frac{\pi}{2}, n_2, w) - \Pi(\frac{\pi}{2}, \bar{n}_2, w)] + (x_2 + \bar{x}_2 - a_1 - a_2) F(\frac{\pi}{2}, w) \right] \\ &= \xi \left[(\bar{x}_1 - x_1)[\Pi(\frac{\pi}{2}, n_1, w) - \Pi(\frac{\pi}{2}, \bar{n}_1, w)] + (x_1 + \bar{x}_1 - a_1 - a_2) F(\frac{\pi}{2}, w) \right] \end{aligned}$$

From Eqns B.3 and B.4, setting $\Pi(\frac{\pi}{2}, n, w) = \Pi(n|w)$, $F(\frac{\pi}{2}, w) = K(w)$, we obtain the expression used in Chapter 6:

$$\begin{aligned} \tilde{A}(r) &= 2\pi r - 2\xi \left\{ (x_1 - \bar{x}_1) \left[\Pi(n_1|w) - \Pi(\bar{n}_1|w) \right] + (a_1 - a_2) K(w) \right\} r \\ &= 2\pi r - 2\xi \left\{ (x_2 - \bar{x}_2) \left[\Pi(n_2|w) - \Pi(\bar{n}_2|w) \right] + (a_2 - a_1) K(w) \right\} r \end{aligned}$$

Expressed in this form, $\tilde{A}$ can readily be evaluated by standard numerical algorithms.

Bibliography

[1] T S van Albada, J N Bahcall, K Begeman. and R Sancisi. 1985, *Ap. J.*, **391**, 685

[2] M R Merrifield, 1992, *Astron. J.*,**103**, 1552

[3] F Zwicky, 1933, *Helv. Phys. Acta*, **6**, 110

[4] S M Faber and J S Gallagher, 1979, *Ann. Rev. Astr. Ap.*, **17**, 135

[5] C J Copi, D N Schramm and M S Turner, 1995, *Phys. Rev. Lett.*, **75**, 3981

[6] M Persic and P Salucci, 1992, *Mon. Not. R. Astron. Soc*, **258**, 14P

[7] P J E Peebles, 1986, *Nature*, **321**, 27

[8] M Fich and S Tremaine, 1991, *Ann. Rev. Astr. Ap.* , **29**, 409

[9] D Zaritsky, R Smith, C Frenk and S D M White, 1993, *Ap. J.*, **405**, 464

[10] D Pfenniger, F Combes and L Martinet, 1994 *A& A*, **285**, 79

[11] F De Paolis, G Ingrosso, P Jetzer and M Roncadelli, 1995, *A & A*, **295**, 597

[12] F Dyson, A S Eddington and C R Davidson, 1920 *Mem. R. Astron. Soc*, **62**, 291

[13] J Soldner, 1804, *Berliner Astronomisches Jarbuch 1804*, p. 161

[14] K R Popper, Unended Quest: An Intellectual Autobiography, Routledge, 1992

[15] A Einstein, 1936, *Science*, **84**, 506

[16] F Zwicky, 1937, *Phys. Rev.*, **51**, 679

[17] S Refsdal, 1964, *Mon. Not. R. Astron. Soc*, **128**, 307

[18] W H Press and J E Gunn, 1973, *Ap. J.*, **185**, 397

[19] D Walsh, R F Carswell and R J Weymann, 1979, *Nature*, **279**, 381

[20] R D Blandford and R Narayan, 1992, *Ann. Rev. Astr. Ap.*, **30**, 311

[21] J M Moran, J N Hewitt and K Y Lo, 1989, "Gravitational Lenses", *Lecture Notes in Physics*, **330**, Springer-Verlag

[22] C S Kochanek, 1990, *Mon. Not. R. Astron. Soc*, **247**, 135

[23] E Audit and J F L Simmons, 1997, *Mon. Not. R. Astron. Soc, submitted*

[24] K Chang and S Refsdal, 1979, *Nature*, **282**, 561

[25] B Paczyński, 1986, *Ap. J.*, **301**, 503

[26] M J Irwin, R L Webster, P C Hewitt, R T Corrigan and R I Jedrzejewski, 1989, *Astron. J.*, **98**, 1989

[27] R T Corrigan, M J Irwin, J Arnaud, G G Fahlman and J M Fletcher, 1991, *Astron. J.*, **102**, 34

[28] M R S Hawkins, 1996, *Mon. Not. R. Astron. Soc*, **278**, 787

[29] B Paczyński, 1986, *Ap. J.*, **304**, 1

[30] P Schneider, J Ehlers and E E Falco, 1992, "Gravitational Lenses", A & A Library

[31] C Alcock et al. (The MACHO Collaboration), 1997, *Ap. J.*, **486**, 697

[32] C Alcock et al. (The MACHO Collaboration), 1997, *Ap. J.*, **479**, 119

[33] K H Cook et al. (The MACHO Collaboration), 1997, in 12th IAP Colloquium: "Variable Stars and the Astrophysical Returns of Microlensing Surveys", eds. R Ferlet, J P Maillard, B Raban, Editions Frontières, p 17

[34] A Udalski et al., 1994, *Act. Astron.*, **44**, 165

[35] J P Beaulieu et al., 1995, *A & A*, **299**, L168

[36] R Ansari et al., 1995, *A & A*, **299**, L21

[37] K Griest et al. (The MACHO Collaboration), 1991, *Ap. J.*, **366**, 412

[38] C Alard, 1997, in 12th IAP Colloquium: "Variable Stars and the Astrophysical Returns of Microlensing Surveys", eds. R Ferlet, J P Maillard, B Raban, Editions Frontières, p 37

[39] K Griest and W Hu, 1992, *Ap. J.*, **397**, 362

[40] M Dominik, 1997, astro-ph/9703003

[41] S Mao and B Paczyński, 1991, *Ap. J. Lett.*, **374**, L37

[42] R Bontz 1979, *Ap. J.*, **233**, 402

[43] H A Witt and S Mao 1994, *Ap. J.*, **430**, 505

[44] C Renault et al., 1996, astro-ph/9612102

[45] Peng 1997, *Ap. J.)*, **475**, 43

[46] D Heyrovsky and A Loeb, 1997, astro-ph/9702097

[47] D Valls-Gabaud 1998, *Mon. Not. R. Astron. Soc*, **294**, 747

[48] D D Sasselov 1997, in 12th IAP Colloquium: "Variable Stars and the Astrophysical Returns of Microlensing Surveys", eds. R Ferlet, J P Maillard, B Raban, Editions Frontières, p 141

[49] A Gould, 1994, *Ap. J.*, **421**, L71

[50] A M Newsam, *in preparation*

[51] T L Swihart, 1981, "Radiation Transfer and Stellar Atmospheres", Pachart Publishing House

[52] A M Magalhães, 1988, in "Polarized Radiation of Circumstellar Origin", ed. G V Coyne et al., University of Arizona Press

[53] J Zorec and D Briot *A&A*, **245** 150, 1991.

[54] K Wood, K S Bjorkman and J E Bjorkman, *Ap. J.*, **477** 926, 1997.

[55] S J Chan and S Kwok, *Ap. J.*, **334** 362, 1988.

[56] P F Treanor, *Mon. Not. R. Astron. Soc*, **138** 325, 1968.

[57] J E Bjorkman, personal communication.

[58] C Alcock et al. (The MACHO Collaboration), 1997, *Ap. J.*, **491**, 436

[59] K Serkowski, in "Planets, Stars and Nebulae studied with photopolarimetry", ed. T Gehrels, University of Arizona Press, p 135

[60] M Saito and Y Saito, *Pub. Astron. Soc. Jap.*, **36** 603, 1984

[61] J C Brown, 1992, in "Inverse Problems in Scattering and Imaging", ed. M Bertero and E R Pike, Adam Hilger

[62] I J D Craig and J C Brown, Inverse Problems in Astronomy, Hilger, 1986

[63] D Gough, 1985, *Solar Physics*, **100**, 65

[64] C De Mol, 1992, in "Inverse Problems in Scattering and Imaging", ed. M Bertero and E R Pike, Adam Hilger

[65] V B Glasko Inverse Problems of Mathematical Physics, American Institute of Physics Translation Series, 1988

[66] Thomas J Loredo and Richard I Epstein. *Ap. J.*, **336** 896, 1989.

[67] Robert L Parker. *Ann. Rev. Earth Planet. Sci.*, **5** 35, 1977.

[68] G Backus and F Gilbert, 1970, *Phil. Trans. Roy. Soc. London*, **266**, 123

[69] F P Pijpers and M J Thompson 1992 *A & A*, **262**, L33

[70] J F L Simmons, A M Newsam, and J P Willis. stellar sources. *Mon. Not. R. Astron. Soc*, **276** 182, 1995.

[71] S Chandrasekhar. *Ap. J.*, **103** 351.

[72] S Chandrasekhar. Radiative Transfer. Clarendon Press, Oxford.

[73] W A Hiltner, 1947, *Ap. J.*, **106**, 231

[74] J C Kemp, G D Henson, M S Barbour, and D J Kraus. *Ap. J.*, **273** L85, 1983.

[75] R E Wilson and J C Liou. *Ap. J.*, **413** 670, 1993.

[76] K -D Goecking et al., *A & A*, **289**, 827, 1994

[77] E Landi Degl'Innocenti, M Landi Degl'Innocenti and M Landolfi. *A&A* **204** 133, 1988.

[78] D M Popper, 1984, *Ap. J.*, **89**, 132

[79] K Horne and T R Marsh, *Mon. Not. R. Astron. Soc*, **235**, 269, 1988.

[80] M Abramowitz and I A Stegun, Handbook of mathematical functions, Dover Publications, 1965

[81] A Claret and A Giménez, 1990, *A & A*, **230**, 412

[82] D Clarke and J F Grainger, Polarized Light and Optical Measurement, Pergamon Press, 1971

[83] I S Gradshtayn and I W Ryzhik, Table of Integrals, Series and Products, New York Academic Press, 1980

[84] I J Coleman, N Gray and J F L Simmons. 1998, *A & A*, in press

[85] I J Coleman, N Gray and J F L Simmons. *In preparation.*

[86] M B Bogdanov and A M Cherepashchuk 1996, *Astronomy Reports*, **40**, 713